

**Laser ablation assisted size-based sorting of pure  
water droplets inside a microfluidic chip and  
designing a microfluidic chip for studying  
sprouting angiogenesis**

by

**Ateeq Ur Rehman**

A Dissertation Submitted to the  
Graduate School of Sciences and Engineering  
in Partial Fulfillment of the Requirements for  
the Degree of

Doctor of Philosophy

in

Biomedical Sciences and Engineering



August 19, 2019

Laser ablation assisted size-based sorting of pure water droplets inside a  
microfluidic chip and designing a microfluidic chip for studying sprouting  
angiogenesis

Koç University

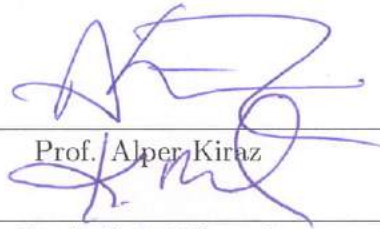
Graduate School of Sciences and Engineering

This is to certify that I have examined this copy of a doctoral dissertation by

**Ateeq Ur Rehman**

and have found that it is complete and satisfactory in all respects,  
and that any and all revisions required by the final  
examining committee have been made.

Committee Members:



Prof. Alper Kiraz



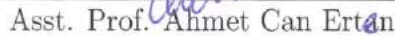
Prof. Kemal Baysal



Assoc. Prof. B. Erdem Alaca



Assoc. Prof. Halil Bayraktar



Asst. Prof. Ahmet Can Ertan

Date:

19/08/2019



*Dedicated to my beloved parents and family for all the support, love and  
encouragement...*

## ABSTRACT

We demonstrate an autonomous, high throughput and rigorous mechanism for sorting of droplets with different dimensions over inclined ( $\sim 10^\circ$ ), shallow ( $\sim 700$  nm) and narrow ( $\sim 22/30$   $\mu\text{m}$ ) guiding tracks defined by laser micromachining. We fabricated a microfluidic device containing two independent T-junctions and inlets for droplet generation allowing broad range of size and speed tuning as well as droplet merging before entering the Hele-Shaw channel hosting the guiding track. In the first part, we investigate partial guiding of different sizes of droplets under same host liquid flow conditions based on the three forces acting on the droplets namely drag force, frictional force and confinement force. For a bigger droplet, drag force being a quadratic function of droplet diameter dominates the confinement force causing the droplets leaving the inclined track earlier covering less vertical distance and guided partially. Secondly, as the speed of the droplet is increased by increasing the channel flow rate while keeping its size constant, higher drag force is exerted on the droplet once again causing partial guiding. Finally, we demonstrate sorting of smaller guided droplets co-flowing with bigger unguided droplets as a result of merging from two inlets in the common tapered region just before entering the Hele-Shaw channel. For all the experiments, we have considered two chip designs with different guiding track widths ( $22$   $\mu\text{m}$  and  $30$   $\mu\text{m}$ ) and found that the droplets undergo stronger guiding for the case of wider track because of the higher confinement force. All experimental results are correlated with analytical model results incorporating droplet size, speed, interfacial tension, contact angle and realistic droplet shape by finite volume method.

Microfluidic technology combined with tissue engineering has significantly increased the progress in cell biology and helped in understanding the physiological and pathophysiological transitions. PDMS due to its biocompatibility, optical trans-

parency and elasticity is widely used in fabrication of microfluidic devices for rapid prototyping to understand the 3D physiological microenvironment. We designed a novel microfluidic chip that incorporates a collagen hydrogel scaffold for 3D cell growth and enables controlled diffusion of medium through it. Thus, it is a convenient design that incorporates a hydrogel that mimicks the cellular microenvironment. Our design consists three parallel microchannels in contact with each other. By the unique height design, the hydrogel solution stays in the defined region and takes the shape of the collagen loading channel due to capillary action and surface tension effect. Angiogenesis; the formation of new capillaries from existing ones is mediated by endothelial cells. The hydrogel provides a porous 3D support which mediates the exchange of O<sub>2</sub> and nutrients. We studied the response of endothelial cells by stimulating them with vascular endothelial growth factor (VEGF) that diffuses through the 3D hydrogel scaffold from biochemical channel to the cell channel inside a microfluidic chip. Our novel design provides a favorable microenvironment for Endothelial cells to grow sprouts under the influence of stimuli by having a wide contact area between the collagen loading channel and the side channels. We found that our design works for studying sprouting angiogenesis and can be used for mimicking 3D microenvironments. We also designed another microfluidic chip that will be used as an indicator of the angiogenic potential of a tumor. It incorporates cells trapping wells in one of the side channels for trapping tumor cells and can be grown to become tumor spheroids in a chip. The side channel enables the formation of spheroids from injected tumor cells on the chip. This design is different from the previous design in a sense that no stimulus is introduced directly in the chip rather the growth factors and molecules secreted by tumor spheroids in its microenvironment will trigger endothelial sprouts. Different type of tumors secrete different growth factors and molecules. By using our designed microfluidic chip the angiogenic tendency of different tumors spheroids can be studied.

## ÖZETÇE

Tez kapsamında gerçekleştirdiğimiz çalışmalarla farklı boyutlardaki damlaların sınıflandırılmasına olanak sağlayan otonom, yüksek veri hacmine sahip, hassas bir mekanizma geliştirdik ve bunun için lazer işleme yöntemiyle üretilen eğimli ( $\sim 10^\circ$ ), sıg ( $\sim 700$  nm) ve dar ( $\sim 22/30$   $\mu\text{m}$ )'lik yönlendirme kanallarından faydalandık. Çok farklı boyutlarda ve hızlarda damla "retimi için, birbirinden bağımsız iki adet T-bağlantısı ve sıvı girişi bulunan, yönlendirme kanalının yer aldığı Hele-Shaw bölgesine girmeden hemen önce damlaların füzyonuna olanak sağlayan bir mikroakışkan çip ürettik. İlk olarak, aynı taşıyıcı akışkan koşulları altında üretilen farklı boyutlardaki damlaların kısmi yönlendirilmesi üzerine çalışmalarımızı gerçekleştirdik. Burada bir damla üzerine etki eden üç farklı kuvvet bulunmaktadır. Bunlar, sürüklenme kuvveti, sürtünme kuvveti ve yakalama kuvveti şeklindedir. Sürüklenme kuvveti damla çapına ikinci dereceden bağlıdır ve büyük bir damla için yakalama kuvvetine baskın gelir. Bu da damlanın eğimli kanalı diğer damlalara kıyasla daha erken terk etmesine, dolayısı ile dikey olarak daha az mesafe kaydetmesine ve kısmi olarak yönlendirilmesine neden olur. İkinci olarak, taşıyıcı kanaldaki akış hızını değiştirerek farklı hızlara sahip aynı boyutlarda damlalar üreterek her bir damla üzerine etki eden sürüklenme kuvvetini değiştirdik ve bunun benzer şekilde kısmi yönlendirmeye sebep olduğunu gözledik. Son olarak, kanal ile yönlendirilebilen küçük damlaları ve bu damlaların birleşimi ile oluşan daha büyük yönlendirilemeyen damlaları eş zamanlı olarak barındıran mikroakışkan çipte damla sınıflandırmasını gösterdik. Tüm deneylerde iki farklı kanal genişliğine sahip ( $\sim 22/30$   $\mu\text{m}$ ) mikroakışkan çip tasarımı kullandık ve daha geniş kanala sahip çipte yüksek yakalama kuvveti nedeni ile daha güçlü bir yönlendirmenin söz konusu olduğunu gözledik. Deneysel çalışmalarımızdan elde ettiğimiz tüm sonuçlar, damla boyutunu ve hızını, arayüz gerilimini, temas açısını ve gerçekçi dalma şeklini esas

alan analitik modelden elde ettiğimiz sonuçlarla uyumludur. Doku mühendisliği ile birleşen mikroakışkan teknolojisi, hücre biyolojisi alanındaki gelişmeleri hızlandırmış ve fizyolojik ve patofizyolojik geçişlerin anlaşılmasında yardımcı olmuştur. Polydimethylsiloxane (PDMS), biyouyumlu, şeffaf ve elastik olması sebebi ile 3 boyutlu fizyolojik mikroçevrelerin anlaşılmasına yönelik mikroakışkan cihazların hızlı şekilde üretilmesinde yaygın olarak kullanılır. Yaptığımız çalışmalarda, 3B hücre büyümesine olanak sağlayan kolajen yapı içeren ve kontrollü olarak ortam difüzyonu sağlayan özgün bir mikroakışkan çip tasarımı gerçekleştirdik. Bu, hücresel mikroçevreyi taklit eden hidrojel için uygun bir tasarımıdır. Geliştirdiğimiz çipte, birbiri ile geniş etkileşim yüzeylerine sahip üç paralel kanal bulunmaktadır. Bu üç kanalın sahip olduğu farklı yükseklikler sayesinde hidrojel çözeltisi belirlenen bölgede kalmakta ve kapiler etki, yüzey enerjisi gibi etkiler sayesinde merkezdeki kolajen kanalının şeklini tamamen almaktadır. Anjiyogenez, endotel hücreleri tarafından yeni kapillerlerin mevcut olanları üzerinden üretilmesi olarak tanımlanır. Hidrojel, mikroakışkan çip içerisine yerleştirilen hücrelere, O<sub>2</sub> ve besin erişimi için gözenekli 3B bir yapı sağlar. Yaptığımız çalışmalarda endotel hücrelerinin, 3B hidrojel yapının içine yayılan damar endotel büyüme faktörüne (vascular endothelial growth factor - VEGF) olan tepkilerini inceledik. Özgün tasarımıımız kolajen kanalı ve yan kanallar arasındaki geniş etkileşim alanı ile endotel hücrelerinin uyarıcı altında filizlenmesi için elverişli bir mikroçevre sağlamaktadır. Tasarımıımızın filizlenen anjiyogenez çalışmalarıda ve 3B mikroçevrelerin taklit edilmesinde kullanılabileceğini gösterdik. Ayrıca, tümörün anjiyogenik potansiyelinin araştırılmasında kullanılabilecek başka bir mikroakışkan çip tasarımı gerçekleştirdik. Bu çipin yan kanallarından birinde, hücrelerin içinde büyümesine ve tümör sferoid oluşumuna olanak sağlayan kuyular yer almaktadır. Bu yan kanal, çipe enjekte edilen tümör hücrelerinden sferoid oluşumunu mümkün kılmaktadır. Bu tasarımıda, doğrudan uyarıcının çipe verilmesi yerine çip içerisinde büyüyen tümör sferoidlerin ortama salacağı büyüme faktörlerine ve moleküllere tepki veren endotel filizlenmeleri incelenmektedir ve bu yönüyle önceki tasarımıdan ayrılmaktadır.

Farklı tipteki tümörler farklı büyüme faktörleri ve moleküller üretmektedir. Geliştirdiğimiz mikroakışkan çip kullanılarak, farklı tümör sferoidlerin anjiyojenik eilimleri çalışılabilir.





## ACKNOWLEDGMENTS

First and foremost, I would like to express my heartiest gratitude to my academic advisor, Prof. Dr. Alper Kiraz for his guidance, positive attitude, motivation and support throughout my research. He is a great source of inspiration and patience with brilliant mind. His scientific intuition and comprehension have always been very helpful. I would like to extend my deepest gratitude to him for invaluable knowledge and professional experience that I have gained over these years which I will use all along in my academic life.

Specifically, I thank Prof. Dr. Kemal Baysal for guiding and motivating me towards cell culturing in 3D microenvironment. My special thanks are extended to Dr. Alexandr Jonáš for his invaluable guidance, motivation and comments which extended this study and leading to success. I appreciate his great contribution in understanding droplet tracking algorithms, physics of microdroplets, scientific writing and learning surface chemistry. I thank Dr. Ahmet Erten for his help in explaining the theory of microfluidics, fabricating droplet microfluidic devices and his expertise in microdroplet experiments. I would like to thank Profs. Kemal Baysal, B. Erdem Alaca, Halil Bayraktar and Ahmet Erten for joining my thesis committee.

I would like to express my gratitude to former and current members of Kirazlab who produced a productive research environment, discussed and suggested innovative ideas and being good friends and helpful coworkers. Specifically, Dr. Berna Morova, Yiğit Uysallı, Rana Muhammad Armaghan Ayaz, Adil Mustafa, Ömer Yaman, Nima Bavili, Gamze Gül, Ekin Özgönül and Zeeshan Rashid. I would also like to thank Dr. Barış Yağci for his interest, help, and support in different parts of my thesis.

I express my warmest thanks to my brother Dr. Inayat Ur Rehman and my friends Arsalan Javeed, Abdul ALi, Waleed Bin Qaim, Imran Khan, Muhammad Suhaib, Ah-

san Jalal, Muhammad Zeeshan, Abasyn Ulasyar, Atif Aijaz, Munam Arshad, Karim Sonbol and all other friends for their unconditional friendship and being always supportive along the way of this study and as it was in the past.

I also thank Prof. Dr. Arif Bülent Özgüler and Assoc. Prof. Dr. Halil Bayraktar for their support and guidance.

Last, but not least, I would like to express my wholehearted thanks to my Parents in law, brother, Brother in law, sisters, sisters in law and my children for their endless love, encouragement and faith in me throughout my life. I express my deep gratitude to my wife, who has enriched all aspects of my life in the last three years. Her support and encouragement was worth more than I can express. Finally, I do not have words to express my thankfulness to my parents, Saif Ur Rehman and Raghdia Naseem, as I would not be able to reach this level today without their guidance and prayers.

# TABLE OF CONTENTS

<b>List of Tables</b>	<b>xiv</b>
<b>List of Figures</b>	<b>xv</b>
<b>Nomenclature</b>	<b>xxii</b>
<b>Chapter 1: Introduction</b>	<b>1</b>
1.1 Droplet microfluidics . . . . .	1
1.1.1 Literature review . . . . .	3
1.2 Microfluidic chip design for 3D cell culturing . . . . .	5
1.2.1 Literature review . . . . .	5
1.3 Angiogenesis . . . . .	7
1.3.1 Literature review . . . . .	8
1.4 Thesis organization . . . . .	9
<b>Chapter 2: Size-Based droplets sorting using laser ablated pattern</b>	<b>10</b>
2.1 Material and Methods . . . . .	14
2.1.1 Microfluidic chip parameters . . . . .	16
2.1.2 Experimental Setup . . . . .	17
2.2 Modeling of Droplet Motion . . . . .	18
2.2.1 Calculation of droplet surface area . . . . .	23
2.2.2 Area Prediction Correction and Corrected Areas . . . . .	25
2.3 Surface profile characterization of laser ablated tracks . . . . .	26
2.4 Results and Discussion . . . . .	28
2.4.1 Size-Based Guiding of Droplets . . . . .	29

2.4.2	Velocity-Based Guiding of Droplets . . . . .	32
2.5	Size-Based Sensitivity of Chip . . . . .	33
2.5.1	Size-Based Sorting of Merged Droplets . . . . .	35
<b>Chapter 3:</b>	<b>Microfluidic chip design for 3D cell culturing</b>	<b>39</b>
3.1	Microfluidic chip design for angiogenesis . . . . .	40
3.2	Materials and method . . . . .	43
3.2.1	Microfluidic system . . . . .	43
3.2.2	Microfluidic chip design for biochemical triggered angiogenesis	43
3.2.3	Microfluidic chip design for growing tumor spheroids . . . . .	46
3.3	Microfluidic chip fabrication and surface modification . . . . .	50
3.3.1	Master mold preparation for microfluidic chip . . . . .	50
3.3.2	PDMS chips preparation methodology . . . . .	51
3.4	Results and discussion . . . . .	53
3.4.1	Testing the collagen loading channel with ink water . . . . .	53
3.4.2	CFD simulations for confining water in the collagen loading channel . . . . .	54
3.4.3	Collagen preparation and loading inside a microfluidic chip . .	56
3.4.4	Collagen loading inside the microfluidic chip . . . . .	57
3.4.5	Treating the PDMS surface with Poly-d-lysine (PDL) . . . . .	57
3.4.6	collagen durability test . . . . .	58
3.5	Experiment with Msenchymal Stem Cells(MSCs) . . . . .	60
3.5.1	Experiment with Collagen type-1 . . . . .	60
3.5.2	Experiment with other hydrogel i.e.Hystem-HP cell culture . .	62
3.5.3	Hystem-HP hydrogel durability test . . . . .	63
3.5.4	Immunofluorescence (IF) staining of MSCs inside a microfluidic chip . . . . .	64

<b>Chapter 4:</b>	<b>Angiogenesis in 3D microenvironment</b>	<b>69</b>
4.0.1	Angiogenesis . . . . .	69
4.0.2	Angiogenesis stimulators . . . . .	73
4.0.3	Results and Discussion . . . . .	74
<b>Chapter 5:</b>	<b>Conclusion</b>	<b>84</b>
<b>Bibliography</b>		<b>87</b>

## LIST OF TABLES

2.1	Microfluidic chip parameters . . . . .	16
2.2	Droplet volume and area change due to 0.1% increase in radius. . . .	26
2.3	The list of cases investigated via CFD . . . . .	38
3.1	Collagen recipe. . . . .	56

## LIST OF FIGURES

2.1	(a) Schematic of microfluidic device used for the droplet generation, guiding and size-dependent sorting. (b) Partial guiding of emulsion droplets along a laser-ablated track as a function of the host liquid speed, (c) Fusion of droplets at the entrance of the flow channel followed by sorting of merged and unmerged droplets. . . . .	12
2.2	Schematics of the setup for droplet guiding and sorting experiments. .	17
2.3	Contours of volume fraction of the droplet liquid in the vicinity of the droplet/host liquid interface. The cross-sections of aqueous droplets (volume fraction 1 - red color) suspended in oil (volume fraction 0 - blue color) are shown in a plane located near the mid-channel height for (a) a newly initialized droplet and (b) a droplet after the completion of the CFD simulation. . . . .	20
2.4	CFD simulations of the shape of flattened emulsion droplets located in a microfluidic channel. Bottom views of droplets with $R = 60 \mu\text{m}$ (a) residing away from the guiding track and (b) centered on the track. .	21
2.5	(a) Droplet just before entering the track ( $\text{Area} = A_{out}$ ). (b) Droplet at the center of the track ( $\text{Area} = A_{in}$ ). . . . .	23
2.6	Generation of whole droplet surface, (a) generation of volume fraction contour on wall boundaries, (b) extraction of contact surfaces, (c) generation of interface surface, (d) uniting interface and contact surfaces under one surface group. . . . .	24

2.7	Surface profiles of guiding tracks obtained after laser ablation for Chips A, B and C in the main manuscript with track widths of (a) $22\mu\text{m}$ , (b) $30\mu\text{m}$ , and (c) $24\mu\text{m}$ . . . . .	27
2.8	Lateral surface profiles of a guiding track obtained after laser ablation for (a) forward and (b) backward profilometer scanning directions. The sharp peaks showed in dashed red squares are measurement artifacts, observed near the same position in different measurements. . . . .	28
2.9	Scanning electron micrograph of $30\mu\text{m}$ wide laser ablated pattern, (a) Portion of ablated pattern (1000X zoom), (b) Portion of ablated pattern (4000X zoom). . . . .	29
2.10	White light interferometry images of $30\mu\text{m}$ wide laser ablated pattern, (a) Portion of ablated pattern (5X objective), (b) Portion of ablated pattern (50X objective, (c) Portion of ablated pattern (50X objective after rinsing with ethanol and DT water. ) . . . . .	30
2.11	Dependence of the stability of droplet guiding on the droplet size. Experimental (black asterisks) and simulated (red, green and blue solid lines) trajectories of aqueous droplets with radii of 40, 60, and $120\mu\text{m}$ in (a) Chip A and (b) Chip B. The values of $U_o$ used for calculating the simulated trajectories were $U_o = (457,453,448)\mu\text{m/s}$ [ $U_o = (449,452,459)\mu\text{m/s}$ ] for 40, 60, and $120\mu\text{m}$ droplet radius in Chip A [Chip B], respectively. . . . .	31
2.12	Dependence of the stability of droplet guiding on the oil flow speed. Experimental (black asterisks) and simulated (cyan, yellow and magenta solid lines) trajectories of aqueous droplets with radius $60\mu\text{m}$ in (a) Chip A and (b) Chip B. The values of $U_o$ in individual experiments and simulations were $U_o = (229,352,450)\mu\text{m/s}$ for Chip A and $U_o = (308,452,701)\mu\text{m/s}$ for Chip B. . . . .	32



2.13	Parametric study of the stability of droplet guiding in laser-patterned microfluidic channels. The track exit height $\Delta H$ is plotted as a function of the oil flow speed $U_o$ in (a) Chip A and (b) Chip B for droplets with $40\ \mu\text{m}$ (red), $60\ \mu\text{m}$ (green), and $120\ \mu\text{m}$ (blue) radii. Experimental data are shown as colored squares, simulated results are denoted by lines in corresponding colors. In part (a), droplet guiding was simulated for laser ablated patterns with the width of $22\ \mu\text{m}$ and depths of $920\ \text{nm}$ (dashed lines), $720\ \text{nm}$ (solid lines) and $520\ \text{nm}$ (dotted lines), in part (b), droplet guiding was simulated for laser ablated patterns with the width of $30\ \mu\text{m}$ and depths of $990\ \text{nm}$ (dashed lines), $790\ \text{nm}$ (solid lines) and $590\ \text{nm}$ (dotted lines).	33
2.14	Sensitivity of size-based droplet sorting for different flow speeds of the host liquid. (a) Simulated track exit height $\Delta H$ as a function of the oil flow speed $U_o$ for droplets of varying radii $R$ guided in Chip B, assuming the depth of the laser-ablated guiding track of $790\ \text{nm}$ . (b) Track exit height $\Delta H$ as a function of the droplet radius $R$ for four selected values of the oil flow speed [ $U_o = (111, 429, 570, 671)\ \mu\text{m/s}$ ] indicated by vertical lines with matching line styles shown in part (a).	36
2.15	Experimental demonstration of size-based sorting of unfused and fused droplets formed at the inlet of a Hele-Shaw flow channel. Time-lapse images illustrate the trajectories of several droplets through the channel. While the smaller unfused droplets follow the laser-ablated guiding track, larger fused droplets proceed through the channel without being deflected by the track.	37
3.1	Schematic of microfluidic chip designed for direct injection of stimulus.	45

3.2	The design of a microfluidic chip for direct injection of biochemical/stimulus form one of the side channel, (a) 3D view of the microfluidic chip, (b) cross-sectional view of the microfluidic chip, showing the difference in the height of the channels. . . . .	46
3.3	Schematic of microfluidic chip for growing tumor spheroids on chip . . . . .	48
3.4	Microfluidic chip design for growing tumor spheroids on a chip for studying angiogenic potential of tumor spheroids, (a) 3D view of the microfluidic chip, (b) cross-sectional view of the microfluidic chip. . . . .	49
3.5	Designing master mold using aluminum tape, (a) first layer of aluminum tapes defining the general design of the microfluidic chip, (b) second layer of the side channels, (c) putting second layer of side channels on the general design layer for introducing the height difference between the side channels and the central collagen loading channel, (d) aluminum tape made two layer master mold. . . . .	51
3.6	Illustration of stamping method for making microfluidic chips . . . . .	52
3.7	Collagen channel testing using ink to show the confinement by collagen loading channel. . . . .	53
3.8	Volume fraction of water flowing inside the collagen loading channel, CFD simulation, (a) shows the volume fraction of water flow in 2D (left) and 3D image (right) of the water flow inside the microfluidic chip at 0.01 sec. (b) shows the 2D (left) and 3D (right) images of water flow inside the microfluidic chip at 0.09 sec. . . . .	55
3.9	Treating microfluidic chip with PDL, (a) intrested microfluidic chip, (b) PDL treated microfluidic chip. . . . .	57

3.10	Collagen durability test with collagen concentration 2.8 mg/ml, (a) trapan bule test in one of the side channel immediately after collagen gelation, (b) after 4 hours of incubation trapan blue is introduced in the same side channel, (c) trapan blue test after 1 day incubation, (e) trapan blue loaded in the same side channel after 4 days of incubation.	59
3.11	Mesenchymal stem cells (MSCs) cultured on a 2D cell culture plate with confluency more than 90 percent. . . . .	60
3.12	Model of microfluidic chip experiment having mesenchymal stem cells seeded in one channel. . . . .	61
3.13	MSCs growth inside a microfluidic chip, (a) MSCs seeded immediately after hydrogel gelation, (b) microfluidic chip with cells after 4 hours of incubation, (c) MSCs after 48 hours of gelation and seeding, (d) MSCs after 72 hours of cells seeding inside a microfluidic chip, (e) Middle region of collagen channel showing MSCs after 120 hours of cells seeding inside a microfluidic chip, (f) Middle region of collagen channel showing MSCs after 168 hours of cells seeding inside a microfluidic chip, (g) MSCs after 120 hours of cells seeding inside a microfluidic chip, (h) MSCs after 168 hours of cells seeding inside a microfluidic chip. . . .	65
3.14	MSCs growth inside a microfluidic chip, (a) MSCs seeded immediately after hydrogel gelation, (b) microfluidic chip with cells after 4 hours of incubation, (c) MSCs after 24 hours of gelation and seeding, (d) MSCs after 72 hours of cells seeding inside a microfluidic chip, (e) MSCs after 96 hours of cells seeding inside a microfluidic chip, (f) MSCs after 144 hours of cells seeding inside a microfluidic chip. . . . .	66

3.15	Hystem-HP durability test inside a microfluidic chip using trapan blue, (a) trapan bule test in one of the side channel immediately after collagen gelation, (b) after 4 hours of incubation before trapan blue is introduced in the same side channel, (c) adding trapan blue after 4 hours incubation, (e) trapan blue loaded in the same side channel after 5 days of incubation. . . . .	67
3.16	Fluorescence stained actins (green), tubulins (red) and nucleus (blue) MSCs, (a & b) MSCs in collagen type-1, (c & d) MSCs in Hystem-HP hydrogel. . . . .	68
4.1	Sprouting angiogenesis triggered by biochemicals, (a) sprouting angiogenesis by providing biochemical directly, (b) biochemical secreted by tumor spheroids triggered sprouting angiogenesis. . . . .	70
4.2	3D schematic illustrating the generation of new vessele through intussusceptive angiogenesis, (BM)base membrane, (fb) fibroblast, (pr) pericytes. . . . .	72
4.3	Dextran 70kDa loaded in one of the side channel for performing diffusion experiment. . . . .	75
4.4	Diffusion profile of Dextran 70kDa in collagen type-1 (2.8 mg/ml) recorded at different time intervals. . . . .	76
4.5	Fluorescent images for the diffusion of Dextran 70kDa in collagen type-1 (2.8 mg/ml) inside a microfluidic chip. . . . .	77
4.6	Diffusion profile of Dextran 70kDa in Hystem-HP hydrogel inside a microfluidic chip. . . . .	78
4.7	Fluorescent images for the diffusion of Dextran 70kDa in Hystem-HP hydrogel inside a microfluidic chip. . . . .	79
4.8	Human umbilical vein endothelial cells (HUVECs) cultured on a 2D cell culture plate showing confluency more than 70 percent. . . . .	80

4.9	Model of microfluidic chip experiment having mesenchymal stem cells seeded in one channel. . . . .	81
4.10	Endothelial cells growth inside a microfluidic chip, (a) ECs seeded immediately after hydrogel gelation, (b) microfluidic chip with ECs after 4 hours of incubation, (c) ECs after 24 hours of incubation after introducing ECs and stimulus at 0 hour, (d) ECs after 23 hours of stimulus, (e) ECs after 48 hours of stimulus, (f) EC with sprouts after 48 hours of stimulus (20X), (g) First half of the region of ECs after 48 hours of stimulus (10X), (f) Second half of the region of ECs after 48 hours of stimulus (10X). . . . .	83

## NOMENCLATURE

A	Area
AC	Alternating current
BM	Base membrane
BSA	Bovine serum albumins
$\beta$	Frictional coefficient
CA	Contact angle
$C_a$	Capillary number
CFD	Computational fluid dynamics
CNC	Computer numerical control
CSF	Continuum surface force
CMOS	Complementary metal oxide semiconductor
DAPI	4',6-Diamidino-2-Phenylindole, Dihydrochloride
d	Center distance between droplet and track
DMEM	Dulbecco's modified eagle medium
$D_L$	Droplet length over left track edge
$D_R$	Droplet length over right track edge
E	Surface energy
FEM	Finite element method
FITC	Fluorescein isothiocyanate isomer
$fs$	Femtosecond laser
$F_D$	Drag force
$F_{D,p}$	Pressure drag
$F_{D,v}$	Viscous drag $F_f$
$F_\gamma$	Frictional force
	Trapping force

$F_{\gamma,s}$	Trapping force due to surface energy gradient
$F_{\gamma,w}$	Trapping force due to wetting defect
HMDS	Hexa-Dimethylsiloxane
h	Height of microfluidic channel
HUVEC	Human umbilical vein endothelial cells
IPA	Isopropyl alcohol
MSC	Mesenchymal stem cells
N	Nitrogen
NaOH	Sodium hydroxide
O	Oxygen
PDMS	Polydimethylsiloxane
pH	Potential hydrogen
PBS	Phosphate buffered saline
PFA	Paraformaldehyde
PDL	Poly-D-lysine
SEM	Scanning electron microscopy
SU-8	Negative photoresist
UV	Ultra violet light
VOF	Volume of fluid
WLI	White light interferometry
$\Delta H$	Relative track exit height of droplet
$K_0, K_1$	Modified Bessel functions of the second kind
$\phi$	Angular difference between droplet and track
$\Phi$	Angle of the guiding track
$Re$	Reynolds number
$R_1$	Central radius of squeezed droplet outside track
$R_2$	Central radius of squeezed droplet inside track
$R_U$	Upper radius of squeezed droplet inside track

$R_L$	Lower radius of squeezed droplet inside track
$t$	Thickness of PDMS coating
$\theta_t$	CA on top of the track
$\theta_p$	CA on top of the PDMS
$\mu$	Viscosity of oil
$U_d$	Droplet speed
$U_o$	Oil speed
$\xi$	Drag coefficient
$\gamma$	Surface tension



## Chapter 1

# INTRODUCTION

### **1.1 *Droplet microfluidics***

With the advancement in microfluidics technology, droplet based studies, its control and handling techniques have progressed continuously. Microfluidic systems have the ability to process Small volumes ranging from nano-litre to micro-liter. Micro scale droplets facilitates individualization, protection and arrangement of samples which makes it a suitable candidate for micro scale analysis with the advantage that individual droplet can be transported,sorted, merged and divided [Chabert, 2008, Shi, 2008, Douglas, 1998, Wang, 1997, Chabret, 2005, Baroud, 2007]. Droplet microfluidic devices uses two immiscible fluids for generating water-in-oil emulsion droplets. Droplet microfluidics has the ability to manipulate discrete volume of the fluids in the form of micro-droplets which provides the benefit of using it in micro scale chemical process and biological experiments. Droplets generated inside a microfluidic systems are widely used in variety of different applications ranging from drug screening, single cell analysis, next generation sequencing systems, molecular diagnostics, and micro reactors [Agresti, 2010, Baret, 2010, Pekin, 2011, Guo, 2012]. In order to utilize the microfluidic systems to it full capability, it is important to select and manipulate the desired droplets form the stream of continuously moving droplets. This gives an opportunity to control droplets merging and mixing its contents. The merged droplets can be sorted inside a microfluidic chip based on the physical, chemical and mechanical properties. In general droplets manipulations techniques can be broadly classifies in to two classes *i.e.* active manipulation techniques and passive manipulation techniques.

Active manipulation techniques includes electokinetic [Link, 2006], acoustic [Franke, 2006], magnetic [Chetouani, 2006], hydrodynamic [Yoon, 2014], and optical-force-induced droplet driving [Pit, 2016] but the performance of all these techniques relies on detection and controlled mechanism which requires complex systems for controlled detection and actuation [Verneuil, 2009, Shim, 2007, Huebner, 2009]. Magnetically labeled or electrically charged droplet sorting relies on relatively simple systems but the sample should be magnetically labeled or charged before sorting [Chetouani, 2006]. Active mechanism allows flexible control of droplets by providing the external users or programs to selectively manipulate the droplet which can be reliable and accurate in selecting a specific droplet from a stream of droplets using detectable features present in droplets. Active dielectrophoretic manipulation of emulsion droplets can be achieved by using AC electric field, created between integrated planar microelectrodes into a microfluidic chip. By switching on and off the AC electric field, the stream of droplets between collect channel and waste channel having different hydrodynamic resistances was switched, thus achieving an effective droplet sorting with sorting rate of more than 1.6 kHz [Ahn, 2005]. When droplets are charged in an electric field 'E', smaller droplets can be generated with precise control of its timing which can be used with other strategies to overcome surface tension [Thorsen, 2001, Sugiura, 2001, Anna, 2002]. By applying high voltages to the fluid stream, oil-water interface can be charged. The water behaves as a conductor whereas the oil behaves as an insulator. This electrochemical reaction makes the interface to behave like a capacitor. Droplets can be sorting using DC voltage by fabricating two indium tin oxide (ITO) electrodes facing microfluidic channel. In the absence of no applied voltage droplets enter alternatively left or right channel but when a voltage is applied to either side the droplets follows that side [Link, 2006].

Upon using dielectrophoresis (DEP) and a special geometry called gap divider, ultra high speed sorting can be performed. Using energized electrode droplets can be slightly moved to one side, this small lateral displacement by DEP increase as the droplet moves downstream and the droplet is forced into the pre-designed channel.

Since the operating time needed for one droplet is relatively short, ultra fast sorting speed with the highest rate reported approximately 30 kHz was achieved using this method [Sciambi, 2015]. Using lasers for droplet sorting showed that the interfacial tension (IFT) increases with temperature which is caused by the migration of the surfactants and the thermocapillary effect [Baroud, 2007]. Induced Marangoni-type flows, results in a 'pushing' force repels the droplet from the location of laser spot. Merging of two different droplets with different chemical contents can be achieved using laser light, thus triggering a chemical reaction of interest [Dangla, 2011]. Active manipulation techniques combined with the droplet detection content preceding the actual manipulation step is allowing maximal flexibility in controlling the droplet behavior. However, external control and sensing mechanisms usually increases the complexity and restrains the use of such techniques only to sophisticated systems.

### 1.1.1 Literature review

In recent years, many research groups demonstrated controlled manipulation of droplet sample using a different mechanism. Among all the techniques, passive manipulation schemes are more straightforward and offers an autonomous solutions for microfluidic systems. Passive manipulation techniques are simple and straight forward, with the disadvantage that once the chip design can not be altered once fabricated. Physical properties of the droplet, such as density, volume, size, viscosity and surface tension are important factors in sorting droplets in microfluidic chip.

Abbyad *et al.* demonstrated the guiding and trapping of droplets using a Hella-Shaw flow cell etched in the upper surface of the microchannel [Abbyad, 2010]. A nanoliter droplet contained within a micro-channel with height much less than the diameter of droplet, is trapped and guided by etching patterns on top surface of the chip. With in the chip the droplet is fattened pancake shape having high surface energy. A droplet of top of the pattern the droplet partially enters in etched pattern, thus decreasing the surface area and surface energy [Tullis, 2014]. This change of droplet surface energy provides an effective confinement mechanism for the droplet

to be trapped and guided inside the microfluidic chip [Dangla, 2011].

Xu *et al.* used railroad like channel network and guiding tracks used for fusion and sorting of two parallel trains of droplets [Xu et al., 2012]. Two parallel droplets following the guiding rail pattern fuses at the fusion region electrically. An additional fusion rail is provided starting from the fusion region located in the middle of the two guiding rails guides the fused droplet to the center railroad like track and takes it to the outlet. The droplets that do not merge follows the two individual guiding rails to the waste outlet tracks and are separated from the fused droplets. The main channel height is  $50\text{ }\mu\text{m}$  along with  $15\text{ }\mu\text{m}$  deep guiding rails [Xu et al., 2012], this causes less deformation to the droplets compared to the abbyad *et al.* where the main channel height was  $35\text{ }\mu\text{m}$ .

Yoon *et al.* demonstrated size-based droplet sorting using multi-level guiding tracks by dividing the flow in front of new groove in to two components i.e. tangential and normal to the direction of the existing groove pattern. The droplets that are trapped follows the rail path due to low laplace pressure on the rail in Hela Shaw cell. Smaller droplets do not reach the new rail and are not trapped thus recover its shape and position due to lower laplace pressure in old groove [Yoon, 2014].

Rashid *et al.* demonstrated sorting of two different droplets i.e. water and ethylene glycol with and without surfactant by providing a laser ablated track of depth 1-2 mm inside a microfluidic chip. The droplets are forced to follow the track due to the difference in wetting property and topographical defects of the hydrophilic tracks obtained by removing thin layer of coated PDMS on the microscope glass slide [Rashid, 2018]. Rashid *et al.* also showed the sorting of emulsion droplets based on the difference in the interfacial tension (IFT) using a shallow guiding track of depth  $0.6\text{ }\mu\text{m}$  defined by using a femtosecond laser ablation. Droplets covered different vertical heights by keeping same flow rate due to the difference in interfacial tension and contact angles, which can be used for sorting droplets. A theoretical model capable of predicting the trajectories of the droplets given the experimental condition was also presented [Rashid, 2019].

## 1.2 Microfluidic chip design for 3D cell culturing

Microfluidic technology provides a favorable platform for studying the 3D behavior of the cells. It has been applied for developing a spatiotemporal control mechanism for mimicking the cellular micro-environment [Young, 2010]. With the integration of microfluidics and cell or tissue biology the technology has opened new ways in development of new cell-based assays in biological research [Barbulovic-Nad, 2010, Su, 2011, Lecault, 2011, Young, 2012]. Previously, many studies were conducted to study cells migration in 2D [B. Vernon, 1999] like wound assay [Sudo, 2005], Teflon cells assay [Carmeliet, 2000] and Boyden chamber [Ridley, 2003, Griffith, 2006]. presently, microfluidics systems are used in phenotypic transition towards mural cells lineage by coculturing method [jeon], role of ANG-1 as vessel stabilizer, capillary morphogenesis [vernella], effect of VEGF on endothelial cells [Farahat, 2012], relationship between tumor cell intravasation and endothelial permeability in perspective of cytokine induced endothelial cells using TNF- $\alpha$  [Zervantonakis, 2012] and lung cancer migration [Anguiano, 2017]. To better replicate the physiological relevant microenvironment of living tissues in-vivo, there remains a need for quantitative cell migration assays in 3D.

### 1.2.1 Literature review

To better replicate the physiological relevant micro environment of living tissues in-vivo, there remains a need for quantitative cell migration assays in 3D to study the environmental factors in a controlled manner. Developing such a system will Achieving this will rationalize the investigations leading to a better understanding the effect of biochemical and mechanical factors that act along side in physiological and pathophysiological processes. which will ultimately facilitate the improvement in tissue engineering and therapeutic strategies. Lee *et al.* introduced a novel injection mold plastic array 3D culture (IMPACT) platform by patterning the gel containing cells using the capillary-guiding flow along the corners and the narrow gaps. HUVECs and fibroblasts were patterned in the desired regions and demonstrated angiogenesis [Lee

et al., 2018]. Chung *et al.* presented a microfluidic approach to investigate the cellular repercussion in 3D micro-environment using three independent flow channels i.e. control channel, cell channel and condition channel. All flow channels are separated by 3D collagen gel inserted through scaffold channel inside the microfluidic chip. The width of individual flow channel is 1 mm and height is 0.12 mm while the width of scaffold channel is 1.3 mm. The region of collagen scaffold that interacts with either condition/control channel or cell channel is 0.6 mm have a micro-pillar. Due to surface tension effect the collagen mixture stays in the scaffold channel and does not leaks to the flow channels [Chung, 2009b].

Vernella *et al.* developed a microfluidic platform for 3D cell culturing and demonstrated capillary morphogenesis. Their design contains two micro channels which are connected by a central region having square shaped micro-pillars array which provides the mechanical support to the soft gel and behaves like a gel cage. The two micro channels controls the fluid flow while the central gel region is used for cell culturing [Vickerman, 2008]. Compared to the design presented by Seok *et al.* where their is a single micro-pillar on each side of the scaffold channel, Vernella *et al.* proposed design have multiple micro-pillar array in the scaffold channel with the advantage that the soft collagen gel confines more strongly and the interaction region between collagen gel and flow channels is increased, which means multiple data points inside a single microfluidic chip.

Farahat *et al.* demonstrated a microfluidic assay for characterizing and analysing 3D angiogenic growth of in the presence of vascular endothelial growth factor (VEGF) and signaling lipid sphingosine-1-phosphate (S1P). Using S1P in the presence of VEGF gradient showed its importance in amplifying the angiogenic response. Directional flow of the cells in the side channels due to the hydrostatic pressure is coupled with the interstitial flow slants the cells towards the gel region which ultimately binds to the collagen region and form a single layer of cells. An array of trapezoidal micro posts with 100 - 125  $\mu\text{m}$  spacing on both sides of 1.3 mm wide collagen channel, cages the collagen solution in its well defined region with a uniform surface interface [Fara-

hat, 2012]. Compared to the design proposed by Vernella *et al.*, due to trapezoidal micro posts array this microfluidic assay provides increased number of angiogenic observations points from existing platforms achieved through parallelized cell culturing in similar extracellular conditions.

Jeon *et al.* demonstrated the co-culturing of endothelial cells (ECs) and bone marrow-derived human mesenchymal cells (BM-hMSCs) that generates human microvascular network and showed a phenotypic transition towards a mural cells lineage using the microfluidic chip designed by farhat et al. Further they investigated the role of endothelium related molecules *i.e.* angiopoietin (Ang-1) and transforming growth factor (TGF- $\beta$ 1) on BM-hMSCs to study the phenotypic transition both in monoculture and in direct contact with human endothelial cells (ECs) [Jeon, 2014].

### 1.3 Angiogenesis

The transportation network of blood vessels and lymphatic vessels is responsible for the transport of plasma, oxygen and nutrients to the cells and carry away the wastes from the cells throughout the body. For a normal physiological functions this is essential but it has implications in various pathological states [Risau, 1995]. Tissue fluid homeostasis, the absorption of dietary fat, and the functioning of the immune system is carried out by the lymphatic vasculature [Alitalo, 2011].

The endothelial cells (ECs) forming the blood vessels are attached to each other having tight junctions which is entirely covered by basement membrane along with contractile mural cells, pericytes and smooth muscle cells. ECs lies on the interior surface of the blood vessels which separates the fluid *i.e* blood form the tissues. The ECs are responsible for various bio-activities, like coagulation, filtration of fluids, arteriosclerosis blood vessel tone, hemostasis, inflammatory recruitment and infiltration, hormone trafficking, and most importantly, they play a very important role in angiogenesis by migration, proliferation and secretion of certain angiogenic factors [Formaggia, 2009, Carmeliet, 2000].

Another basal structure of walls of vessels is mural cells, like pericytes and venules

are the mural cells of capillaries and other blood vessels respectively. These pericytes makes the interior of the basal membrane and lines beneath the endothelial cells (ECs). Pericytes communicates with ECs using paracrine signaling mechanism or use cell junction directly and strengthens the barrier between surrounding tissues and capillaries [Polverini, 2002, Papetti, 2002, Rosenkilde, 2004]. Exchange of ions and small molecules between endothelial cells and pericytes us carried out using gap junctions. Interactions among cells is very important for vessel formation and its maintenance [Armulik, 2005, Gerhardt, 2003].

### 1.3.1 Literature review

Farahat *et al.* demonstrated 3D cell culturing and quantitative analysis of angiogenic growth from uniform endothelial monolayer using microfluidic assay which enables parallelized angiogenic growth instances and automated image processing. This enables high-throughput quantification of angiogenic growth. The assay was used to evaluate the combined effect of vascular endothelial growth factor (VEGF) and the signaling lipid sphingosine-1-phosphate(S1P) [Farahat, 2012]. Zervantonakis *et al.* presented a 3D in-vitro microfluidic model for tumor vascular interface to study relationship between tumor cell intravasation and endothelial permeability in perspective of cytokine induced endothelial cells using TNF- $\alpha$  [Zervantonakis, 2012]. They found increase in permeability of endothelial cells via macrophages signaling or through stimulation with tumor necrosis alpha (TNF- $\alpha$ ) and associated it with a higher intravasation rate. Aref *et al.* demonstrated a manifestation of EMT of cancer cells in 3D in the availability of human endothelial cells and monitored the EMT inhibitory effect of the drug using a microfluidic device. The cancer cell spheroids transferred to the microfluidic device exhibited mesenchymal morphology in less time with the human umbilical vein endothelial cells (HUVECs) co-culturing [Aref, 2013]. Anguiano *et al.* characterized a microfluidic platform for studying lung cancer cells migration under different microenvironment and experimental conditions. They found that at low concentration, Matrigel supports cells migration due to the supportive and growth



factor retaining environment while at high concentration cells migration slows down due to excessive cells attachment. It is also showed that antibody-based integrin blockade supports change in migration phenotype from mesenchymal or lobopodial to amoeboid [Anguiano, 2017]. Using microfluidic technology has enabled researches to precisely control geometrical, physical and biochemical microenvironment in cell biology applications. It is observed that single cell assays can yield millions of data points [Bonetta, 2005] while 3D multi-cellular assays can produce hundreds of parallel observations [Domansky, 2010a, Chen, 2010]. The microfluidic platform used previously used pillars array either in the middle channel or on both sides to confine the collagen. Pillars for confinement has the disadvantage that pillars restrict the cells and extracellular matrix interaction area and allows a handful of observations [Vickerman, 2008].

#### **1.4 Thesis organization**

The thesis is organized as follow: In chapter 2, laser ablated pattern assisted size based sorting of three different sizes *i.e.* 40  $\mu\text{m}$ , 60  $\mu\text{m}$  and 120  $\mu\text{m}$  radius on two different ablated width *i.e.* 22  $\mu\text{m}$  and 30  $\mu\text{m}$  having inclination angle of approximately  $10^\circ$  are discussed as a function of same oil velocity and varying oil velocities. As an application fusion/merging of two droplets generated by two separate T-junctions inside same microfluidic chip is demonstrated. Chapter 3 deals with the designing of a microfluidic device for studying 3D cells culturing and 3D microenvironment. In chapter 4, 3D microenvironment of angiogenesis is discussed, endothelial cells behaves as a sensors for the biochemical stimulus by producing sprouts in the direction of increase in gradient of the biochemicals.

## Chapter 2

# SIZE-BASED DROPLETS SORTING USING LASER ABLATED PATTERN

Miniaturized droplet-based microfluidic systems have recently underpinned a remarkable progress across the fields of medicine [Shi, 2008], security [Piorek et al., 2012], cell biology [Sollier et al., 2011, Abbyad et al., 2010] and microchemistry [Link et al., 2006]. In this wide spectrum of diverse applications, micro-scale droplets facilitate individualization, encapsulation, and protection of samples for single-cell analysis [Baret, 2010], cell growth [Guo, 2012], antibiotic synthesis [Mahler et al., 2018], drug discovery [Eduati et al., 2018], enzymatic activity [Agresti, 2010, Huebner, 2009], or DNA diagnostics [Pekin, 2011]. Owing to the recent technological advancements in the sample control and handling techniques, individual droplets can be efficiently transported, merged, trapped, dispersed, and sorted within microfluidic chips [Pit, 2016]. Controlled manipulation and sorting of droplets have been a subject of extensive research for the last decade and a broad spectrum of active as well as passive sorting methods have been experimentally demonstrated. Active sorting approaches including electrokinetic [Link et al., 2006], acoustic [Franke, 2006], magnetic [Chetouani, 2006], pneumatic [Xi et al., 2017] and optical [Verneuil, 2009] sorting offer flexible, remote selection and manipulation of a target droplet containing detectable features, either on-demand by instrument operator or automatically by a pre-programmed control routine. Passive sorting protocols, on the other hand, operate autonomously and exploit the material properties of the droplet and host liquids, architecture of the microfluidic chip, or shear forces acting in the confined flow geometry to selectively modify the droplet trajectory. As a result, design and prototyping of a robust passive sorting device requires considerable effort to converge to an optimized

layout that can be reliably employed in real-world microfluidic applications.

In recent years, a considerable effort has been dedicated to formulate passive droplet manipulation protocols based on the physical properties of the working liquids. Tan *et al.* reported sorting of droplets according to their size through controlling a bifurcating junction that divided the original flow into two daughter flow channels [Tan et al., 2004, Tan et al., 2007]. The difference in the shear forces experienced by the droplet caused it to move in the direction of the higher daughter flow. Harada *et al.* demonstrated size-based passive sorting due to different surface energy of droplets moving over a groove fabricated using UV lithography [Harada et al., 2012]. In particular, when located over the groove, smaller droplets acquire a more spherical shape as compared to the flattened shape of bigger droplets, resulting in lower surface energy and, thus, stronger confinement and more stable guiding along the groove. Xu *et al.* devised a microfluidic device capable of performing simultaneously electrical fusion and sorting of droplets approaching a fusion junction along two independent guiding tracks [Xu et al., 2012]. When two droplets moving in their respective tracks reach the fusion junction at the same time, they are electrically fused and the resulting fusion droplet continues to move along the central outlet track. On the other hand, unfused droplets remain in their original tracks and are guided to waste outlets. Kurup *et al.* demonstrated size-based sorting of droplets using tensiophoresis – a phenomenon utilizing two co-flowing host liquids with different interfacial tensions with respect to the droplet liquid, causing the suspended droplets to move towards the host liquid stream with a lower interfacial tension [Kurup and Basu, 2013]. The position of the interface between the two host liquid streams could be adjusted by varying the flow rates; as a result, size threshold for droplet sorting could be precisely tuned. Yoon *et al.* performed size-based sorting experiments using multiple droplet guiding grooves [Yoon, 2014]. In their approach, droplets guided along a single continuous groove encountered another parallel groove displaced laterally from the original one. Based on the droplet size and surface tension, hydrodynamic forces arising due to the interaction between the two grooves could either displace the droplet into the new

groove or keep it in the original one.

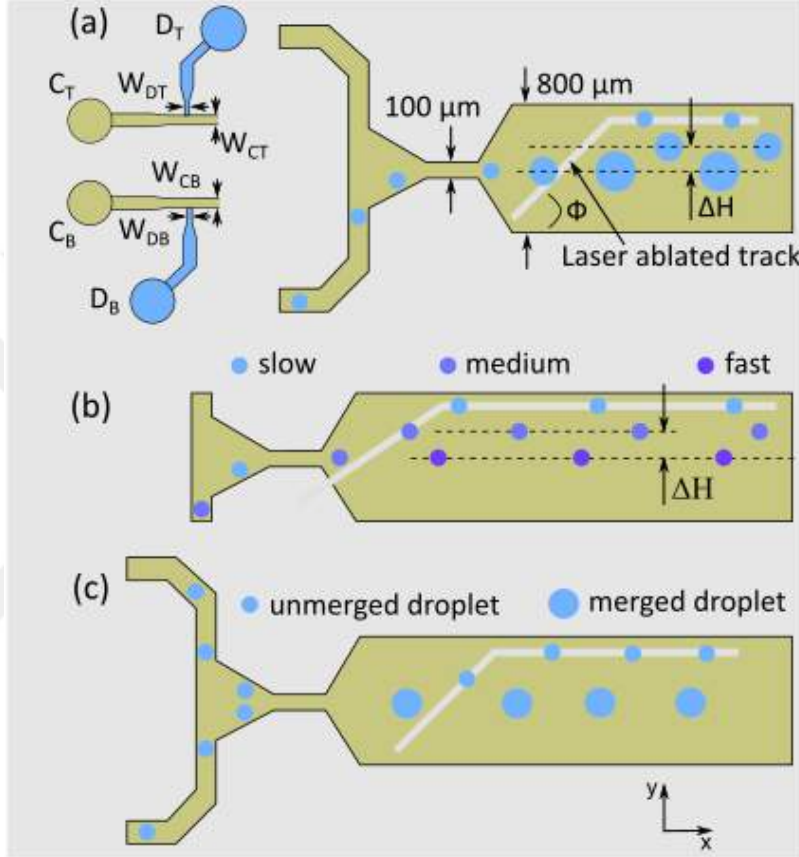


Figure 2.1: (a) Schematic of microfluidic device used for the droplet generation, guiding and size-dependent sorting. (b) Partial guiding of emulsion droplets along a laser-ablated track as a function of the host liquid speed, (c) Fusion of droplets at the entrance of the flow channel followed by sorting of merged and unmerged droplets.

In this chapter, we demonstrate controlled guiding and sorting of emulsion droplets moving over inclined, shallow guiding tracks obtained by selective removal of polydimethylsiloxane (PDMS) coatings deposited on glass substrates using laser ablation. The wetting contrast between the ablated and intact surfaces together with the obtained topographic features result in effective confinement forces attracting the droplets toward the guiding track. The stability of the droplet confinement then critically depends on the droplet size and the speed of the host liquid flow, which forms the basis of the droplet sorting mechanism. The proposed technique is easy to implement

and allows for integration of the droplet sorting tracks into various microfluidic chip layouts. Furthermore, the use of laser ablation for defining the guiding tracks has the advantage of rapid prototyping of different track geometries in a maskless manner, in contrast to the previously demonstrated microfluidic platforms, which often relied on at least two masks for their microfabrication [Xu et al., 2012, Yoon, 2014]. Due to an additional liquid inlet incorporated into our microfluidic platform, we can tune the speed  $U_o$  of the continuous phase flow without altering the droplet size. This allows for using  $U_o$  as an additional control parameter for droplet separation.

In our experiments, the droplets can be generated at two independent T-junctions [Garstecki et al., 2006] connected to a common Hele-Shaw flow channel featuring the guiding track, as shown in Fig. 2.1. A tapered, axially symmetric transition zone between the narrow entrance of the Hele-Shaw channel and the location where the channel reaches its full width ensures that the droplets arriving from both T-junctions experience laminar flow conditions at all times and, consequently, propagate along the axis of the channel. Moreover, the funnel-shaped region at the entrance of the main channel, in which the two droplet streams reaching the channel inlet from their respective T-junctions meet, facilitates spontaneous fusion of droplets that does not require any external triggering mechanism [Xu et al., 2012]. The droplet sorting demonstrated in this article is induced by a partial overlap of the droplet surface with the laser-ablated guiding track that results in a modification of the overall surface energy of the droplet. For all studied droplets, the track width is narrower than the diameter of the contact area between the droplet and the channel surface, with smaller droplets having a larger fractional overlap with the track. Hence, for these droplets, the relative changes of the droplet surface area upon interaction with the track are more significant, which results in larger effective confinement forces associated with changes of the droplet surface energy. Furthermore, smaller droplets experience a lower fluid drag destabilizing the confinement of the droplets and pushing them out of the track. As a net result of these phenomena, smaller and bigger droplets concurrently flowing through the channel follow the guiding track for different

distances, with smaller droplets being confined and guided more efficiently. Thus, the trajectories of droplets with different sizes are deflected to different streamlines across the channel and the droplets are spatially separated from each other at the end of the channel.

We characterize the performance of our droplet guiding and sorting technique by systematic experiments, in which we vary the size of the aqueous emulsion droplets, the speed of their motion through the microfluidic chip, and the width of the laser-ablated guiding track. In addition, we also simulate the droplet trajectories along the guiding track, using a previously developed theoretical model that includes the relevant forces acting on the moving droplets under the given experimental conditions [Rashid, 2019]. Such modeling requires realistic evaluations of changes in the shape and surface area of a droplet that is located partially inside and outside of the guiding track; these changes are obtained from detailed computational fluid dynamics (CFD) simulations. Using the simulated droplet trajectories, we analyze the sensitivity of our droplet sorting protocol and show it is possible to optimize the operating parameters for efficient separation of droplets with radii lying within the target size range. Finally, we demonstrate an application of our size-based droplet sorting mechanism, in which droplets of different sizes are first obtained by fusion of two independent droplet streams at the entrance of the Hele-Shaw flow channel and, subsequently, separated upon interaction with the guiding track.

## 2.1 Material and Methods

Microscope glass slides (dimension: 76 mm  $\times$  26 mm  $\times$  1 mm) were initially cleaned by dipping overnight in 2% solution of Hellmanex II (Hellma GmbH and Co.) in deionized water. PDMS (Dow Corning Sylgard 184) base agent and curing agent were mixed at a ratio 10:1 and the solution was diluted in toluene with 1:4 weight ratio. This mixture was spin coated over a clean glass slides at 6000 rpm for 120 sec resulting in PDMS coating layer of 700 nm to 800 nm. These coated glass slides were then kept in oven for 2 hr under 120°C to enhance PDMS cross linking. Using laser ablation

technique a PDMS coated glass substrate was used to make an ablation pattern which had an inclined and a straight section as shown in Fig. 2.1. An amplified Ti:Sapphire laser system (Spitfire<sup>®</sup> Ace<sup>™</sup>; Spectra Physics; maximum average power: 4 W, Gaussian beam diameter: 10 mm, pulse duration: 120 fs, wavelength: 800 nm, and repetition rate: 1 kHz) is used to selectively remove the PDMS coating over the glass slide and engrave a guiding pattern. Pulse energy has been attenuated to 3.5  $\mu\text{J}$  by means of neutral density filter to avoid laser penetration into the glass slide. The sample was placed on a three-axis micro machining system ( $\mu\text{FAB}^{\text{™}}$  Microfabrication Workstation; Newport) for translation and the scan speed was kept at 1 mm/s. A plano-convex spherical lens with the focal length of 50 mm was placed in the optical path to focus the ablation beam on the sample surface. With these parameters,  $\sim 10\ \mu\text{m}$  width of the track was achieved in a single pass which was extended by displacing the laser focus by 10  $\mu\text{m}$  before the next round. In this way, final track width of  $\sim 20\ \mu\text{m}$  and  $\sim 30\ \mu\text{m}$  for the two guiding chips were achieved which were confirmed by a Dektak profilometer. Microfluidic device based on PDMS elastomer was fabricated using conventional soft lithography technique. Silicon mold with fluidic channels was developed using UV lithography of negative photoresist (SU-8-50) coated on a silicon wafer. The PDMS base agent and curing agent (10:1 weight ratio) is mixed and degassed to remove bubbles and poured onto the silicon mold. It was then heated in oven for 2 hr at 75°C for PDMS curing, taken out and exposed to oxygen plasma (Euro plasma SN 010/226) along with the guiding chip to convert the patterned surfaces to hydrophilic. Immediately after oxygen plasma treatment, both surfaces were bonded carefully under a microscope to align the track inside the Hele-Shaw channel (see Fig. 1) followed by heating at 120°C for 72 hr to ensure absolute hydrophobic recovery. The systematic droplet experiments are carried out by injecting olive oil using syringe pumps in two continuous phases at a flow rate of 65  $\mu\text{L}/\text{h}$  and pure water at flow rate of 2  $\mu\text{L}/\text{h}$  for generating 40  $\mu\text{m}$  and 120  $\mu\text{m}$  while 2.5  $\mu\text{L}/\text{h}$  for 60  $\mu\text{m}$  in two dispersed phases of the top and bottom T-junction components as shown in Fig. 2.1(a). In partial guiding experiment of different sized droplets at constant speed, the oil flow

rate in the top inlet is kept constant at 30  $\mu\text{L/h}$  and that in the bottom inlet was varied from 20  $\mu\text{L/h}$  to 140  $\mu\text{L/h}$ . In the third set of experiment, droplet sizes are kept constant and their flow speed is increased to the point where the droplets cross the track fairly unguided. This procedure was repeated for three different sizes of the droplets; small, medium and big to plot the track exit height as a function of droplet speed. The experiments are performed on a three dimensional movable stage with top illumination and microscope objective mounted below the microfluidic device to capture droplet videos using camera.

### 2.1.1 Microfluidic chip parameters

In this study we report results obtained using three different microfluidic chips with the same angle of inclination ( $\Phi = 10^\circ$ ) but different ablated pattern widths, and T-junction parameters. These chips will be referred as Chips A, B and C throughout this paper. Chips A and B were used in experiments with a homogeneous droplet size where droplet size or speed was varied in a parametric manner. In contrast, Chip C was used to demonstrate sorting of merged droplets. All the design parameters of the chips used in our experiments are given in Table 2.1. In this table,  $d$ ,  $w$ ,  $\Phi$ ,  $W_{CT}$ ,  $W_{DT}$ ,  $W_{CB}$ , and  $W_{DB}$  correspond to the laser ablated track depth, track width, angle of inclination of the track, width of the continuous phase inlet at the top T-junction, width of the dispersed phase inlet at the top T-junction, width of the continuous phase inlet at the bottom T-junction, and width of the dispersed phase inlet at the bottom T-junction, respectively.

Table 2.1: Microfluidic chip parameters

	$d$ [ $\mu\text{m}$ ]	$w$ [ $\mu\text{m}$ ]	$\Phi$ [ $^\circ$ ]	$W_{CT}$ [ $\mu\text{m}$ ]	$W_{DT}$ [ $\mu\text{m}$ ]	$W_{CB}$ [ $\mu\text{m}$ ]	$W_{DB}$ [ $\mu\text{m}$ ]
<b>Chip A</b>	0.72	22	10	50	100	100	200
<b>Chip B</b>	0.79	30	10	50	100	100	200
<b>Chip C</b>	0.79	30	10	50	100	50	100



### 2.1.2 Experimental Setup

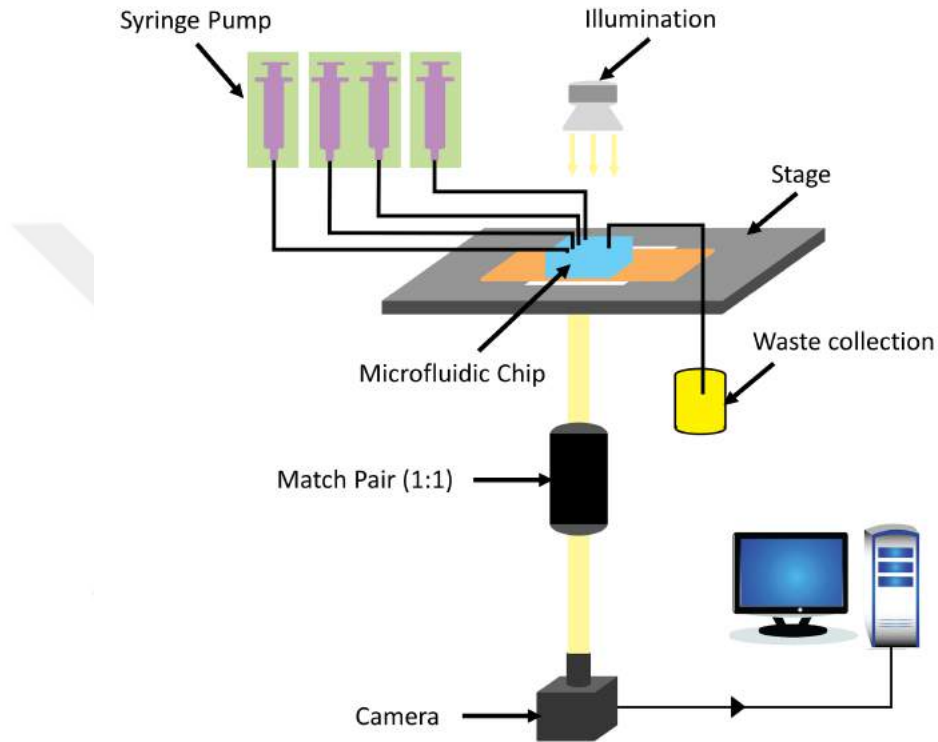


Figure 2.2: Schematics of the setup for droplet guiding and sorting experiments.

Figure 2.2 shows the schematic of the setup used for droplet guiding and sorting experiments. Inlet ports were connected through four independent syringe pumps (MTI Corporation; EQ-300SP-H-LD), two for injecting oil as the continuous phase and two for different droplet liquids (water) as the discontinuous phases.

The whole microfluidic device was kept on a 2D movable stage. An illumination from above was provided and videos of flowing droplets were captured from below using a CMOS camera (Hayear; HY-2307) and a matched achromatic doublet pair (Thorlabs; MAP10100100-A-1:1, Magnification: 1x), with the sample and CMOS chip placed at the front- and back-focal plane of the matched pair, respectively. Recorded videos of moving droplets were stored for subsequent off-line analysis of the droplet trajectories.

## 2.2 Modeling of Droplet Motion

In order to simulate the trajectories of droplets flowing through microfluidic channels featuring laser-ablated guiding tracks, we adopted the previously developed model of droplet guiding that ignores inertial effects at the low-Reynolds numbers limit ( $\text{Re} \ll 1$ ), *i.e.*, assumes a zero net force acting on the droplet at all times [Rashid, 2019]. Briefly, the net force acting on a guided droplet consists of three components: fluid drag force  $\mathbf{F}_D$ , frictional force  $\mathbf{F}_f$ , and confinement force  $\mathbf{F}_\gamma$ .  $\mathbf{F}_D$  - the sum of pressure and viscous drag - is exerted on the droplet by the flowing host liquid and causes the droplet to move along with the channel flow.  $\mathbf{F}_f$  arises due to the contact of the droplet with the top and bottom walls of the channel and opposes the droplet motion.  $\mathbf{F}_\gamma$  then corresponds to the effective force experienced by the droplet upon interaction with the laser-ablated guiding track. It originates from the changes of the droplet surface energy upon interaction with the track and represents the key ingredient of the droplet guiding and sorting phenomenon described in this article.  $\mathbf{F}_\gamma$  is modeled as a sum of two contributions: confinement force  $F_{\gamma,s}$  due to the changes of the droplet surface area that pushes the droplet towards the configuration with the minimal surface area and confinement force  $F_{\gamma,w}$  that results from gradients of surface wettability and pulls an aqueous droplet towards the hydrophilic regions of the ablated track:

$$F_\gamma = F_{\gamma,s} + F_{\gamma,w} = -\gamma \frac{\Delta A}{R_B + w/2} + \gamma(D_R - D_L)(\cos \theta_{in} - \cos \theta_{out}). \quad (2.1)$$

Here,  $\gamma$  is the interfacial tension (IFT) between the droplet and host liquids,  $D_L$  and  $D_R$  are the interaction lengths of the droplet with the left and right track edge,  $\theta_{in}$  and  $\theta_{out}$  are the droplet contact angles (CAs) inside and outside the track [Pit, 2016],  $R_B$  is the radius of the contact area between the droplet and the bottom wall of the channel,  $w$  is the width of the track, and  $\Delta A = A_{in} - A_{out}$  ( $\Delta A = A_{out} - A_{in}$ ) represents the change in the droplet surface area upon moving into (out of) the center of the track. Except for  $\Delta A$ , all the quantities that enter into Eq. 2.3 can be either independently measured beforehand or analytically calculated from the droplet geometry at each

time step during the simulation of droplet motion along the guiding track. Hence, precise determination of  $\Delta A$  is crucial for calculating the droplet trajectory from our model.

When a moving droplet lies entirely outside the track, its shape has a full rotational symmetry and, thus, its surface area,  $A_{out}$ , can be calculated analytically [Rashid, 2019]. On the other hand, the calculation of the surface area of a droplet partially overlapping with the track is not analytically tractable and requires a full three-dimensional computational fluid dynamics (CFD) analysis. In order to reduce the computational costs, in this study, CFD is employed solely to calculate the droplet surface area,  $A_{in}$ , of a droplet centered on the track. Numerically calculated values of  $A_{in}$  are then combined with analytically calculated values of  $A_{out}$  to approximate  $F_{\gamma,s}$  as  $-\gamma \frac{\Delta A}{R_B + w/2}$ , assuming  $F_{\gamma,s}$  remains constant during the droplet motion.

While the surface areas of the studied droplets were on the order of  $\sim 10^4 \mu\text{m}^2$ , the expected values of  $\Delta A$  were  $\sim 10^1 \mu\text{m}^2$ , much smaller than the droplet surface areas, due to the small depth of the guiding tracks. Thus, to evaluate  $\Delta A$  with less than 20% error, area calculations had to be done with an error smaller than 0.05%. Obtaining this high accuracy in area calculations was the biggest challenge of our CFD study. To achieve this goal, the numerical setup was constructed carefully and a correction procedure was applied to the droplet areas calculated by CFD. The details of the actual numerical algorithm, geometry of the computational domain, mesh adaptation procedure, mesh dependency test and initial/boundary conditions used in our CFD simulations are provided. In the beginning of a simulation, the droplets were introduced into the initial volume fraction field by defining a cylindrical region in contact with the top and bottom channel walls, whose radius was chosen so that the cylinder volume was exactly equal to the actual droplet volume. The cells of the computational domain, whose centers lied within the target cylindrical region, were then marked and their initial values of the volume fraction of the droplet liquid were changed from 0 to 1. The cells near the edge of the target cylindrical region were included or excluded depending entirely on the locations of their centers. Figure 2.3(a)

shows a magnified view of the droplet/oil interface after initializing the droplet inside the oil domain. Pixilated character of the interface results from the strictly binary inclusion or exclusion of individual cells from the target water domain. Figure 2.3(b) then shows an exemplary magnified view of the final shape of the droplet/oil interface obtained after the completion of the CFD simulation. Adaptive mesh refinement procedure visible in Fig. 2.3(b) yields a considerably smoother interface between the two liquid phases.

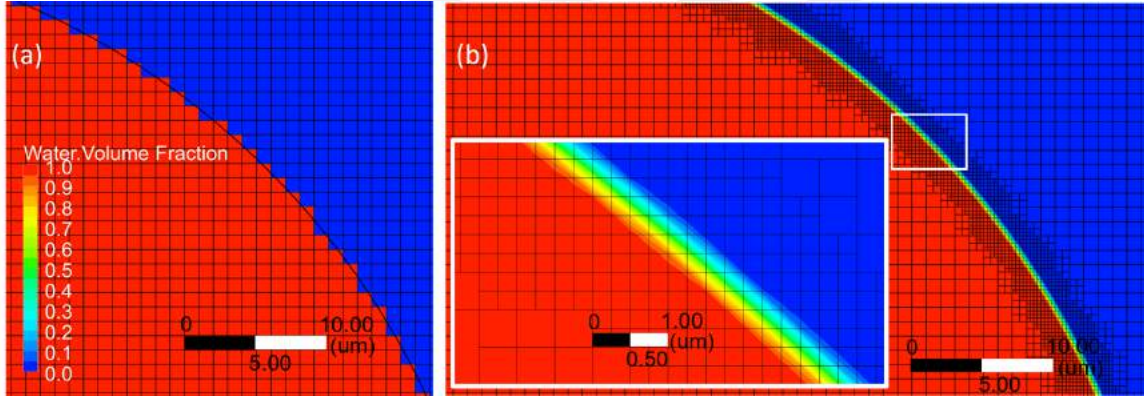


Figure 2.3: Contours of volume fraction of the droplet liquid in the vicinity of the droplet/host liquid interface. The cross-sections of aqueous droplets (volume fraction 1 - red color) suspended in oil (volume fraction 0 - blue color) are shown in a plane located near the mid-channel height for (a) a newly initialized droplet and (b) a droplet after the completion of the CFD simulation.

After the initialization step of the CFD simulations, an error of  $\sim 0.1\%$  in the droplet volume is introduced by the discretization process. In order to satisfy the requirement of high accuracy in the calculation of the droplet surface area, we developed and applied a correction procedure that reduced the effect of discretization-related errors to a negligible level. We validated our CFD simulations and the correction procedure by comparing the corrected values of the droplet surface area  $A_{out}$  determined by CFD with the values calculated analytically for droplets located away from the guiding track. After the correction, the error in calculating the total droplet area was revealed to be smaller than  $0.04\%$ . To visualize the shape of flattened emulsion droplets moving through a microfluidic channel, Fig. 2.4 shows bottom views of

droplets with  $R = 60 \mu\text{m}$  residing away from the guiding track [part (a)] and centered on the track [part (b)] obtained at the end of the CFD analysis.

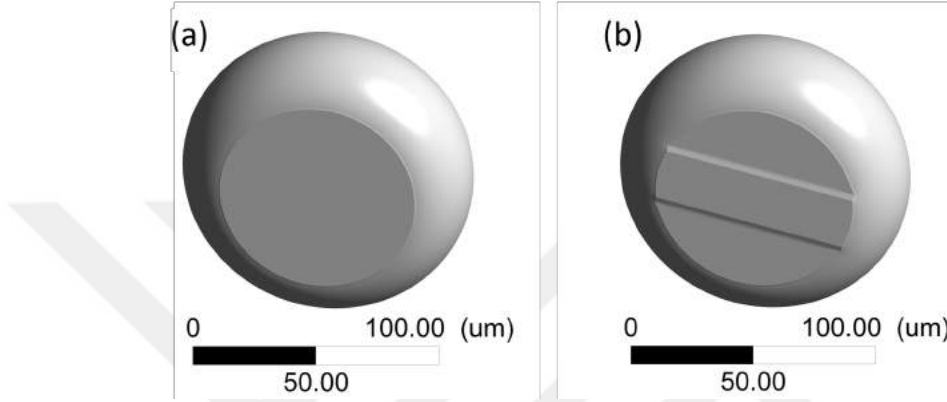


Figure 2.4: CFD simulations of the shape of flattened emulsion droplets located in a microfluidic channel. Bottom views of droplets with  $R = 60 \mu\text{m}$  (a) residing away from the guiding track and (b) centered on the track.

We used the analytical model developed in our previous work to simulate the droplet motion in the presence of a guiding track [Rashid, 2019]. This model ignores inertial effects at the low-Reynolds number ( $Re \ll 1$ ), *i.e.* assumes zero net force acting on the droplet at all instances, and follows a finite difference time domain approach to calculate droplet trajectories. There are three different forces acting on a droplet: Drag force ( $\mathbf{F}_D$ ), frictional force ( $\mathbf{F}_f$ ), and confinement force ( $\mathbf{F}_\gamma$ ).  $\mathbf{F}_D$ , is the sum of pressure drag and viscous drag, and is exerted on the droplet by the host liquid causing the droplet to move with the channel flow. Mathematically,  $\mathbf{F}_D$  is represented as [Pit, 2016]:

$$\mathbf{F}_D = \xi \left( \mathbf{U}_o - \frac{\mathbf{U}_d}{2} \right), \quad (2.2a)$$

$$\xi = 24\pi\mu \frac{R_2^2}{h} \left( 1 + 2 \frac{K_1(q)}{qK_0(q)} \right), \quad (2.2b)$$

where  $\xi$  is the drag coefficient,  $\mu$  is the viscosity of host liquid,  $R_2$  is the central radius of the squeezed droplet over the track,  $h$  is the channel height,  $\mathbf{U}_o$  is the oil velocity and  $\mathbf{U}_d$  is the average droplet velocity.  $q = 2\sqrt{3} R_2/h$ ,  $K_0$  and  $K_1$  are the modified

Bessel functions of the second kind [Pit, 2016].  $\mathbf{F}_f$  is obtained due to the droplet's interaction with the top and bottom channel walls.  $\mathbf{F}_f$  is expressed as  $\mathbf{F}_f = -\beta \mathbf{U}_d$ , where  $\beta$  is the frictional coefficient [Rashid, 2019].  $\beta$  values are determined to be  $0.696\xi$ ,  $0.58\xi$  and  $0.56\xi$  for droplets with 40, 60, and 120  $\mu\text{m}$  radius, respectively.

$\mathbf{F}_\gamma$  represents the force that is experienced by a droplet when its bottom surface interacts with the laser ablated guiding track.  $\mathbf{F}_\gamma$  tries to confine the droplet motion along the track and is composed of two forces: Confinement force due to surface area change ( $F_{\gamma,s}$ ) when the droplet surface area changes over the track, and confinement force due to surface wetting ( $F_{\gamma,w}$ ) as a result of the hydrophilic nature of the track.  $F_{\gamma,w}$  is given as:  $F_{\gamma,w} = \gamma(D_R - D_L)(\cos \theta_{in} - \cos \theta_{out})$ , where  $\gamma$  is the interfacial tension (IFT),  $D_L$  and  $D_R$  are the interaction lengths of droplet over the left and right track edges,  $\theta_{out}$  and  $\theta_{in}$  are the droplet contact angles (CAs) inside and outside the track, respectively [Pit, 2016].  $F_{\gamma,s}$  is evaluated by Fradet *et al.* [Fradet et al., 2011] as:  $F_{\gamma,s} = -\gamma dA/d\zeta$  which can be approximated as  $F_{\gamma,s} \approx -\gamma \Delta A / \Delta \zeta$ , where  $\Delta A$  is the total change in area and  $\Delta \zeta$  is the total interaction length traversed in the direction perpendicular to the track. For simplicity, surface areas are calculated when the droplet is entirely outside the track ( $A_{out}$ ) and exactly at the center of the track ( $A_{in}$ ) as shown in Fig. 2.5. In this way,  $\Delta \zeta$  can be calculated as  $\Delta \zeta = R_B + w/2$ , where  $R_B$  is the bottom contact radius and  $w$  is the width of the track.  $\Delta A$  is given as  $\Delta A = A_{in} - A_{out}$  or  $\Delta A = A_{out} - A_{in}$  when the droplet center remains in the left half or right half of the track, respectively. The total  $F_\gamma$  is then given as:

$$F_\gamma = -\gamma \frac{\Delta A}{R_B + w/2} + \gamma(D_R - D_L)(\cos \theta_{in} - \cos \theta_{out}). \quad (2.3)$$

As detailed in Ref. [Rashid, 2018], following the calculation of  $F_\gamma$ , droplet trajectories are determined using a finite difference time approach by determining the  $x$  and  $y$  components of  $\mathbf{U}_d$  at each time step using:

$$U_{d,x} = \frac{\xi U_o + F_\gamma \sin \Phi}{\beta + \xi/2}, \quad (2.4a)$$

$$U_{d,y} = -\frac{F_\gamma \cos \Phi}{\beta + \xi/2}. \quad (2.4b)$$

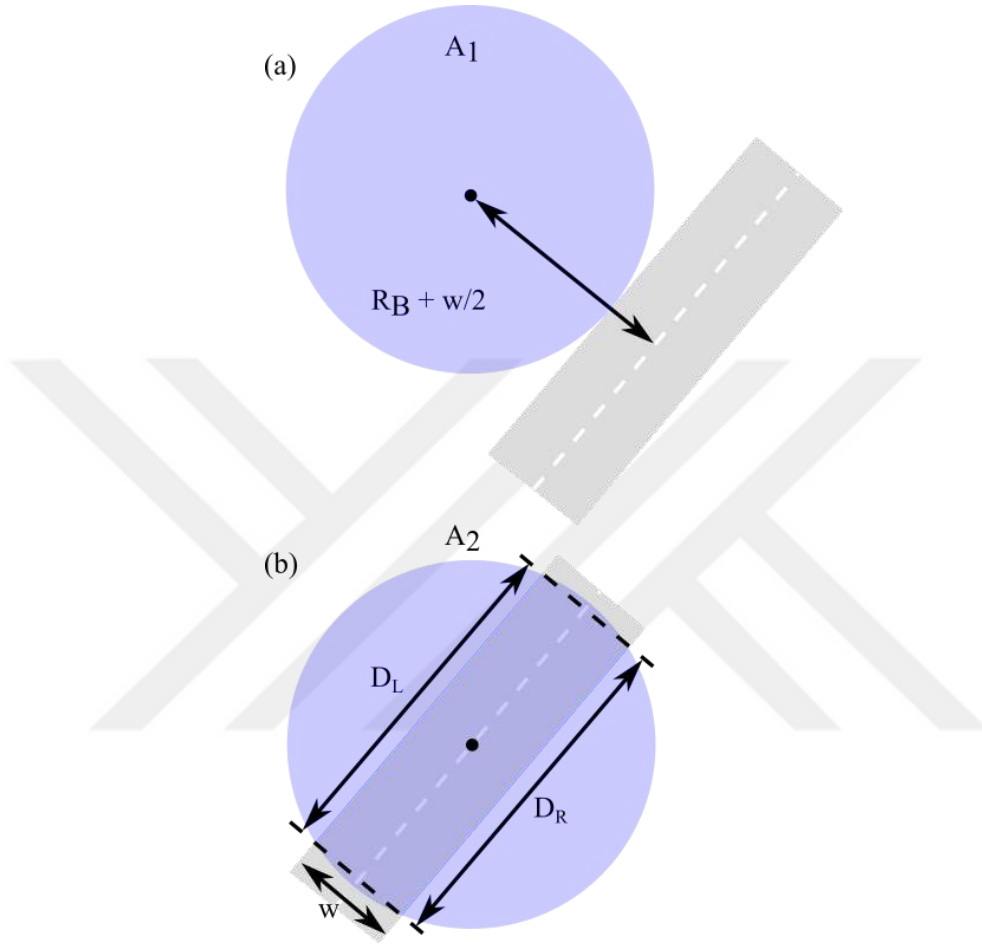


Figure 2.5: (a) Droplet just before entering the track (Area =  $A_{out}$ ). (b) Droplet at the center of the track (Area =  $A_{in}$ ).

At  $i^{th}$  time step droplet velocity  $[(U_{d,x})_i, (U_{d,y})_i]$  is updated, then the droplet position in the  $(i + 1)^{th}$  time step is calculated as  $x_{i+1} = x_i + (U_{d,x})_i \Delta t$ ,  $y_{i+1} = y_i + (U_{d,y})_i \Delta t$ , where  $\Delta t$  represents the time step interval. This procedure is then repeated to determine the position and velocity of a droplet at each time step.

### 2.2.1 Calculation of droplet surface area

The surface of a droplet consists of three parts, fluid-fluid interface surface (the iso-surface of volume fraction equals to 0.5), top and bottom surfaces where droplet is in contact with top and bottom walls. Once the simulations were completed, the area

of droplets were calculated using CFD-Post post process software.

In order to calculate contact areas, a contour plot of volume fraction with only two levels of contours on all wall boundaries was generated showing where the volume fraction is greater or lower than 0.5 with a sharp (zero thickness) interface. The contact surfaces were then extracted using the second contour level of this contour plot. As a last step, these generated surfaces were then united in single surface group to create outer surface of droplet. The generation of whole droplet surface is shown in Fig. 2.6.

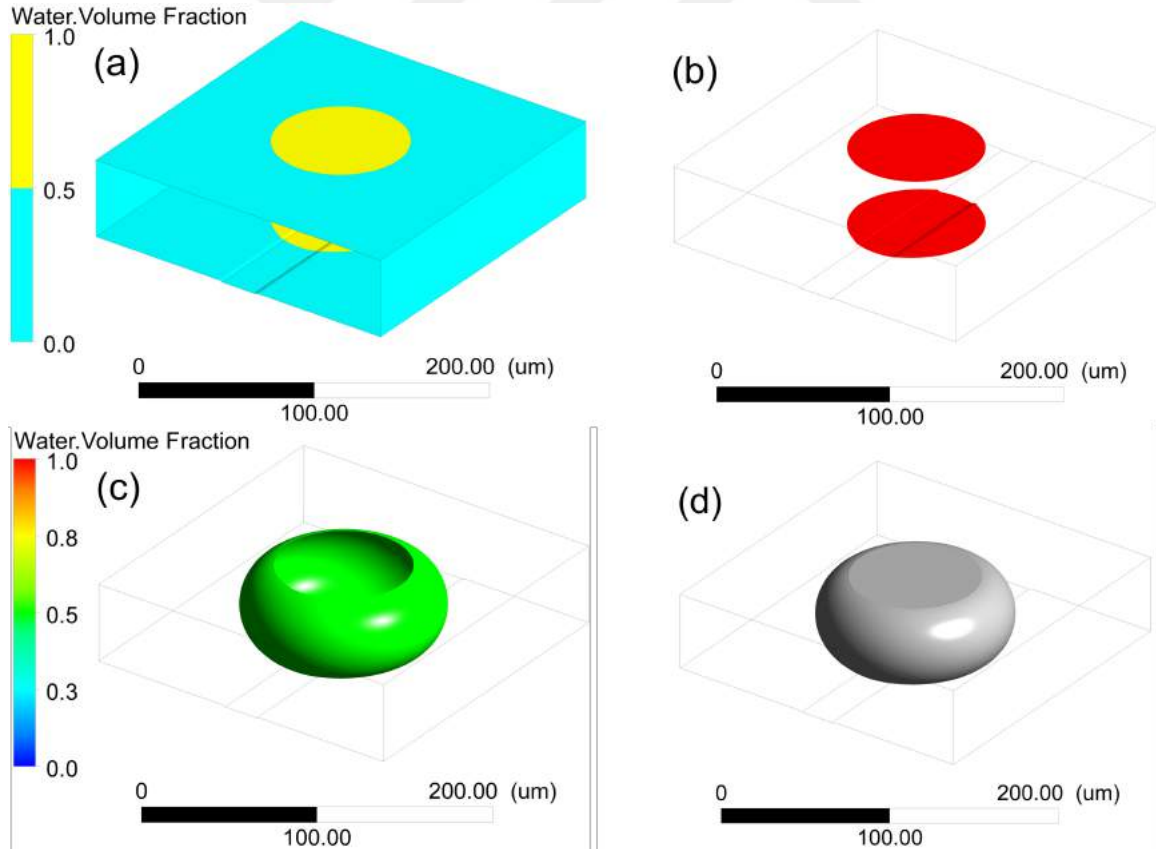


Figure 2.6: Generation of whole droplet surface, (a) generation of volume fraction contour on wall boundaries, (b) extraction of contact surfaces, (c) generation of interface surface, (d) uniting interface and contact surfaces under one surface group.



### 2.2.2 Area Prediction Correction and Corrected Areas

The droplet volumes ( $V_{actual}$ ) for desired radii were calculated using analytical relations [Rashid, 2019] and introduced to computational domain by patching the initial volume fraction field. However the patched volumes ( $V_{CFD}$ ) for all cases is slightly off from actual volume by approximately 0.1 because of the initialization procedure described in the Fig. 2 of the main manuscript. Having droplets larger or smaller than actual sizes causes errors in area values too. It is possible to reduce these errors by a correction procedure.

The corrected area of a droplet ( $A_{corr}$ ) with radius  $r$  was calculated by multiplying the droplet area evaluated using CFD ( $A_{CFD}$ ) by a correction multiplier ( $C_{corr}$ ). This multiplier was calculated using the predicted area error percentage ( $\varepsilon_{A_{predicted}}$ ) defined with the following equations:

$$A_{corr} = A_{CFD} \cdot C_{corr} , \quad (2.5)$$

$$C_{corr} = 1 - \varepsilon_{A_{predicted}} . \quad (2.6)$$

For a convex 3D object, increment in its radius causes a larger increment in its area and even larger increment in its volume by percentage. These suggest that for the same increase in radius, the relative error in droplet area must be smaller than the relative error in droplet volume. Volume of a droplet can be conveniently calculated when it is away from the track and applied to the instances where it is on the track, as droplet volume is a constant in our simulations. Thus volume error percentage ( $\varepsilon_V$ ) of any case can be calculated exactly. As an approximation to  $\varepsilon_{A_{predicted}}$ ,  $\varepsilon_V$  was multiplied by the ratio of area change percentage to volume change percentage caused by a slight change in radius using the following equations:

$$\varepsilon_{A_{predicted}} = \varepsilon_V(r) \frac{\Delta A(r)_{actual} / A(r)_{actual}}{\Delta V(r)_{actual} / V(r)_{actual}} , \quad (2.7)$$

$$\varepsilon_V(r) = \frac{V(r)_{CFD} - V(r)_{actual}}{V(r)_{actual}} , \quad (2.8)$$

$$\Delta A(r)_{actual} = A(r^+)_{actual} - A(r)_{actual} , \quad (2.9)$$

$$\Delta V(r)_{\text{actual}} = V(r^+)_{\text{actual}} - V(r)_{\text{actual}}, \quad (2.10)$$

$$r^+ = r + 0.001r. \quad (2.11)$$

$r^+$  stands for 0.1% increased radius where  $A(r)_{\text{actual}}$  and  $V(r)_{\text{actual}}$  in Eq.s S6-S10 indicate the area and volume of actual droplet away from the track, respectively. They were calculated using analytical relations [Rashid, 2019] and the results are shown in Table 2.2 for all radii used in this study.

Table 2.2: Droplet volume and area change due to 0.1% increase in radius.

<b>R</b> [ $\mu\text{m}$ ]	$\Delta R/R$	$\Delta A/A$	$\Delta V/V$	$\Delta A/A/\Delta V/V$
40	0.1%	0.164%	0.225%	72.7%
60	0.1%	0.171%	0.217%	78.5%
80	0.1%	0.175%	0.213%	82.3%
100	0.1%	0.179%	0.211%	85.0%
120	0.1%	0.182%	0.209%	87.0%

After correction, the numerical procedure is validated for droplets away from the track and absolute area error was revealed to be smaller than 0.04%. Results of all cases investigated via CFD are shown in Table 2.3 along with cases parameters,  $\varepsilon_{A_{\text{predicted}}}$  and  $A_{\text{corr}}$  values.

### 2.3 Surface profile characterization of laser ablated tracks

Figure 2.7 shows the surface profiles of laser-ablated tracks recorded for Chips A, B and C in the main manuscript with widths of 22  $\mu\text{m}$  (Fig. 2.7(a)), 30  $\mu\text{m}$  (Fig. 2.7(b)), and 24  $\mu\text{m}$  (Fig. 2.7(c)), respectively. Surface profilometer (Dektak 150; Veeco) scans of the PDMS surfaces were recorded in the direction perpendicular to the ablated tracks. During the laser ablation, PDMS debris accumulate at the top edge of the track due to the ablation direction. The broad bumps observed in the surface profiles around the track edges originate from those debris.

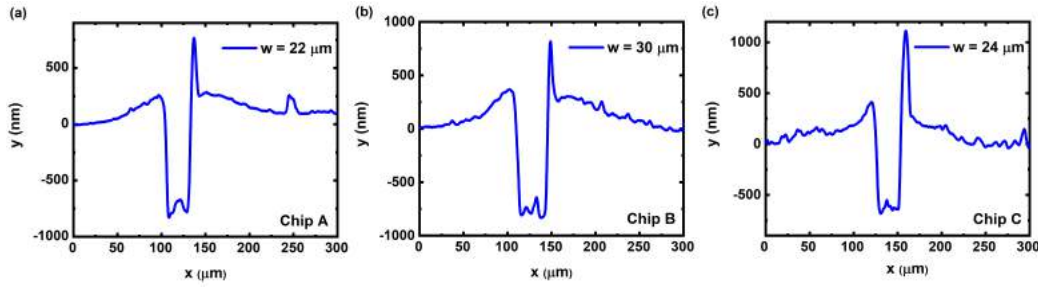


Figure 2.7: Surface profiles of guiding tracks obtained after laser ablation for Chips A, B and C in the main manuscript with track widths of (a)  $22\mu\text{m}$ , (b)  $30\mu\text{m}$ , and (c)  $24\mu\text{m}$ .

The sharp peaks observed at the right side of all surface profiles shown in Fig. 2.7 originate from a profilometer measurement artifact. In order to show that those peaks do not belong to scanned surfaces, profilometer scans were recorded for another laser-ablated track in forward and backward scan directions (see Fig. 2.8). For both scan directions, the sharp peak was observed at the same side of the measured surface profiles. These sharp peaks are measurement artifacts observed when the profilometer needle suddenly moves upwards, following a steep slope. We note that the laser-ablated track discussed in Fig. 2.8 was not used in our droplet sorting but only used for characterization of the ablated surfaces.

Figure. 2.9. shows the surface characterization PDMS coated microscope glass side having a laser ablate pattern of width  $30\mu\text{m}$  using scanning electron micrograph (SEM). A portion of the laser ablated pattern is shown in Fig. 2.9 (a). with 1000X zoom while Fig. 2.9 (b). having 4000X zoom. SEM images confirms the width of the laser ablated pattern, which is approximately  $30\mu\text{m}$  and is in accordance to the width measured using dektak profilometry.

In addition to SEM which gives information about the surface properties of the substrate, white light interferometry (WLI) on the other hands uses the light reflected from the surface to give indepth information about the irregularity of the surface. Fig. 2.10. shows the WLI images of the PDMS coated microscope glass slide to see the depth and boundary walls orientation for  $30\mu\text{m}$  wide and  $790\text{nm}$  deep laser ablated

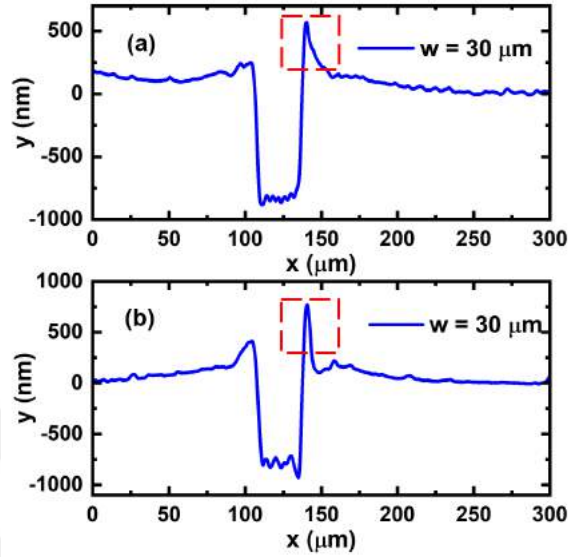


Figure 2.8: Lateral surface profiles of a guiding track obtained after laser ablation for (a) forward and (b) backward profilometer scanning directions. The sharp peaks showed in dashed red squares are measurement artifacts, observed near the same position in different measurements.

pattern. Fig. 2.10 (a). shows the WLI image of the portion of laser ablated pattern recorded with 5x objective lens, while the WLI image recorded with 50x objective lens is shown in Fig. 2.10 (b). Fig. 2.10 (c) shows the WLI image of the portion of the laser ablated track after rinsing with ethanol and DI water. It can be seen the by doing so we get rid on the residues and the surface is clean.

## 2.4 Results and Discussion

In order to characterize the performance of our droplet guiding and sorting technique, we carried out systematic experiments with aqueous emulsion droplets of varying sizes moving at different flow rates of the host liquid in microfluidic chips featuring guiding tracks of different widths. The chips used in the experiments, featuring two separate T-junctions with individually adjustable flow rates of both droplet and host liquids, allowed for controlling the speed of droplet motion through the chip independently of the droplet size [Rashid, 2019]. In addition, droplets produced at different T-junctions

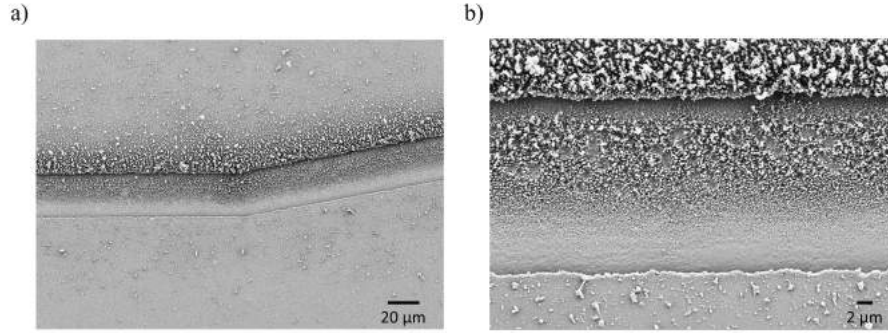


Figure 2.9: Scanning electron micrograph of  $30\mu\text{m}$  wide laser ablated pattern, (a) Portion of ablated pattern (1000X zoom), (b) Portion of ablated pattern (4000X zoom).

could be fused at the entrance port of the Hele-Shaw flow channel, thus creating a sorting scenario with two distinct, well-defined droplet sizes present simultaneously in the chip. The stability of droplet guiding along the laser-ablated track was evaluated in terms of the track exit height  $\Delta H$  measured as the distance along the  $y$ -axis between the center of the Hele-Shaw flow channel and the point at which the moving droplet leaves the track (see Fig. 2.1(a) for illustration). The maximal value of  $\Delta H$  that could be achieved by a droplet in the complete guiding scenario was  $280\mu\text{m}$  in Chip A,  $270\mu\text{m}$  in Chip B, and  $290\mu\text{m}$  in Chip C, determined by the geometry of the flow channel and the guiding track.

#### 2.4.1 Size-Based Guiding of Droplets

Figure 2.11 summarizes the results of droplet guiding experiments conducted in Chips A and B with aqueous droplets of radii of  $40$ ,  $60$ , and  $120\mu\text{m}$ . During these experiments, both continuous-phase inlets ( $C_T$  and  $C_B$ ) and one of the two dispersed-phase inlets ( $D_T$  or  $D_B$ ) of the T-junctions were used at a time. This way, one T-junction served to generate droplets with a desired size while the adjustment of the flow rate into the continuous phase inlet of the other T-junction allowed to control the droplet velocity. While performing the experiments, the flow rates at the inlets of the T-

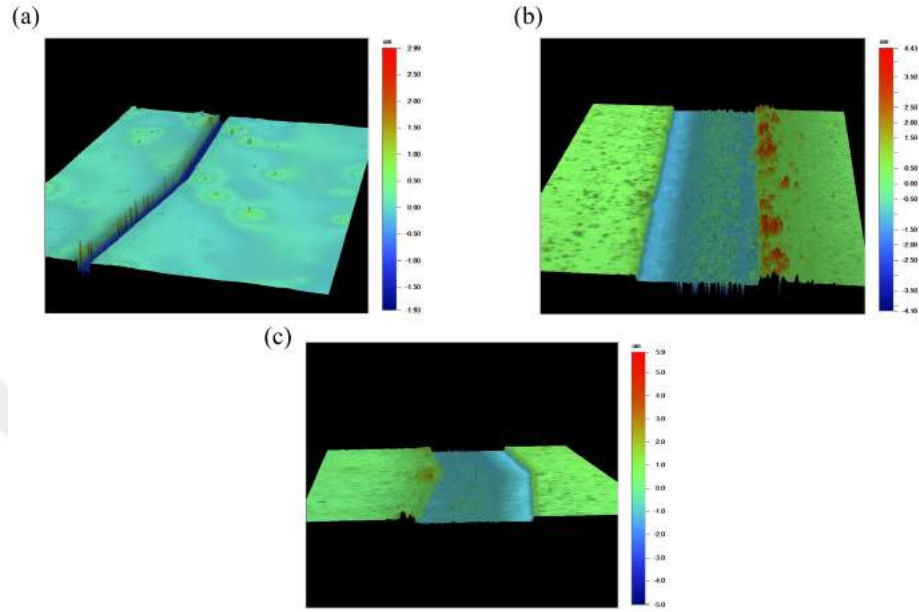


Figure 2.10: White light interferometry images of  $30\mu\text{m}$  wide laser ablated pattern, (a) Portion of ablated pattern (5X objective), (b) Portion of ablated pattern (50X objective), (c) Portion of ablated pattern (50X objective after rinsing with ethanol and DT water. )

junction used for the droplet generation were not altered. The droplets with  $40\mu\text{m}$  and  $60\mu\text{m}$  radii were generated in the top T-junction with flow rates at inlets ( $D_T$ ,  $C_T$ ) set to ( $2\mu\text{L/h}$ ,  $30\mu\text{L/h}$ ) and ( $2.5\mu\text{L/h}$ ,  $20\mu\text{L/h}$ ), respectively. The continuous-phase flow rates at the inlet ( $C_B$ ) for  $40\mu\text{m}$  and  $60\mu\text{m}$  radius droplets were set to  $35\mu\text{L/h}$  and  $45\mu\text{L/h}$ , respectively, while the inlet ( $D_B$ ) was not used. The droplets with  $120\mu\text{m}$  radius were then generated in the bottom T-junction, using flow rates  $D_B = 2\mu\text{L/h}$  and  $C_B = 30\mu\text{L/h}$ . For these droplets, the flow rate at the inlet ( $C_T$ ) was set to  $35\mu\text{L/h}$  and the inlet ( $D_T$ ) was not used. With the above settings of the oil flow rates, similar oil velocities  $U_0$  could be obtained for all studied droplet sizes. In particular, the droplet guiding experiments reported in Figure 2.11 were conducted with the value of  $U_0$  adjusted to approximately  $(450 \pm 10)\mu\text{m/s}$  for both Chips A [Fig. 2.11(a)] and B [Fig. 2.11(b)]. The experimental droplet trajectories denoted by black asterisks were extracted offline from the recorded videos of moving droplets by a particle tracking program using normalized cross-correlation algorithm [Rashid,

2018]. The corresponding simulated trajectories of the droplets were produced by the modeling procedure described in detail above. In Figs. 2.11(a) and 2.11(b), these simulated trajectories are shown as solid red, green and blue lines for 40, 60, and 120  $\mu\text{m}$  droplet radius, respectively. In the simulations, the values of  $\Delta A$  for 40, 60, and 120  $\mu\text{m}$  droplet radius were chosen as 18, 38.5, 46.8  $\mu\text{m}^2$  for Chip A and 39, 72, 108.4  $\mu\text{m}^2$  for Chip B; with these choices of  $\Delta A$ , best agreement between the experiments and simulations could be obtained.

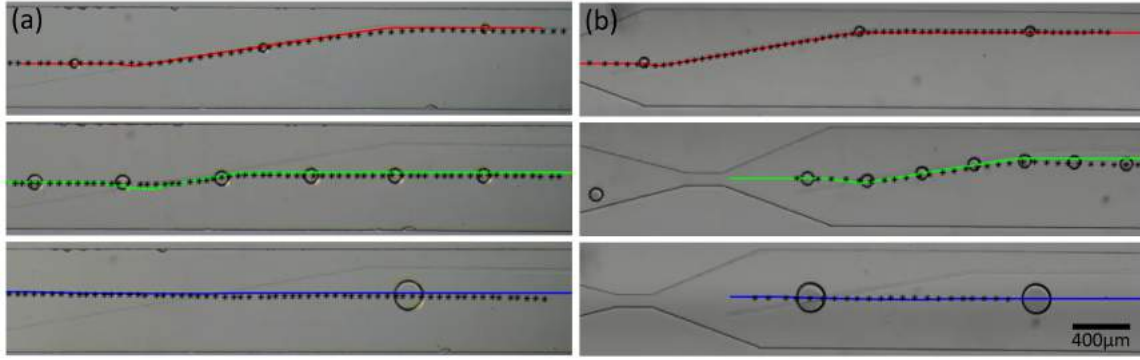


Figure 2.11: Dependence of the stability of droplet guiding on the droplet size. Experimental (black asterisks) and simulated (red, green and blue solid lines) trajectories of aqueous droplets with radii of 40, 60, and 120  $\mu\text{m}$  in (a) Chip A and (b) Chip B. The values of  $U_o$  used for calculating the simulated trajectories were  $U_o = (457, 453, 448) \mu\text{m/s}$  [ $U_o = (449, 452, 459) \mu\text{m/s}$ ] for 40, 60, and 120  $\mu\text{m}$  droplet radius in Chip A [Chip B], respectively.

As evident from Fig. 2.11, for similar values of  $U_o$ ,  $\Delta H$  decreases with increasing droplet size. Hence, more stable droplet guiding is observed for smaller droplet sizes. Specifically, for the smallest studied droplet radius of 40  $\mu\text{m}$ , complete droplet guiding can be reached in both Chip A at  $U_o = 457 \mu\text{m/s}$  and Chip B at  $U_o = 449 \mu\text{m/s}$ , with the respective  $\Delta H$ -values covered by the droplets being 264  $\mu\text{m}$  and 280  $\mu\text{m}$ . On the other hand, at  $U_o \approx 450 \mu\text{m/s}$ , the largest studied droplets with the radius of 120  $\mu\text{m}$  cannot be guided along the laser-ablated tracks in either chip. For these large droplets, the hydrodynamic drag  $F_D$  at the given flow conditions exceeds the confinement force  $F_\gamma$  at all times, pushing the droplets out of the track.

### 2.4.2 Velocity-Based Guiding of Droplets

For the intermediate droplet radius of  $60 \mu\text{m}$ , partial droplet guiding is observed, with  $\Delta H = 40 \mu\text{m}$  for Chip A, and  $\Delta H = 147 \mu\text{m}$  for Chip B. The comparison of the  $\Delta H$ -values obtained for  $R = 60 \mu\text{m}$  droplets in Chip A (guiding track width of  $22 \mu\text{m}$ ) and Chip B (guiding track width of  $30 \mu\text{m}$ ) under similar flow conditions shows that the stability of droplet guiding increases with the increasing width of the guiding track, as indicated by a higher value of  $\Delta H$  observed in Chip B. This is a direct consequence of a stronger confinement force  $F_\gamma$  associated with the wider track.

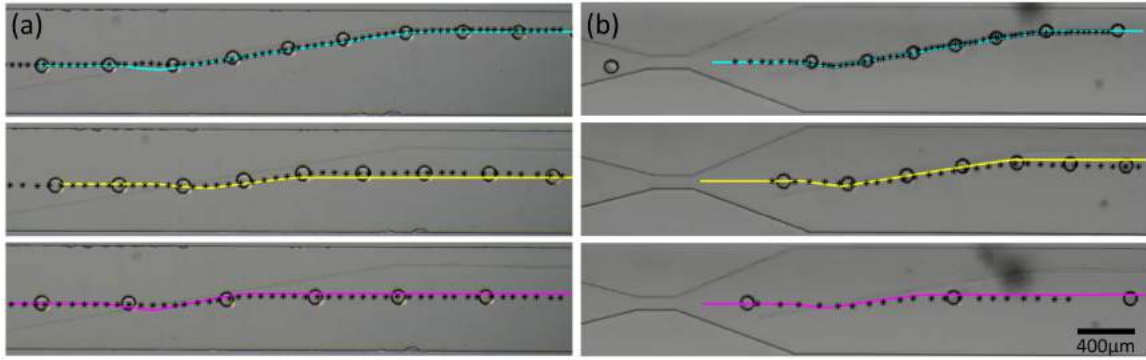


Figure 2.12: Dependence of the stability of droplet guiding on the oil flow speed. Experimental (black asterisks) and simulated (cyan, yellow and magenta solid lines) trajectories of aqueous droplets with radius  $60 \mu\text{m}$  in (a) Chip A and (b) Chip B. The values of  $U_o$  in individual experiments and simulations were  $U_o = (229, 352, 450) \mu\text{m/s}$  for Chip A and  $U_o = (308, 452, 701) \mu\text{m/s}$  for Chip B.

Figure 2.12 shows the experimental (black asterisks) and simulated (cyan, yellow and magenta solid lines) trajectories of aqueous droplets of  $60 \mu\text{m}$  radius guided at different oil flow speeds  $U_o$  along the laser-ablated tracks in Chip A and Chip B. In the simulations, the values of  $\Delta A$  were chosen as  $38.5 \mu\text{m}^2$  for Chip A and  $72 \mu\text{m}^2$  for chip B in order to achieve the best match with the experimental data recorded at the given oil flow speed. For Chip A with the ablated track width of  $22 \mu\text{m}$  [see Fig. 2.12(a)], the values of  $\Delta H$  covered by  $60 \mu\text{m}$  droplets at  $U_o$  equal to 229, 352, and  $450 \mu\text{m/s}$  are 264, 82, and  $40 \mu\text{m}$ , respectively. In contrast, for Chip B with the ablated track width of  $30 \mu\text{m}$  [see Fig. 2.12(b)], the values of  $\Delta H$  covered by  $60 \mu\text{m}$



droplets at  $U_o$  equal to 308, 452, and 701  $\mu\text{m/s}$  are 280, 147, and 48  $\mu\text{m}$ , respectively. Comparison of the corresponding cases of partially guided droplets - indicated in Fig. 2.12 by yellow and magenta colors of the simulated trajectories - shows that at a given value of  $\Delta H$ , droplets in Chip B featuring a wider guiding track can sustain larger flow velocities  $U_o$  in comparison to droplets in Chip A. In other words, at the same flow speed  $U_o$ , droplet guiding in Chip B is more stable (higher value of  $\Delta H$  is achieved), owing to a stronger confinement force  $F_\gamma$  in this chip.

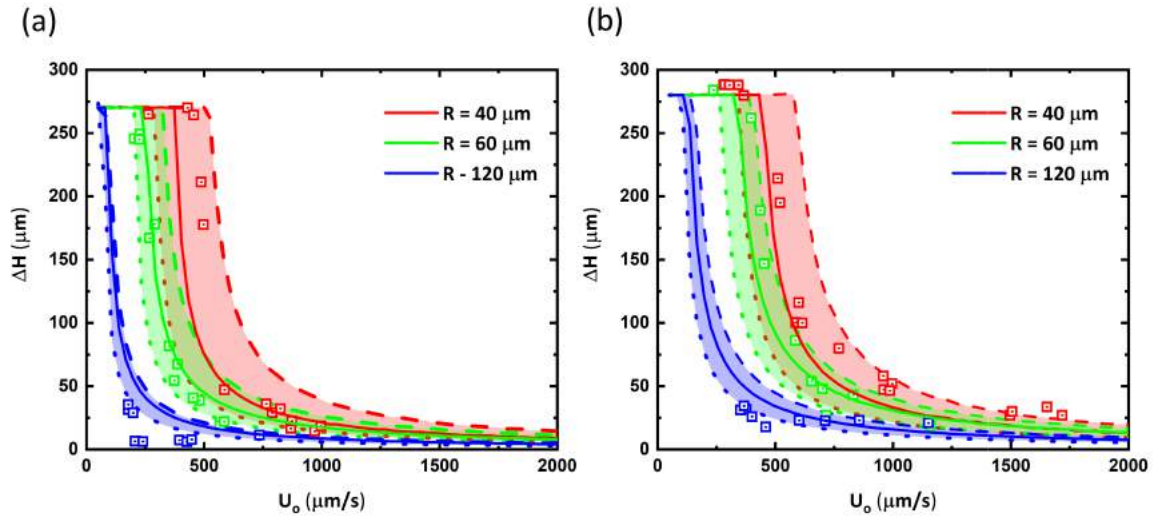


Figure 2.13: Parametric study of the stability of droplet guiding in laser-patterned microfluidic channels. The track exit height  $\Delta H$  is plotted as a function of the oil flow speed  $U_o$  in (a) Chip A and (b) Chip B for droplets with 40  $\mu\text{m}$  (red), 60  $\mu\text{m}$  (green), and 120  $\mu\text{m}$  (blue) radii. Experimental data are shown as colored squares, simulated results are denoted by lines in corresponding colors. In part (a), droplet guiding was simulated for laser ablated patterns with the width of 22  $\mu\text{m}$  and depths of 920 nm (dashed lines), 720 nm (solid lines) and 520 nm (dotted lines), in part (b), droplet guiding was simulated for laser ablated patterns with the width of 30  $\mu\text{m}$  and depths of 990 nm (dashed lines), 790 nm (solid lines) and 590 nm (dotted lines).

## 2.5 Size-Based Sensitivity of Chip

In order to evaluate the stability of guiding for droplets of different sizes moving through laser-patterned microfluidic Hele-Shaw channels at varied speeds of the host

liquid, we carried out systematic guiding experiments whose results are summarized in Fig. 2.13, together with the results of the corresponding simulations of droplet behavior at the given set of system parameters. In particular, Fig. 2.13 shows the dependence of  $\Delta H$  observed for droplets with 40, 60, and 120  $\mu\text{m}$  radii in Chips A and B as a function of the oil flow speed  $U_o$ . For all studied droplet sizes in both chips,  $\Delta H$  monotonically decreases with increasing  $U_o$ , as the hydrodynamic drag  $\mathbf{F}_D$  that pushes the droplets out of the guiding track is directly proportional to  $U_o$ , whereas the confinement force  $\mathbf{F}_\gamma$  that keeps the droplets in the track is independent of the flow conditions. When  $\mathbf{F}_D$  experienced by the droplets exceeds  $\mathbf{F}_\gamma$ , the droplets leave the track. In addition, at any given value of  $U_o$ , the stability of guiding in both chips decreases with increasing droplet radius  $R$ . This trend stems from the fact that  $\mathbf{F}_D$  depends quadratically on  $R$  while  $\mathbf{F}_\gamma$  scales linearly with  $R$ . Experimentally obtained data on the droplet guiding stability shown in Fig. 2.13 as colored squares is complemented by simulations of the droplet behavior denoted by lines in corresponding colors. Because the experimentally measured depths of the guiding tracks display uncertainty, the simulations were carried out for the depths of the guiding track varying from 520 nm (dotted lines) through 720 nm (solid lines) to 920 nm (dashed lines) in Chip A and from 590 nm (dotted lines) through 790 nm (solid lines) to 990 nm (dashed lines) in Chip B. Within these intervals of the guiding track depths, a good agreement between the experiments and simulations is observed for both chips.

The data presented in Fig. 2.13 indicate that at the given flow conditions represented by the value of  $U_o$ , the stability of droplet guiding quantified by the value of  $\Delta H$  depends on the droplet size. This variation in the droplet guiding stability can be then used for size-based sorting of droplets into different streamlines across the Hele-Shaw flow channel. In order to analyze the sensitivity of our size-based droplet sorting technique, we performed CFD calculations of the values of  $\Delta A$  for droplets with 80 and 100  $\mu\text{m}$  radii, in addition to the cases of 40, 60, and 120  $\mu\text{m}$  radii that had been calculated previously, considering droplets moving in Chip B with the ablated track width of 30  $\mu\text{m}$  and depth of 790 nm. Subsequently, we simulated

the trajectories of all considered droplets at varied  $U_o$  and calculated the values of  $\Delta H$  for each individual case; these values are plotted in Fig. 2.14(a) as a function of  $U_o$  for different droplet sizes. In the final step of the sensitivity analysis, we chose several representative values of  $U_o$  and generated a plot of  $\Delta H$  as a function of the droplet radius  $R$ , which is provided in Fig. 2.14(b). Figure 2.14(b) illustrates that there exists an optimal range of values of  $U_o$ , for which the maximal sensitivity in discriminating droplets with different sizes is observed for the given geometry of the microfluidic chip and guiding track. When  $U_o$  is very small ( $U_o < 111 \mu\text{m/s}$ ) or very large ( $U_o > 570 \mu\text{m/s}$ ), either complete or very small droplet guiding is observed, respectively. Hence, those values of  $U_o$  are not well suited for selective sorting of droplets with radii between 40-120  $\mu\text{m}$ . On the other hand, for an intermediate value of  $U_o$  chosen at 429  $\mu\text{m/s}$ ,  $\Delta H$  depends strongly on  $R$  for droplet radii lying between 40-80  $\mu\text{m}$ , suggesting the possibility of efficient size-based separation of droplets within this radius range. Specifically, the observed slope of  $\Delta H/R \approx 5$  translates into a change of 5  $\mu\text{m}$  in  $\Delta H$  upon changing the droplet radius  $R$  by merely 1  $\mu\text{m}$ . By adjusting the parameters of the guiding track (i.e., its width and depth), the high-sensitivity sorting region can be moved to a different interval of the values of  $R$ . Hence, we conclude that our sorting scheme can discriminate between droplets with radii differing by about 1  $\mu\text{m}$ , provided that the geometrical parameters of the guiding track and the value of  $U_o$  are selected properly to match the target range of droplet sizes to be separated.

### 2.5.1 Size-Based Sorting of Merged Droplets

To demonstrate the application of our droplet sorting procedure in a realistic experimental situation, we carried our experiments, in which we separated droplets produced by fusion of two independent droplet streams at the inlet of the Hele-Shaw cell from unfused daughter droplets (see Fig. 2.1(a) for illustration of the used experimental geometry). Such a scenario can arise, for example, in microfluidic chips used for controlled synthesis of a target chemical compound initiated by mixing of

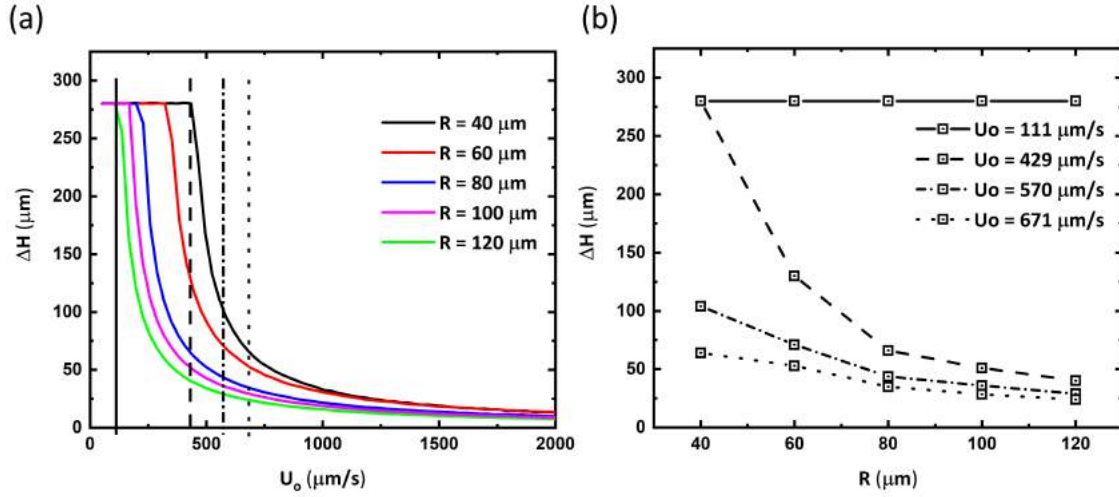


Figure 2.14: Sensitivity of size-based droplet sorting for different flow speeds of the host liquid. (a) Simulated track exit height  $\Delta H$  as a function of the oil flow speed  $U_o$  for droplets of varying radii  $R$  guided in Chip B, assuming the depth of the laser-ablated guiding track of 790 nm. (b) Track exit height  $\Delta H$  as a function of the droplet radius  $R$  for four selected values of the oil flow speed [ $U_o = (111, 429, 570, 671) \mu\text{m/s}$ ] indicated by vertical lines with matching line styles shown in part (a).

two chemically distinct droplets containing the necessary reagents. Figure 2.15 illustrates such a droplet sorting experiment conducted with Chip C, in which the two droplet streams were simultaneously generated at the top and bottom T-junctions with identical geometrical parameters (see Fig. 2.1(a) for details). In order to generate droplets with  $\sim 60 \mu\text{m}$  radii, flow rates into the T-junction inlets were set to  $C_T = C_B = 17 \mu\text{L/h}$  and  $D_T = D_B = 1 \mu\text{L/h}$ . As shown in Fig. 2.15, droplets that arrive simultaneously at the inlet of the Hele-Shaw flow channel fuse. The resulting fusion droplets with  $\sim 100 \mu\text{m}$  radius are not guided by the guiding track and move through the flow channel without deflection, while the unfused  $60 \mu\text{m}$  daughter droplets are completely guided by the ablated guiding track. At time  $t = 0$  s, the droplet labeled 3 is observed to be fully guided along the track while two other droplets labeled 1 and 2 are about to fuse at the tapered region of the microfluidic device. At time  $t = 2$  s, the droplets labeled 1 and 2 complete their fusion, proceeding through the chip as a single larger droplet labeled  $1+2$  that subsequently leaves the track at  $t = 8$  s without

being guided, owing to its size associated with large fluid drag that overcomes the confinement force keeping the droplet in the track. The whole process then repeats with the two droplets labeled 4 and 5 simultaneously approaching the channel inlet at time  $t = 8$  s that are seen to fuse at time  $t = 12$  s, forming a large fusion droplet  $4+5$ .

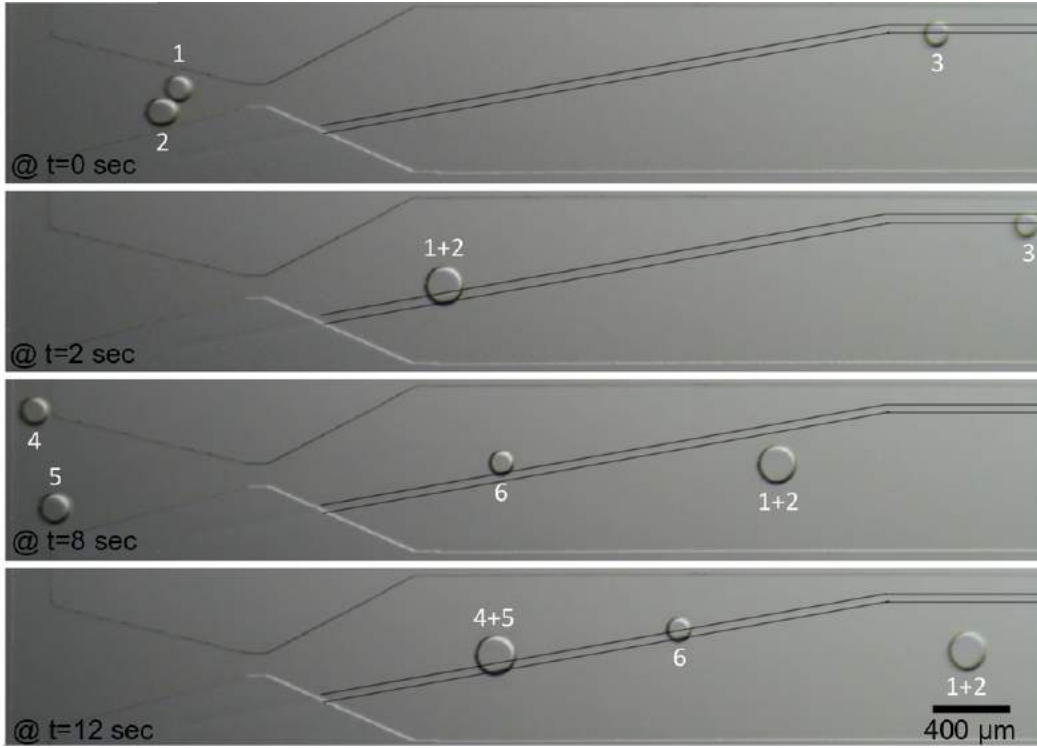


Figure 2.15: Experimental demonstration of size-based sorting of unfused and fused droplets formed at the inlet of a Hele-Shaw flow channel. Time-lapse images illustrate the trajectories of several droplets through the channel. While the smaller unfused droplets follow the laser-ablated guiding track, larger fused droplets proceed through the channel without being deflected by the track.

Table 2.3: The list of cases investigated via CFD

Radius [ $\mu\text{m}$ ]	Droplet to Track Position	Track Width [ $\mu\text{m}$ ]	Track Depth [nm]	$\varepsilon_A$	$A_{corr}$ [ $\mu\text{m}^2$ ]	Absolute Area Error [%]
40	Away	-	-	0.117%	16731	0.03%
60	Away	-	-	-0.013%	32926	0.04%
120	Away	-	-	0.031%	111672	0.04%
40	On	30	990	0.174%	16677	-
60	On	30	990	-0.026%	32824	-
120	On	30	990	0.013%	111438	-
40	On	30	790	-0.044%	16716	-
60	On	30	790	0.061%	32840	-
120	On	30	790	-0.021%	111477	-
40	On	30	590	0.035%	16700	-
60	On	30	590	0.045%	32859	-
120	On	30	590	-0.015%	111518	-
40	On	22	920	0.145%	16694	-
60	On	22	920	0.088%	32859	-
120	On	22	920	-0.020%	111545	-
40	On	22	720	0.060%	16705	-
60	On	22	720	-0.016%	32874	-
120	On	22	720	0.002%	111555	-
40	On	22	520	0.100%	16711	-
60	On	22	520	-0.065%	32885	-
120	On	22	520	-0.026%	111580	-
80	On	30	790	0.033%	54031	-
100	On	30	790	-0.007%	80237	-

## Chapter 3

# MICROFLUIDIC CHIP DESIGN FOR 3D CELL CULTURING

Microfluidics system is the technology that process and manipulate very small amounts of fluids such as ( $10^{-9}$  to  $10^{-18}$  liters) having microfluidic channels dimensions ranging from tens of micrometers to a millimeter [Whitesides, 2006]. Microfluidics technology have visible advantages over common platforms, such as high resolution and sensitivity, detection, low fabrication cost, less amount of sample consumption and less generation of waste, shorter analysis time, and small device footprint [Reyes, 2002]. Study of biomolecules and medial applications demands reduction in the dimensions of scientific technology and the systems to reduce the sample volume, separate particles and defect free molecules. Theoretically, new prospects can be explored in a well controlled manner and with accurately verifying using the modeling , for example, the behavior of the liquid flow inside a thin channel, studying the surface tension effect on micro scale and capillary effect etc. Many scientists and researches strongly believe that progress in microfluidics technology will revolutionize not only chemical processes but also the modern research approach towards the complex studies in cell biology. Microfluidics is multi-disciplinary research area with applications ranging from biotechnology, biochemical processes [Chován, 2002], forensic analysis [Verpoorte, 2002], tissue engineering [Andersson, 2004], cell-based biosensors [Park, 2003], drug delivery [Jain, 2004] and embryology [B.Wheeler, 2006]. The advancement in microfabrication technology biology community has greatly benefited as it opens ways for new approaches to investigate and observe cells in microenvironment which closely mimics the in-vivo conditions. Microfluidic based cell culture systems provide new capabilities for continuous monitoring of dynamic processes, such as the

control of biomolecules and cells concentrations and angiogenesis, at high spatial and temporal resolution in a well controlled microenvironment [Vickerman, 2008].

### **3.1 Microfluidic chip design for angiogenesis**

Complex behavior of factors that influence metastasis in humans can not be mimicked completely neither in vivo nor in vitro. Studies have been done to understand Cancer cell invasion, cell migration, and endothelium cells interactions comprising various stages of cancer metastasis. Studies of cancer metastasis are mostly limited to in vivo mouse models. There is a deficiency of tumor models and methods to study these processes in vitro. In acknowledgement of the necessity for a new generation of in vitro platforms, which is optically accessible and mimicking physiological conditions in better manner through controlled-microenvironments. Using the benefits of the emerging technology of microfluidics, it has led us to open paths to try new testing methodologies of in vitro studies. While knowing that in vitro systems cannot completely replicates the complexity of in vivo situation, although this technology allow an opportunity to create organ-specific microenvironments and to explore the progression of metastasis of various cancer types, including migration through gels as well as real-time imaging of invasion and extravasation. The microenvironment is described by small distances to nutrient flow, a 3-dimensional (3D) scaffold, and the presence of multiple cell types in proper spatial relationship. These features can be achieved by present microfabrication techniques and can be merged with proper cell culture protocols. The significant benefits of micro-scale cell culture systems or microfluidic bioreactors are their ability to use lesser quantities of cells and reagents, meticulous control of spatiotemporal habitat and high resolution visualization of cellular events in real-time.

The use of microfluidic cell cultures to characterize the response of multi-cellular systems in vitro has gained traction in the experimental study of a variety of biological processes, including angiogenesis [Stroock, 2010, Shamloo, 2010, Sudo, 2009, Vickerman, 2008], neuronal growth and development [Kothapalli, 2011, Liu, 2008, Bonvin,



2010], immune cell responses [Irimia, 2006] and micro-tissue cultures [Domansky, 2010b]. Studying cells migration is important in numerous physiological and pathological processes, such as healing of wounds, inflammation, creating of new blood vessels from the existing blood vessels and cancer metastasis [Chung, 2009a] the evaluation in microfabrication techniques and approaches to employ and monitor the environment of the cells which mimics the in vivo conditions [Vickerman, 2008]. Microfluidic system is getting popular with in the cell biology community, in 2D microfluidic systems cells are seeded on a substrate coated with the media that supports cell growth such as PDL, fibronectin, mertigel etc. This 2D microfluidic systems have provided new insights into the cellular and molecular mechanisms of cell migration [Verbridge, 2010]. However, it is necessary to study cell migration on 3D quantitatively, as 3D models has the potential to mimic the physiologically relevant microenvironment of living tissues in vivo precisely, compared to 2D culture models [Even-Ram, 2005]. Researchers are now agreeing that many crucial biological subtleties may be missed in 2D cell culture models and are in pursuit for an alternate approaches that incorporate a 3D gel or a matrix. In vitro microenvironment is combination of local as well as global behavior that can be classified as biophysical or biochemical in nature. Biochemical factors can be steady or time dependent depending on solubility factor and diffusion in scaffolds. The cells are seeded either inside the 3D scaffold or to the side of scaffold. The biophysical factors includes porosity, density and stiffness of the scaffold along with with the behavior related to the flow, either in the form of surface stress or flow around the cells. In vitro models for cancer metastasis investigated cancer cell invasion and cells migration across extracellular matrix of different types under various mechanical and/or chemical cues [M.Mercurio, 2001]. Some studies focused on interactions between two different cell types by modeling cancer cell binding to the endothelium, with focus on the changes imposed in cell morphology and biomechanical properties [Mierke, 2011]. Microstructure hydrogels used in modeling and monitoring processes such as angiogenesis, cancer metastasis, interactions of different cells, mechanisms based on the 3D development and proliferation of cells were also

studied [Song, 2009]. The most frequently used is collagen of type I, which contains all necessary proteins in the structure of the extracellular matrix that supports cell adhesion and growth inside and on top of EC matrix. One of the most prominent system is the microarray based system used by a variety of cancer researches such as angiogenesis and intravasation, developed by Roger Kamm group from MIT [Farahat, 2012, Aref, 2013, Sudo, 2009, Vickerman, 2008]. The microfluidic systems, collagen gel is trapped into the middle channel by creating a collagen cage using the surface tension mechanism created by microstrips/micropillars placed in the middle of the collagen channel or at the boundaries of the center channel to confine the collagen gel inside the microfluidic chip. Solutions containing cells are injected/pipetted on one side of the collagen to cultivate the cells on the collagen surface. Then, a chemical gradient is obtained by injecting/pipetting various chemicals or cells that trigger angiogenesis on the other side of the collagen, and the responses and angiogenic potentials of the cells that are cultured on the collagen surface against these chemicals can be observed [Sudo, 2009, Farahat, 2012]. The parameters such as the properties of the materials used to trap the hydrogel into the middle channel in a desired way, the distance between the microstructures/micropillars and the edge angles of the micropillars play a major role in the confinement of the collagen. A test platform was developed to test antiangiogenic drugs using these microarray. However, one of the biggest disadvantages of this system is that the surface area where cells can interact with collagen is limited due to the necessity to place microarray frequently [Farahat, 2012]. The microfluidic system design used for studying angiogenesis phenomena is based on the putting the biochemicals that initiate angiogenesis inside the chip. Furthermore, due to the microfluidic system design it is not possible to grow tumor spheroids inside the microfluidic chip rather tumor spheroids will be injected inside the chip at the time on loading the collagen.

In this chapter, we proposed a novel microfluidic chip design that over come the limitation of the earlier designs. i) no microstructures or micropillars used for confinement of collagen gel, which provides a continuous surface area for the interaction

of cells with the matrix. ii) microwell structures for growing tumor spheroids inside the microfluidic chip. By adding these two features in the design a study of tumor spheroids induced angiogenesis can be conducted in vitro inside a microfluidic chip.

## **3.2 Materials and method**

### *3.2.1 Microfluidic system*

In this study we designed two different types of microfluidic chips for understanding 3D microenvironment of different cell types. The first design of our microfluidic chip is used for conducting experiment that need special biochemical to induced specific type of behavior such as angiogenesis, cells migration and capillary morphogenesis. The second chip is designed specifically to grow tumor spheroids inside the microfluidic chip and to use endothelial cells as an indicator or sensors that responds to the chemicals secreted by these tumor. Endothelial cells can serve as an indicator for the angiogenic potential of different types of tumor spheroids as different type of tumor spheroids will secrete different type of biochemicals.

### *3.2.2 Microfluidic chip design for biochemical triggered angiogenesis*

The microfluidic chip designed for studying the angiogenesis phenomenon by biochemical stimulation, contains two parallel side channels for injecting cells and cell culturing medium at first place and then stimulus when needed. The third channel is a central collagen loading channel which is used for injecting the collagen solution which after gelation becomes a scaffold and stays there for cell support and controlled diffusion. There are no side micro-pillars provided in this design for caging the collagen which is used in previous studies [Jeon, 2014] rather we used capillary action and surface tension effect which provides a virtual cage and confinement for housing the collagen scaffold inside the microfluidic chip. One primary aim was to facilitate the incorporation of most widely used biological compatible and injectable cell culture scaffolds *i.e. hydrogels*, which may be biologically derived *i.e. collagen gels or*

*Matrigel TM* or synthetic *i.e. self-assembling peptide gels* [Chen, 2008]. Collagen or hydrogel loading channel height is kept less than the side channels which provides the ease of loading and confinement of the gel due to capillary action and surface tension effect. To use a range of hydrogel concentrations the gel cage geometry was optimized, with the less height of the collagen channel provides the physical support and stability to the soft gel.

Figure. 3.1 shows the schematic of the microfluidic master mold designed for injecting stimulus directly from one of the side channels. The width of the collagen confinement region is  $3000\ \mu\text{m}$  and the length of the channel is  $6800\ \mu\text{m}$ . No side micro-pillars are used for confining the collagen inside the microfluidic chip. The width of the two side channels, one for loading cells for growth and the other for providing cell growth medium or biochemicals/stimulus depending on the experiment phase, is  $1000\ \mu\text{m}$  and length is approximately  $19000\ \mu\text{m}$ . In order to minimize the flow resistance and the force induced on the collagen scaffold, the stream lines of inflow medium are kept parallel to the collagen gel interface. The two side channels are isolated from each other through the extracellular matrix *i.e.* through collagen/hydrogel scaffold. The two side channels can only transfer their contents through the collagen gel in between them by diffusion. This allows the establishment of gradients in both pressure and chemo-tactic factors across the gel.

Figure. 3.2 shows the design of microfluidic chip master mold. Fig. 3.2 (a) shows the 3D view of the chip with middle region as collagen loading channel and two side channels one for biomolecules/stimulus and other for cell growth. These biochemicals such as VEGF-A, Ang-1 etc are introduced directly in the biochemical channel which diffuses through the collagen scaffold and reaches the cells in the opposite cell growth channel. Fig. 3.2 (b) Shows the cross-sectional view of the microfluidic chip clearly showing the height of the middle region is less than the side channels. This difference in channels height causes the capillary action in the central collagen loading channel, which along with the surface tension effect helps in loading of the collagen in fluid form and keeping the collagen in the middle region. The collagen remains in the

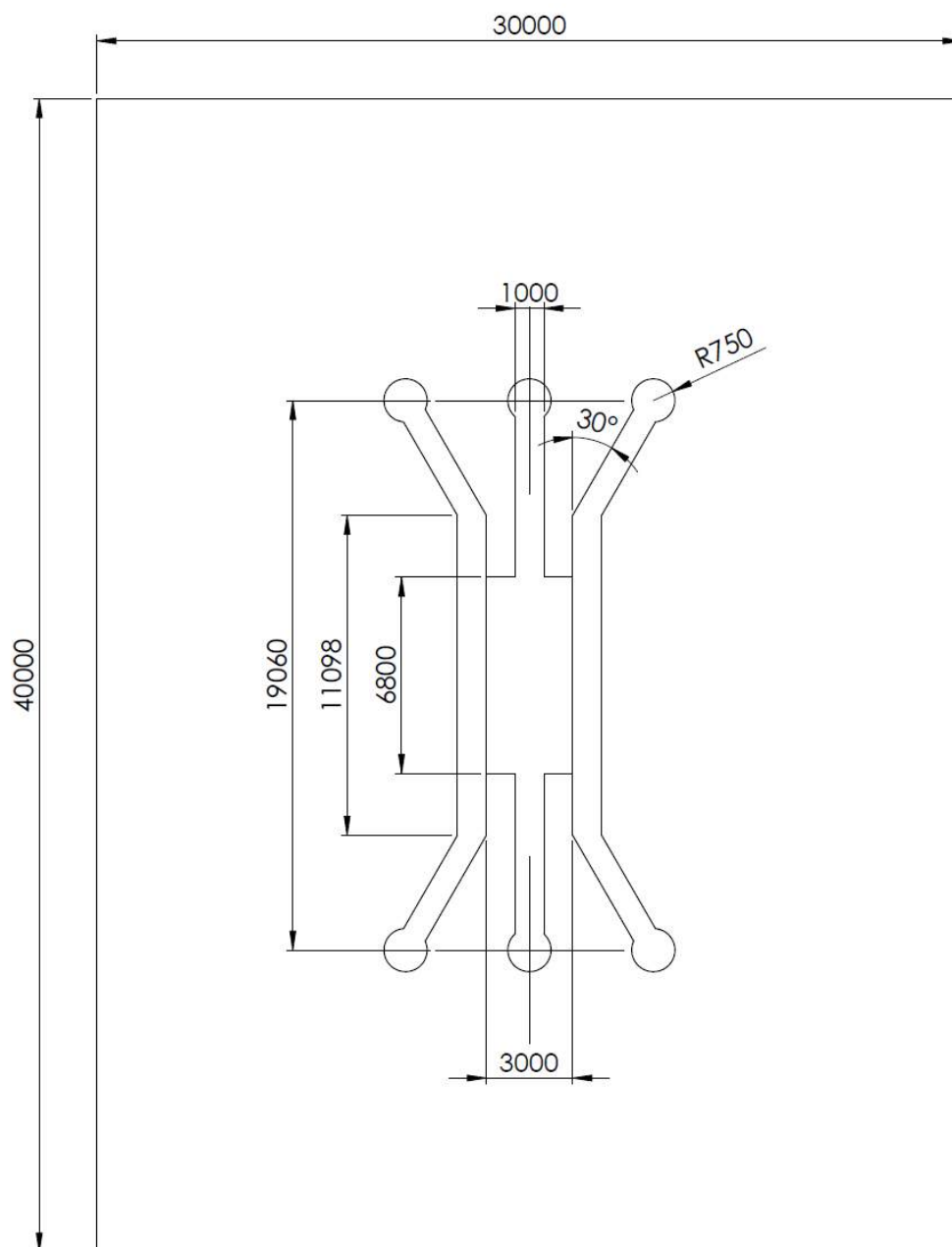


Figure 3.1: Schematic of microfluidic chip designed for direct injection of stimulus.

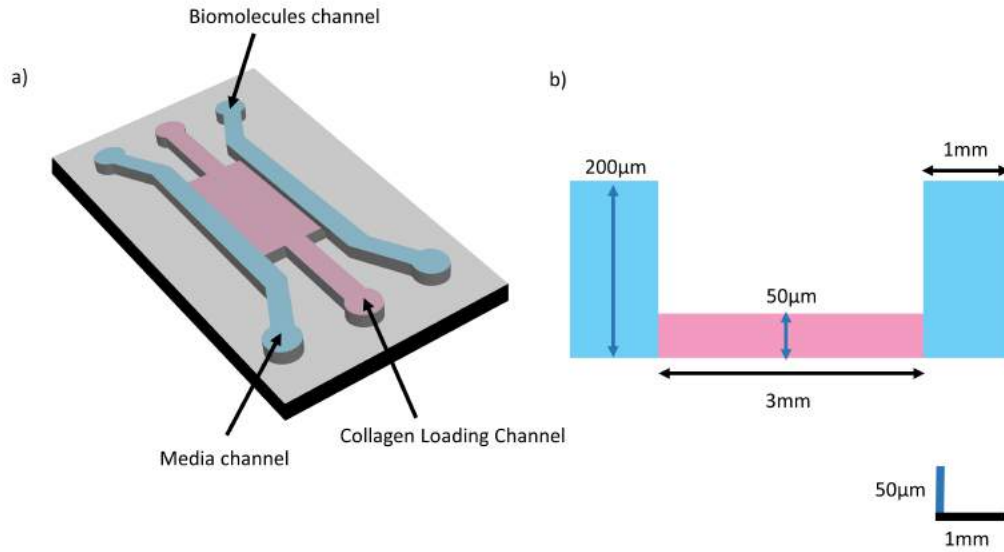


Figure 3.2: The design of a microfluidic chip for direct injection of biochemical/stimulus from one of the side channel, (a) 3D view of the microfluidic chip, (b) cross-sectional view of the microfluidic chip, showing the difference in the height of the channels.

collagen loading channel after gelation. R.kammet al. designed microfluidic chip having micropillars in the center channel or on both sides of the channel loading channel for confining the collagen. The entire microfluidic platform was designed to be small enough to fit on a microscope slide which then allow real-time monitoring of cells over the course of the experiment.

### 3.2.3 Microfluidic chip design for growing tumor spheroids

The need of growing tumor spheroids inside a microfluidic chip is to study the tendency of different tumor spheroids in triggering endothelial cells sprouts to understand angiogenic potential. Endothelial cells injected inside the microfluidic chip from the cell growth channel (side channel) will be used as a indicator showing the potential of different tumors to stimulate angiogenesis. We believe that different types of tumor spheroids will have different strengths to induce endothelial cells sprouts. One way

to study angiogenesis is to grow tumor spheroids outside the chip and once they form a tumor clump then it is transferred to the microfluidic chip. In such type of analysis the tumor spheroids are mixed with the collagen and is then loaded in the collagen channel along with the scaffold. The disadvantage of this method is you can not control the number of tumor spheroids inside a collagen on a chip and also you can not control the position of the tumor spheroid, the placement of the tumor spheroid is totally random. With the proposed design tumor cells will be loaded in the tumor cell channel, where the cell traps will trap tumor cells. The cells after being trapped in the micro-wells/micro-traps will grow and form a tumor spheroid. The unwanted cells or untrapped cells will be washed without disturbing the cells inside the micro-wells as the flow will not disturb them. The microfluidic chip consists two parallel channels and in between is the collagen loading channel. Similar to the previous design no side micro-pillars provided for caging the collagen rather the same concept of capillary effect and surface tension is used which provide a virtual cage for housing the collagen scaffold inside the microfluidic chip. Gel loading channel height is less than the side channel which provides the ease of loading and confinement of the gel. Side pockets are provided in the collagen channel whose height is equal to the side channel height. This less height of the collagen channel provides the physical support and stability to the soft gel. Due to the capillary effect the collagen is filled in to the less height region providing an opportunity for the tumor cells to grow in spheroid in the side pockets.

Figure. 3.3 shows the schematic of the microfluidic master mold design of the chip used for growing tumor spheroids and studying the angiogenic potential of tumor spheroids. Endothelial cells seeded in the other channel are used as an indicator for angiogenic potential of these spheroids. The width of the collagen confinement region is  $3000\ \mu\text{m}$  and the length of the channel is  $6800\ \mu\text{m}$ . The side pockets are polygon shaped with spacing of  $1\ \text{mm}$  and the dimension of  $300\ \mu\text{m}$ . The width of the side channels used for loading cells and cell growth medium is  $1000\ \mu\text{m}$  and length is approximately  $19000\ \mu\text{m}$ . Similar to the previous design to minimize the

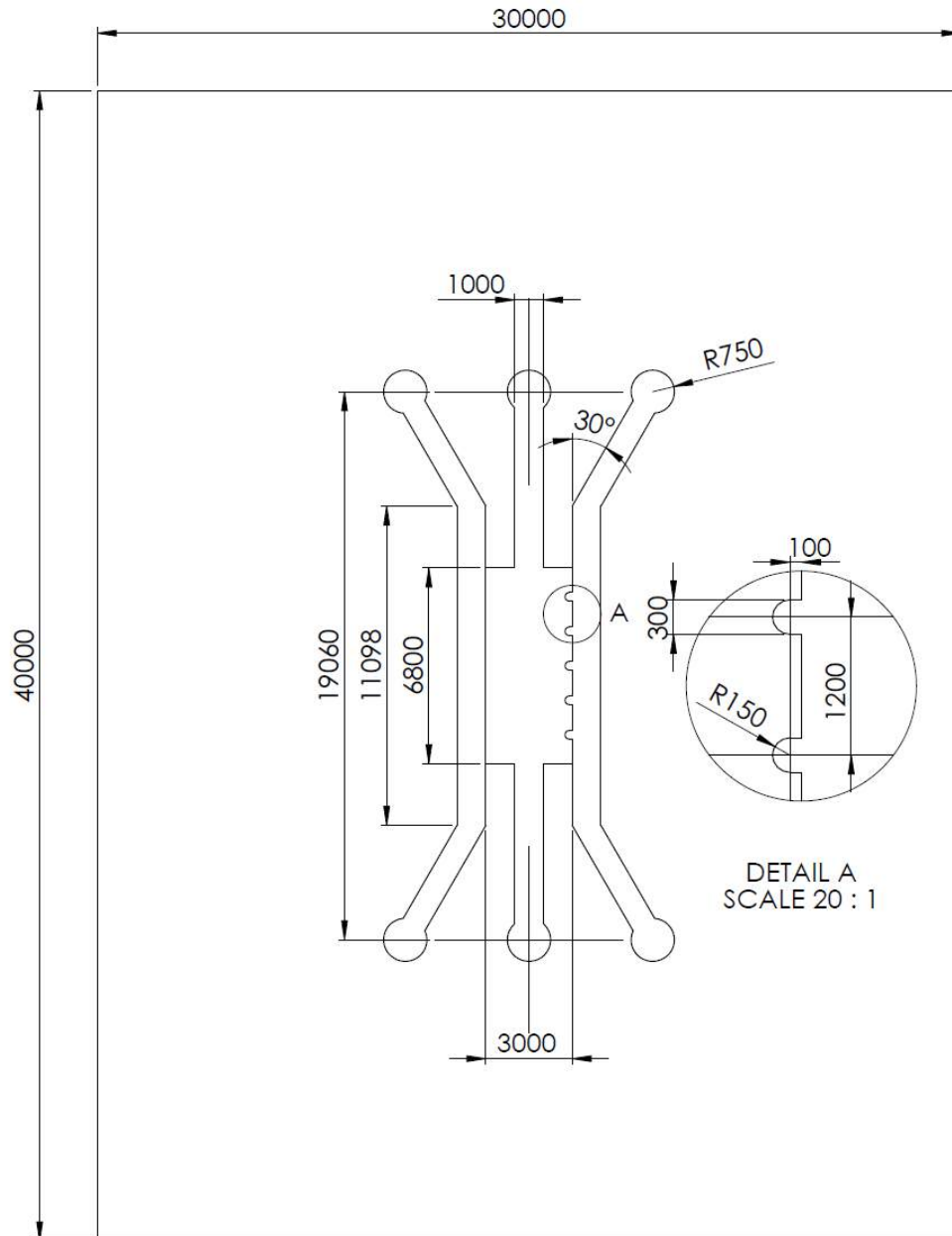


Figure 3.3: Schematic of microfluidic chip for growing tumor spheroids on chip



flow resistance and the force induced on the collagen the stream lines of of flow medium are kept in parallel to the walls of the collagen gel. Collagen extracellular matrix serves as an isolation between two channels. The only mean of communication between two side channels is through this collagen. This collagen in between permits the establishment of gradients in both pressure and chemotactic factors across the gel.

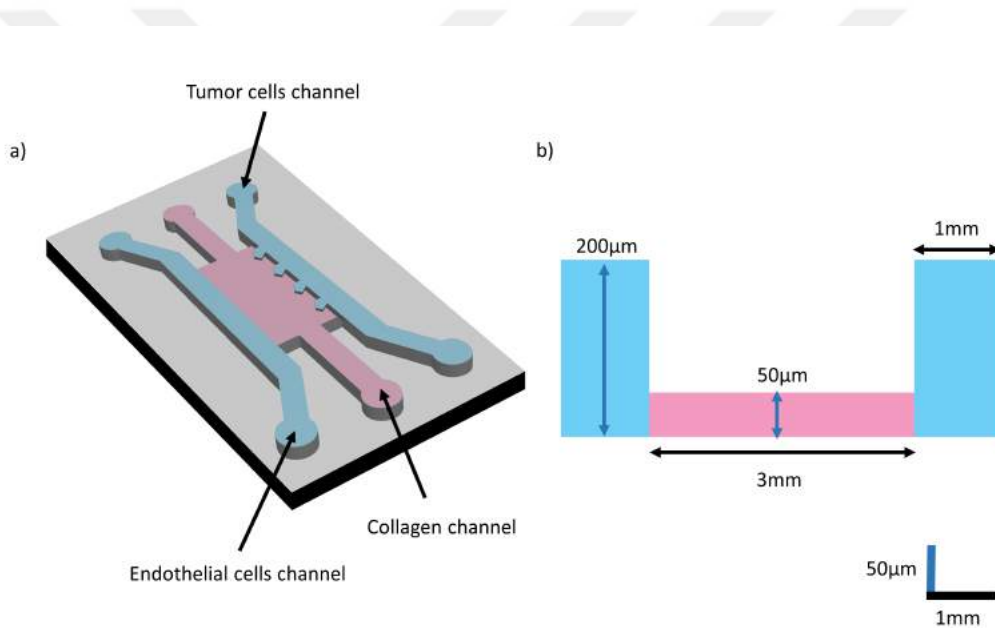


Figure 3.4: Microfluidic chip design for growing tumor spheroids on a chip for studying angiogenic potential of tumor spheroids, (a) 3D view of the microfluidic chip, (b) cross-sectional view of the microfluidic chip.

Figure. 3.4 shows the design of microfluidic chip master mold for tumor spheroids dependent studies. Fig. 3.4 (a) shows the 3D view of the chip with middle region as collagen loading channel with pockets on one side and two side channels one for endothelial cells growth and other for growing tumor spheroids on chip. These tumor spheroids secretes biochemicals such as VEGF-A, Ang-1 etc, which will diffuse through the collagen. Once these biochemical are received by the endothelial cells they will respond by producing sprouts in the direction of higher gradients. Fig. 3.4 (b) Shows the cross-sectional view of the microfluidic chip clearly showing the height of the

middle region is less than the side channels. This difference in channels height causes the capillary effect in the collagen loading channel, which along with the surface tension effect helps in loading of the collagen in fluid form and keeping the collagen in the region. The collagen stays in the collagen loading channel after gelation. In order to convert liquid collagen to gel the chip is incubated for 30 min under 37°C.

### **3.3 Microfluidic chip fabrication and surface modification**

#### *3.3.1 Master mold preparation for microfluidic chip*

Master mold for microfluidic chip was designed by two methods, i) using sticky aluminum tapes and ii) using CNC machining. Aluminum tapes made master mold was designed due to its ease of preparation and the changes needed to optimize the design can be easily implemented. Once the design was finalized the master molds were produced using CNC machining. Designing master mold using aluminum tapes was done using two layers approach. Figure. 3.5 Shows the design approach used for the master mold.

Figure. 3.5 (a) Shows the first layer of the master mold. The height of this layer is approximately 80  $\mu\text{m}$ . This layer defines the general design of the microfluidic chip with two side flow channels and central collagen loading channel. On top of this layer a second layer of aluminum tape is placed, precisely cutted according to the dimensions designed by the first layer, shown in Fig. 3.5 (b). This layer only contains the design of the two side channels to give the elevation. This difference in heights of the central collagen loading channel and the two side channels gives rise to the capillary effect phenomenon. Fig. 3.5 (c) Shows the complete design of the master mold. The black and gray colored channels shows the height difference with the height of the side channels more than the middle channel. Fig. 3.5 (d) Shows the image of the actual chip master mold which is used for the preparation of elastomer (PDMS) chips.

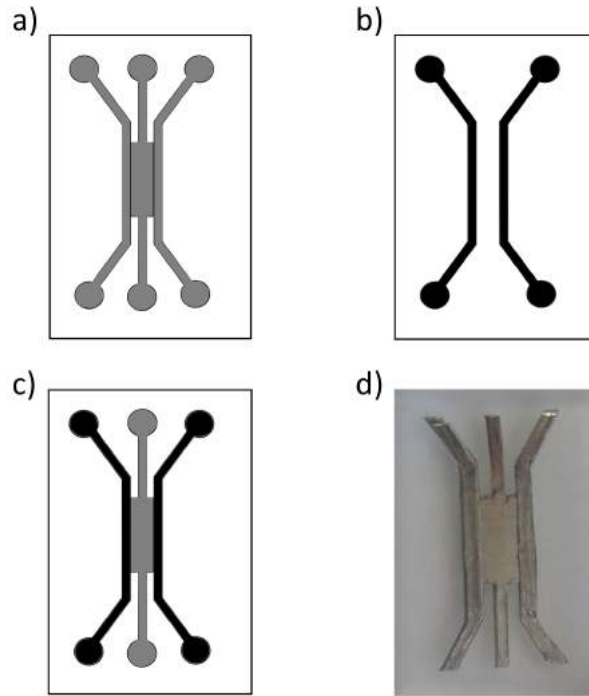


Figure 3.5: Designing master mold using aluminum tape, (a) first layer of aluminum tapes defining the general design of the microfluidic chip, (b) second layer of the side channels, (c) putting second layer of side channels on the general design layer for introducing the height difference between the side channels and the central collagen loading channel, (d) aluminum tape made two layer master mold.

### 3.3.2 PDMS chips preparation methodology

The fabrication process of PDMS (poli-dimethyl siloxane) on PDL coated glass was illustrated in Fig. 3.6.

The master mold shown in Fig. 3.6 (a) was initially fabricated using two layer design of aluminium tapes. The master mold was salinized in a vacuum chamber for 24 hours by using HMDS (hexa-dimethyl siloxane), this helps in peeling off the PDMS stamp. PDMS material made using the pre curser and the curing (Sylgard 184, Dow cronig co.) mixed in weight to weight ratio of 10:1. Mixing pre-curser and curing agent makes many bubbles which were removed using desiccation. After removal of air bubbles from the mixture it was then poured on top of the master mold

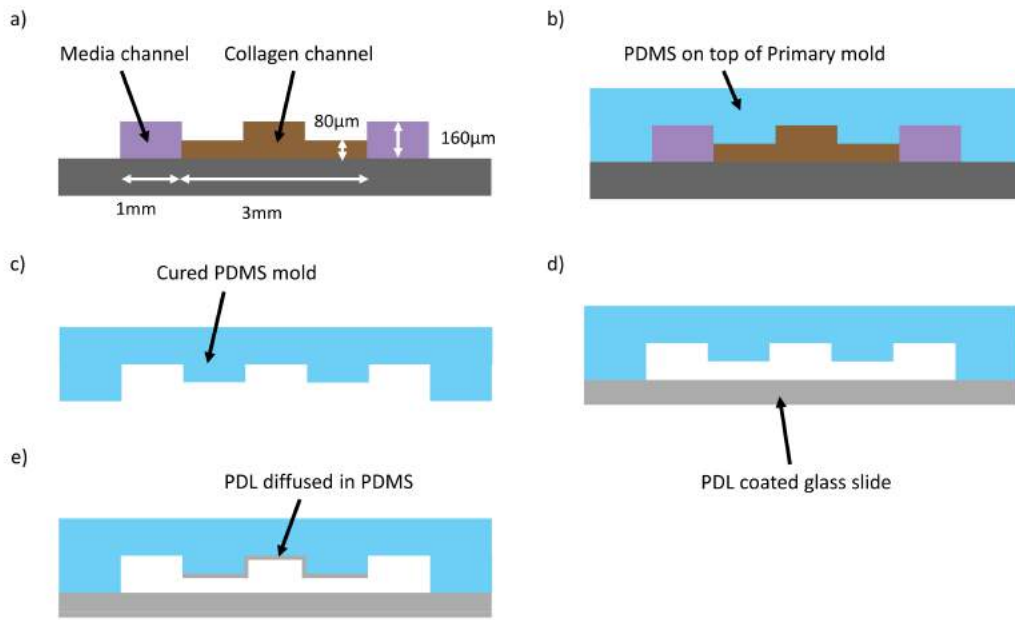


Figure 3.6: Illustration of stamping method for making microfluidic chips

and was kept in oven under 65°C for 1 hour as shown in Fig. 3.6 (b). Fig. 3.6 (c), Shows PDMS is peeled off from the master mold after curing, the cured PDMS has taken the shape of the master mold. The PDMS stamp is bonded to the PDL coated microscope glass side as shown in Fig. 3.6 (d). PDMS is hydrophobic in its self, in order to bond it to the PDL glass surface, the PDMS surface should be converted to hydrophilic by using oxygen plasma (Plasma treatment). Both PDMS stamp and PDL coated microscope glass slide were treated in oxygen plasma for 60 sec in the presence of 100 percent oxygen and were then placed on top of each other. Due to hydrophilic surface, they are attracted to each other and are tightly bonded. The bonded chip is then putted in oven for 72 hours under 65°C for slightly hydrophobic recovery. After hydrophobic recovery the chips are ready to be tested directly or can be treated with PDL to increase the collagen binding to the PDMS surface.

### 3.4 Results and discussion

#### 3.4.1 Testing the collagen loading channel with ink water

The microfluidic chips were tested for the confinement of fluid in the collagen channel to verify the concept of the chip design. A 20  $\mu\text{l}$  of ink was injected in the collagen loading channel using a pipette. The loading of the ink using pipette was done very gently so that no ink leaks in to the side channels. Fig. 3.7 shows that the ink followed the central collagen loading channel very nicely. This is due to the capillary effect caused by the less height of the collagen loading channel and the surface tension effect at the ink/water and air interface inside the microfluidic chip, which does not allow it to leak in to the side channels.

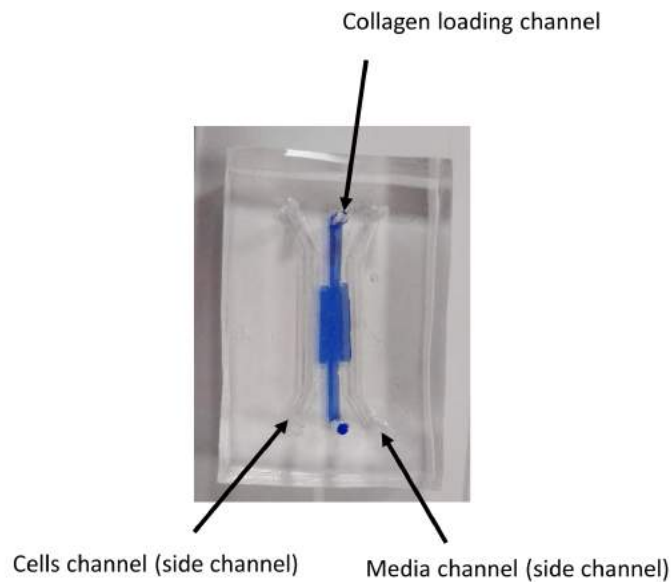


Figure 3.7: Collagen channel testing using ink to show the confinement by collagen loading channel.

Computational Fluid Dynamics (CFD) methods were used with experimental methods in the design of PDMS based microfluidic chips. Collagen solution remains only in the desired regions within the microfluidic chip, depending on the surface tension

forces and fluid pressure acting on the collagen-air interface. CFD analysis is firstly considered as two-phase which will be used to determine the geometry and flow rates required for the collagen to be confined only to the desired volume. The examination of the flow of these channels to collect tumor spheres only in the desired volumes will play an important role in determining the details of the channel design.

### *3.4.2 CFD simulations for confining water in the collagen loading channel*

Ansys Fluent commercial software based on finite volumes method was used for CFD analysis. Analyzes for collagen filling was handled as three-dimensional, time-dependent, laminar and two-phase. Although there are multiple numerical methods for tracking the liquid-gas interface in the biphasic flow, Volume of Fluid (VOF) method will be used in these analysis because it allows for the modeling of complex liquid-gas interfaces and is frequently used in the literature. The characteristic dimensionless numbers in these microprocessing problems are the Reynolds Number indicating the ratio of the surface tension forces to the inertial forces and the Capillary Number indicating the ratio of the inertial forces to the viscous forces and play an important role in determining the numerical methods to be used. Low tensions in the Capillary and Reynolds ( $Ca \ll 1$ ,  $Re \ll 1$ ) surface tensions are dominant. The VOF explicit diagram and wall adhesion forces of Continuum Surface Force (CSF) were used to model these surface tensions and the interaction of the interface with the walls with sufficient accuracy. Model parameters selected for high accuracy limit the greatest time step available. Therefore, a large number of time steps have to be solved, which in turn increases the cost. In the numerical part of the preliminary study, water was injected from the entrance section as in the microfluidic chip. The water-to-air two-phase flow is modeled in a smaller control volume, similar to existing micro-flow in microfluidic chips. The structural solution network was used in the analysis and the cell sizes were formed from 4  $\mu\text{m}$  uniform cubes and the time step was chosen to change dynamically to keep the Courant Number at 0.5. Since the bottom wall is glass, the contact angle (CA) is  $30^\circ$ , while all other wall surfaces are

PDMS material, the contact angle (CA) was defined to be  $100^\circ$ . Non-slip boundary condition is applied on all walls. Figure. 3.8 shows the volume fraction contours (@  $z = 40 \text{ fm}$ ) taken at two different time steps of the analysis and the shape of the liquid-gas interface.

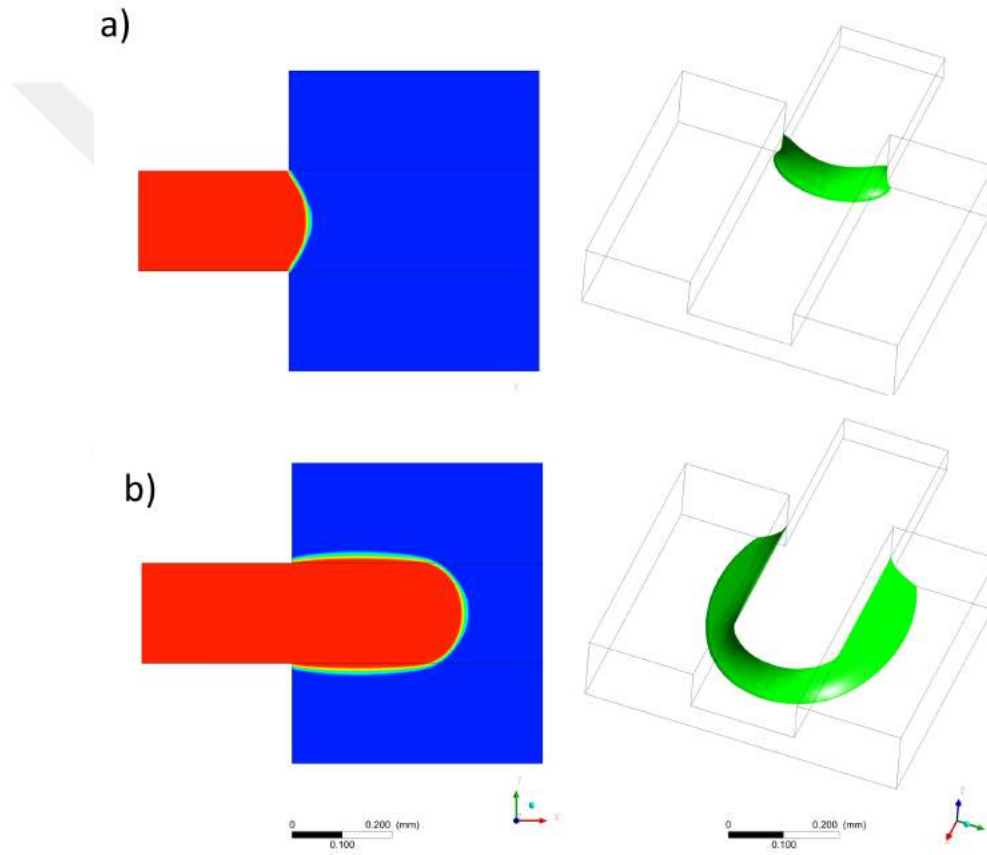


Figure 3.8: Volume fraction of water flowing inside the collagen loading channel, CFD simulation, (a) shows the volume fraction of water flow in 2D (left) and 3D image (right) of the water flow inside the microfluidic chip at 0.01 sec. (b) shows the 2D (left) and 3D (right) images of water flow inside the microfluidic chip at 0.09 sec.

Figure. 3.8 shows the volume fraction images of the water flow inside the collagen loading channel inside the microfluidic chip to verify the confinement of fluid inside the microfluidic chip. Figure. 3.8 (a) show the loading of water inside the collagen loading channel at 0.01 sec in 2D and 3D. The water follows the middle collagen loading channel with out leaking to the side channels as shown in Figure. 3.8 (b). In

this simulation two phase flow is used by considering air and water as two different fluids. Water is represented in red color and air as blue color in volume fraction images. As the bottom substrate of the microfluidic chip is glass with contact angle (CA) of  $30^\circ$ , we see slight spreading as compared to the top surface which is PDMS having contact angle of  $100^\circ$ . Figure. 3.7 shows that the ink followed the collagen channel with out any leakage to the side channels.

### 3.4.3 Collagen preparation and loading inside a microfluidic chip

The collagen after gelation plays a vital role in cells growth as they provide a base for cells to either grow on top of it or grow inside it. For cells to grow inside a collagen hydrogel, its pH should be neutral *i.e.* neither acidic (1-6) nor basic (8-14). The ideal value for cell growth is approximately pH 7.4 and at this value the color of collagen solution is light pink. For our experiments we prepared the collagen solution according to the recipe mentioned in table 3.1. The light pinkish color of the collagen solution indicates that the pH is in the range 7.4 - 7.6, which is safe for cells growth.

Table 3.1: Collagen recipe.

Ingredients	Volume( $\mu$ l)
10x DMEM	10.5
1M NaoH	3.5
NaHCo3 (7.5%)	1.5
1x DMEM	19.5
Collagen (3.6 mg/ml) Rat-tail type 1	125
Total volume	160

Table 3.1 shows the protocol for preparing 2.8 mg/ml collagen. Fabrication of collagen was conducted inside a sterile hood. All the ingredients mentioned in 3.1 were kept in ice. Also the ependorff tube used for preparation of collagen was pre-chilled. All the ingredients are mixed in the order mentioned in the tale. After adding collagen



the mixture is pipetted carefully to avoid any bubble formation. After pipetteing the mixture is kept in ice before loading the collagen solution inside the microfluidic chip.

#### 3.4.4 Collagen loading inside the microfluidic chip

After preparing the collagen solution, it is loaded in the collagen loading channel by using 10  $\mu$ l pipette. First collagen solution was injected from one inlet of the collagen loading channel till the collagen solution reaches the middle of the collagen loading channel then from the other inlet another 10  $\mu$ l collagen solution was injected to the point when both collagen solution merges. The reason for doing this method is to avoid leaking of collagen to the side channels and to fill the collagen in the collagen loading channel completely.

#### 3.4.5 Treating the PDMS surface with Poly-d-lysine (PDL)

Figure. 3.9 Shows the the difference between the PDL treated and not treated microfluidic chips.

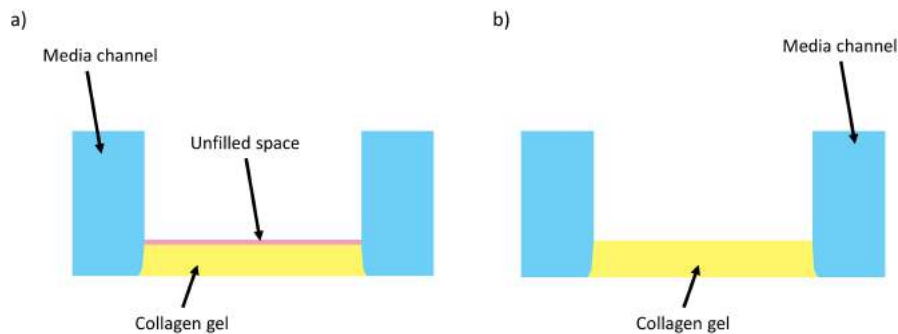


Figure 3.9: Treating microfluidic chip with PDL, (a) untreated microfluidic chip, (b) PDL treated microfluidic chip.

As shown in Fig. 3.9 (a) the collagen solution after gelation leaves a very narrow space in between the collagen gel and PDMS top layer. This narrow space provides an easy path for the fluid from the side channel to pass through the collagen gel and reach the other media channel rather than reaching the other media channel

through diffusion in collagen. As suggested by [Sudo, 2005] PDL treatment enhance the adhesion of the collagen to the PDMS. Fig. 3.9 (b) shows the improved loading of collagen after PDL treatment. PDL is positively charged, PDL treated channels enhance adhesion to the negatively-charged collagen scaffold. [Chung, 2009a]. This hypothesis was verified by measuring the adhesive strength between a collagen coated AFM tip and PDMS plates treated by either collagen or PDL. Adhesion strength between the collagen coated AFM tip and the PDMS plate treated by PDL was  $(7.45 \pm 0.31)$  nN, while that between the collagen coated AFM tip and the PDMS plate treated by collagen was  $(4.2 \pm 0.15)$  nN. PDL (poly-D-lysine hydrobromide; 1 mg/ml; Sigma–Aldrich, St. Louis, MO) surface treatment solution was introduced to the collagen loading channel and incubated at 37°C for 12 hours. The PDL was then aspirated from the microfluidic chip, washed with sterile water, and dried at 80°C for 24 hours for rendering the channel surface hydrophobicity and for confining the filled gel scaffold within the collagen loading region. It is shown in Fig. 3.9 (b), that after PDL treatment no air gap is left in the collagen loading channel which was causing leaking of the media or trapan blue.

#### 3.4.6 collagen durability test

To check the durability and to confirm that collagen stays intact with the top and bottom surface, experiment was conducted by putting trapan blue in one of the media channel and check for leaking of trapan blue from the inserted channel to the other channel.

Figure. 3.10 shows the experiment conducted using trapan blue to verify that there is no leaking or no gap is present between the collagen scaffold and PDMS layer in the microfluidic chip after treatment of PDL. Fig. 3.9 (a) Shows no leaking when trapan blue was injected in to the side channel immediately after the collagen gelation. Fig. 3.9 (b) shows the images of the chip after 4 hours incubation under 37°C and then trapan blue is added in the side channel. As it can be seen that after 4 hours there was no leaking and the collagen gel is in contact with the PDMS top

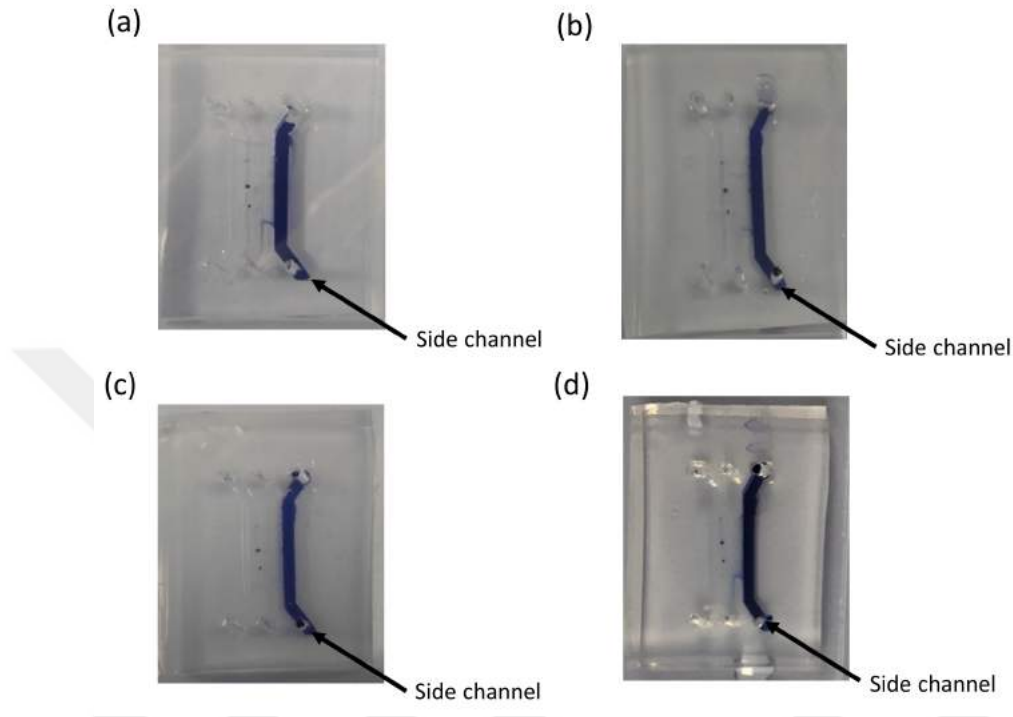


Figure 3.10: Collagen durability test with collagen concentration 2.8 mg/ml, (a) trapan blue test in one of the side channel immediately after collagen gelation, (b) after 4 hours of incubation trapan blue is introduced in the same side channel, (c) trapan blue test after 1 day incubation, (e) trapan blue loaded in the same side channel after 4 days of incubation.

surface. Once the image is recorded, the microfluidic chip was washed with PBS and incubated till next test. The microfluidic chip after 1 day of incubation was injected with trapan blue in the same side channel as shown in Fig. 3.10 (c) the collagen was found intact with the top PDMS surface and bottom glass surface. Fig. 3.10 (d) shows the experimental image repeated after 4 days. It is found that even after 4 days there was no leakage in the chip, collagen was confined in its defined region and it is in good contact with the top PDMS and bottom glass surface. The above experiment confirms the treating the collagen loading channel of the microfluidic chip with PDL improves the binding of the collagen/hydrogel scaffold inside the microfluidic chip.

### 3.5 Experiment with Mesenchymal Stem Cells(MSCs)

#### 3.5.1 Experiment with Collagen type-1

MSCs plays a vital role in repair and regeneration of tissues by secreting growth promotion factors. MSCs are selected for testing the microfluidic chip stability due to its rapid growth and multiplicity. MSCs were grown in a cell culture plate and were constantly feed till its confluency reaches approximately 90 percent. Fig. 3.11 (a & b), shows the image of MSCs cultured in 2D cell culture plate with confluency of more than 90 percent.

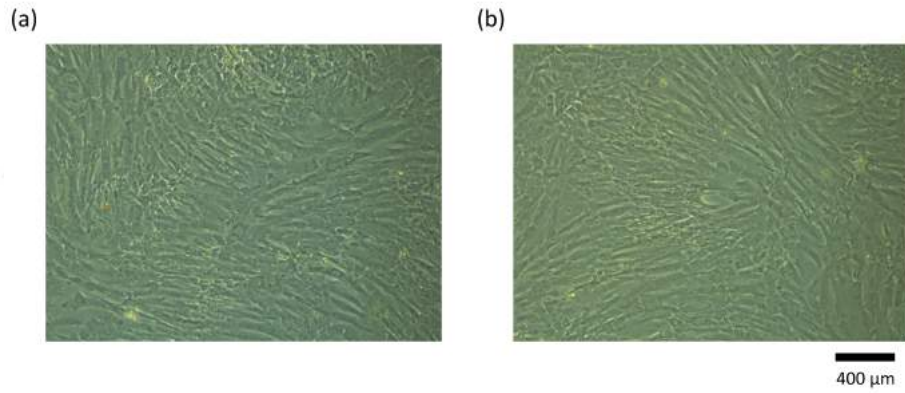


Figure 3.11: Mesenchymal stem cells (MSCs) cultured on a 2D cell culture plate with confluency more than 90 percent.

Figure. 3.12 shows the model of the microfluidic chip experiment with mesenchymal stem cells seeded in one of the side channel referred as cell growth channel. The MSCs are very active cells and like the collagen in its microenvironment so they attaches to the collagen-medium interface quickly and starts to increase in number. For MSCs to grow inside a collagen, no external stimulus is needed that grow by themselves. Only the cells growth medium is needed to be changed repetitively with one day interval. In the cell channel, shown in Fig. 3.12 cells settled down and started to grow in side the collagen, represented as the elongations.

We studied the cell migration of mesenchymal stem cells (MSCs) in collagen type-1 inside the microfluidic chip over the span of time. The collagen pH value was in

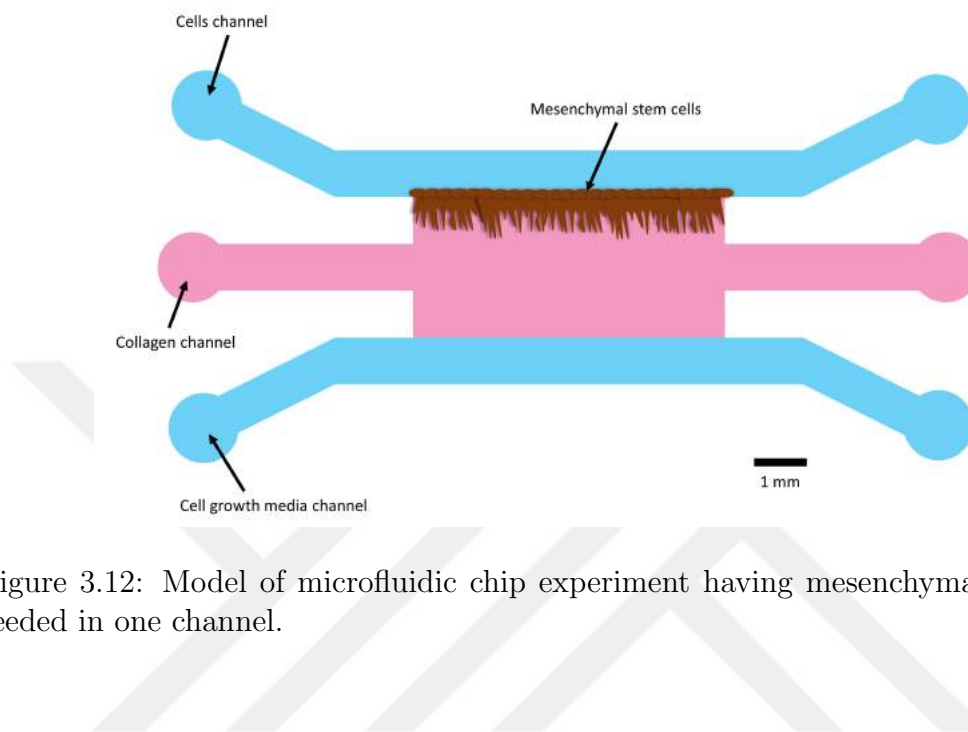


Figure 3.12: Model of microfluidic chip experiment having mesenchymal stem cells seeded in one channel.

the range of 7.4 - 7.6 and concentration was 2.8 mg/ml. We injected approximately 200,000 - 300,000 cells in the cells growth channel. The other media channel was filled with cells growth media. Figure.3.13 shows the growth of cells growth inside a microfluidic chip in collagen. Fig. 3.13 (a) shows the cells injected immediately after the formation of gel inside the microfluidic chip. it can be seen that their exist a nice boundary of cells and the cells does not enters the collagen neither from top nor from the bottom. After cells were seeded inside the microfluidic chip the chips were tilted at 90 degrees so that cells settle down on the collagen to attach on it. Fig. 3.13 (b) shows the image recorded after 4 hours of tilting the microfluidic chip. Most cells settle down on the side wall of the collagen. After 4 hours of tilting the chips a blob of cells growth medium was putted on all the channel inlets and outlets. This helps in maintaining the protein concentration in the media channel inside the microfluidic chip. Fig. 3.13 (c) Shows the image recorded after 48 hours of cell seeding inside the microfluidic chip. It can be seen that cells are growing in the microfluidic chip and are perfusing inside a collagen. After each 24 hours the cells growth media was changed and the chips were incubated. Fig. 3.13 (d) Shows the cells growth after 72 hours of its seeding. The cells are growing further inside the collagen and its disctaced covered

inside collagen is increased. Fig. 3.13 (e) shows the middle collagen region inside a microfluidic chip and Fig. 3.13 (g) shows its respective collagen region near the cells seeding channel after 120 hours of incubation. It can be seen that as the incubation time increases the cells grows more inside the collagen. Fig. 3.13 (f) and Fig. 3.13 (h) shows the middle collagen region and collagen area near the cells seeding channel after 168 hours. The cell are active and reached the other side channel.

### 3.5.2 Experiment with other hydrogel *i.e.* HyStem-HP cell culture

HyStem-HP cell culture (HYSHP020-1KT, sigma-aldrich) is known as a starting point for optimizing the metrix that support cell culturing in studies where the release of biochemical *i.e.* growth factor, at slower rates is important for stem cells. This hydrogel has three chemical components *i.e.* HyStem-HP, Gelin-S and Extralink. The presence of thiol-modified heparin in HyStem-HP allows the slow release of growth factors (GF). The sites for basic cell attachment of cell lines and primary cells is provided by Gelin-S. This hydrogel can be used as a basic scaffold for 3D cell growth for stem cells.

we used this hydrogel inside a microfluidic chip to study the behavior of mesenchymal stem cells in 3D micro-environment.

#### *HyStem-HP cell culture preparation procedure*

- 1) Reconstitute HyStem-HP in 1 ml of degassed water.
- 2) Reconstitute Gelin-S in 1 ml of degassed water.
- 3) Reconstitute Extralink in 0.5 ml of degassed water.

The Solutions remain liquid at temperature between 15 °C and 37 °C. The formation of hydrogelis dependent on the addition of the crosslinking chemical *i.e.* extralink. This extralink is added to the mixture of HyStem-HP and Gelin-S. The gelation is independent of temparature or pH value, it occurs after 20 min when the extralink is added to the solution.

*Experiment with mesenchymal stem cells*

After preparation of Hystem-HP hydrogel its was loaded in the microfluidic chip in collagen loading channel. As it is neither temperature sensitive or pH sensitive as it gelifies in approximately 20 min when extralink is added, to be on safe side we putted it inside the incubator under 37 °C for 30 min. After this time the microfluidic chip was ready for cell seeding. Cells which were trypsinized and re-suspended were injected using a 10  $\mu$ l pipette. The cell count was approximately 35000 in 10  $\mu$ l for cell medium. The other side channel was filled with cell growth media. Media was putted on all inlets and were then incubated with repeatedly change of medium every day. Fig. 3.14 shows the images of MSCs captured from the microfluidic chip at different days of the experiment.

*3.5.3 Hystem-HP hydrogel durability test*

To check the durability Hystem-HP and to confirm that this hydrogel stays in contact with the upper PDMS and lower glass surface, experiment was performed by injecting trapan blue in one of the media channel.

Figure. 3.15 shows the experimental results performed using trapan blue to verify the leaking and durability of the hydrogel inside a microfluidic chip. Fig. 3.15 (a) Shows that no leaking when trapan blue was injected in to the side channel immediately after the collagen gelation. Fig. 3.15 (b,c) shows the images of the chip after 4 hours before adding trapan blue and after adding trapan blue. The concentration of trapan blue was increased in order to clearly monitor the behavior of the chip. As it can be seen that after 4 hours there was no leaking and the collagen gel is in contact with the PDMS top surface. Once the image is recorded the chip was washed with PBS and incubated till next test. Fig. 3.15 (d) shows the experimental image repeated after 5 days. It is found that even after 5 days there was no leakage in the chip and collagen was confined in its region.

#### 3.5.4 Immunofluorescence (IF) staining of MSCs inside a microfluidic chip

Fig. 3.16 shows the fluorescence stain confocal images of the mesenchymal cells inside a microfluidic chips for collagen and Hystem-HP hydrogel. The nucleus of the cells were stained with DAPI having excitation and emission wavelength 405/450 nm. The actins were stained with Phalloidin–FITC (green fluorescence) having excitation and emission wavelength 488/525 nm. Some cells in a microfluidic chips were also stained by Vimentin (In Rabbit) (red fluorescence) having excitation and emission wavelengths 532/568 nm. Fig. 3.16 (a,b) shows the staining of the mesenchymal stem cells inside a collagen. we can see very nice fluorescence for all. It is observed that when the cells starts to grow inside a collagen the Vimentin starts to lose its fluorescence. When MSCs interacts with the collagen the perfuse inside it and continues its growth. On the other hand fig. 3.16 (c,d) shows the fluorescence images of the MSCs when they interacts with the Hystem-HP hydrogel. It is observed that the cells grows nicely in the cell channel but none of them entered inside the hydrogel. Hystem-HP hydrogel is known to be liked by MSCs in 2D culturing but from the experiment performed in 3D microenvironment it seems that either the porosity of the Hystem-HP hydrogel is too small or the cells like to grow on the surface rather than entering inside the hydrogel.



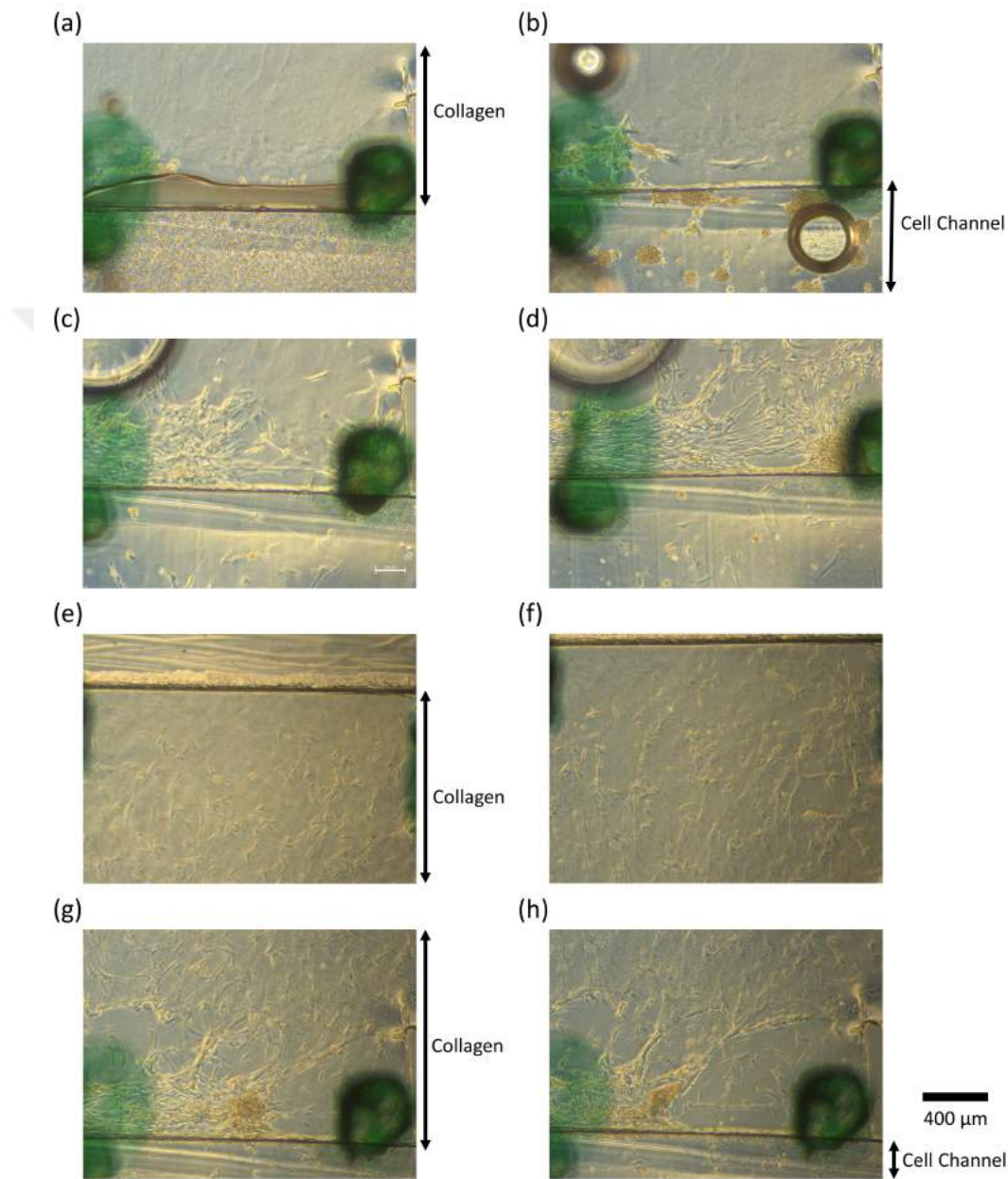


Figure 3.13: MSCs growth inside a microfluidic chip, (a) MSCs seeded immediately after hydrogel gelation, (b) microfluidic chip with cells after 4 hours of incubation, (c) MSCs after 48 hours of gelation and seeding, (d) MSCs after 72 hours of cells seeding inside a microfluidic chip, (e) Middle region of collagen channel showing MSCs after 120 hours of cells seeding inside a microfluidic chip, (f) Middle region of collagen channel showing MSCs after 168 hours of cells seeding inside a microfluidic chip, (g) MSCs after 120 hours of cells seeding inside a microfluidic chip, (h) MSCs after 168 hours of cells seeding inside a microfluidic chip.

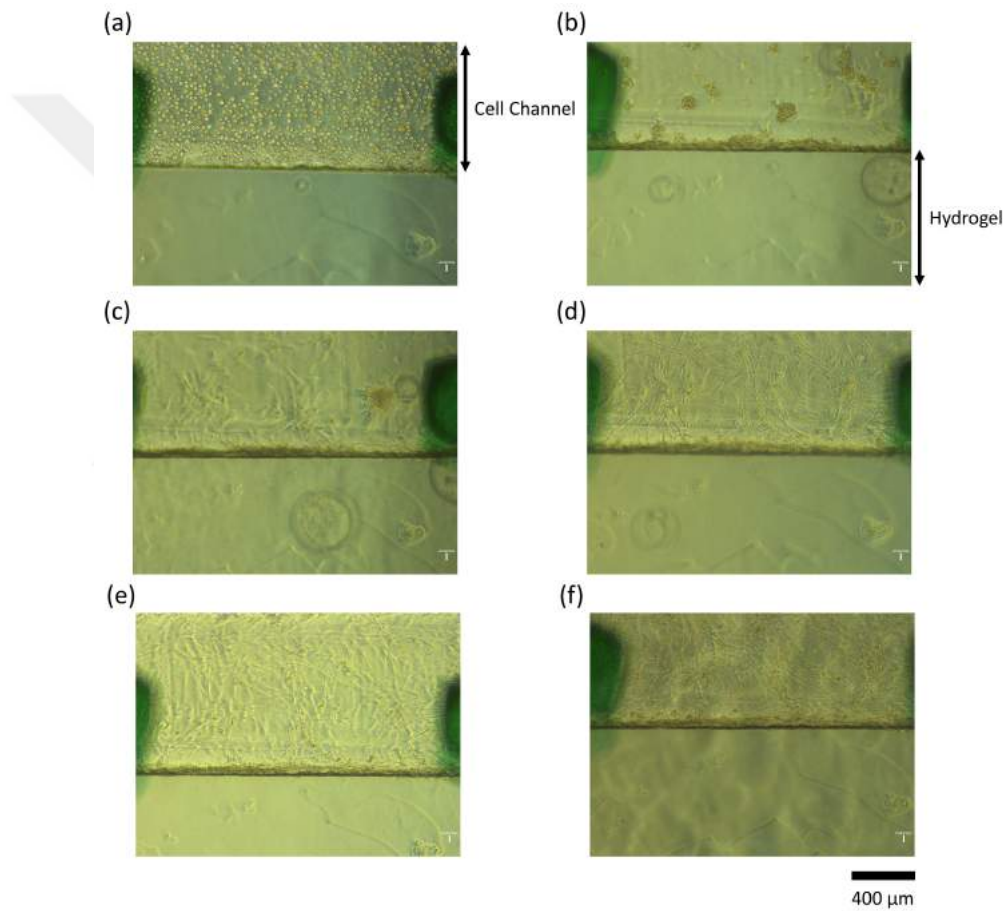


Figure 3.14: MSCs growth inside a microfluidic chip, (a) MSCs seeded immediately after hydrogel gelation, (b) microfluidic chip with cells after 4 hours of incubation, (c) MSCs after 24 hours of gelation and seeding, (d) MSCs after 72 hours of cells seeding inside a microfluidic chip, (e) MSCs after 96 hours of cells seeding inside a microfluidic chip, (f) MSCs after 144 hours of cells seeding inside a microfluidic chip.

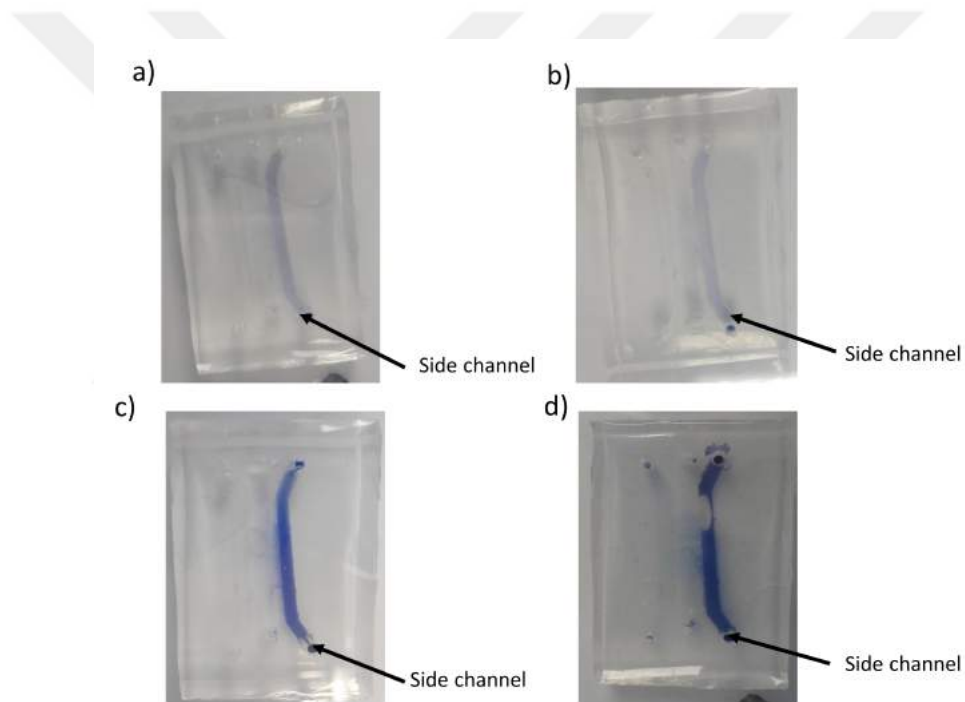


Figure 3.15: Hystem-HP durability test inside a microfluidic chip using trapan blue, (a) trapan blue test in one of the side channel immediately after collagen gelation, (b) after 4 hours of incubation before trapan blue is introduced in the same side channel, (c) adding trapan blue after 4 hours incubation, (d) trapan blue loaded in the same side channel after 5 days of incubation.

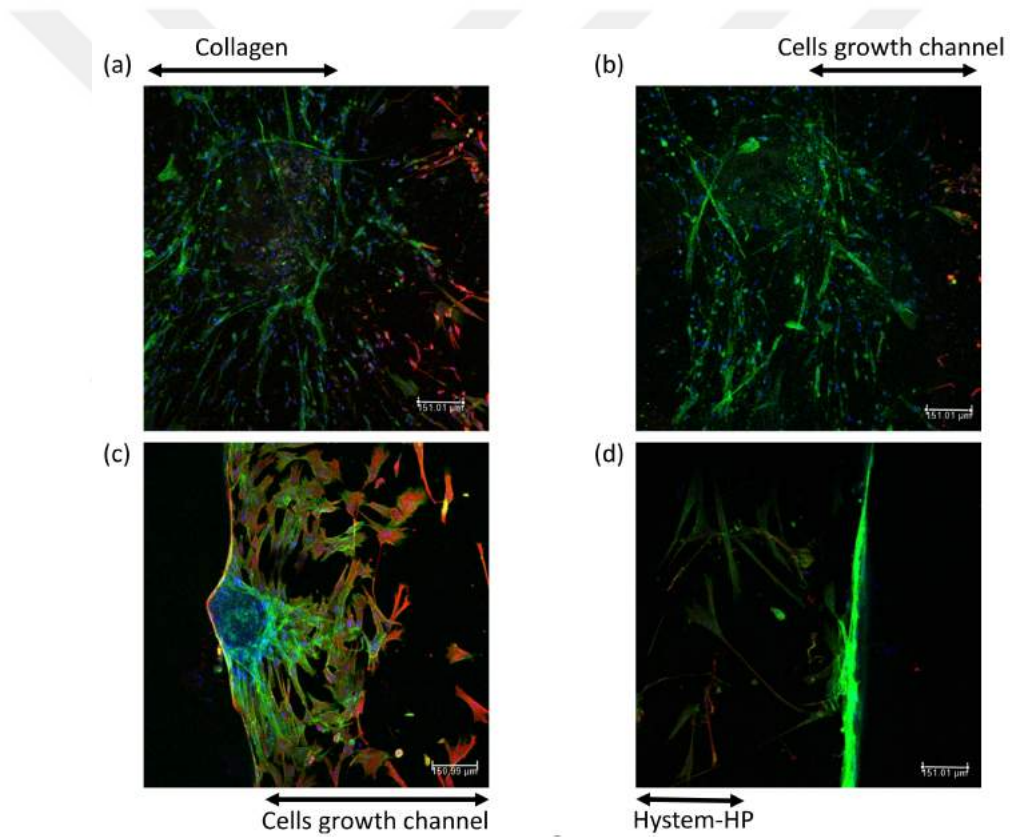


Figure 3.16: Fluorescence stained actins (green), tubulins (red) and nucleus (blue) MSCs, (a & b) MSCs in collagen type-1, (c & d) MSCs in Hystem-HP hydrogel.

## Chapter 4

### ANGIOGENESIS IN 3D MICROENVIRONMENT

#### *4.0.1 Angiogenesis*

Angiogenesis is a greek word with “angêion” means “vessel” and “genesis” means “emergence”. Angiogenesis is the creation of new blood vessels from the existing blood vessels. Judah Folkman in 1971 for the first time hypothesized angiogenesis as a factor of enabling malignant tumor growth in cancer [Folkman, 1971]. In wound healing the blood flow is restored to the injured tissues by providing necessary nutrients and oxygen for physiologic remodeling of the wound in a healthy body. This process of wound healing is often called hemangiogenesis. In pathologic hemangiogenesis sometimes leaky and unstable vessels are formed which are unnecessary and destructive for the tissues and transpires in plentiful different diseases like eye blinding diseases, atherosclerosis, inflammation and cancer [Carmeliet, 2005, Ellenberg, 2010]. Anti-hemangiogenic medications are used to its cure with impressive effect on pathologic growth of blood vessels. Angiogenesis is dependent up on cells adhesion and proteolytic mechanisms which involves the activity of molecules responsible for adhesion, proteins, extracellular matrix (ECM), proteases and growth factors (GF).

Angiogenesis is mainly classified in to two different types.

1. Sprouting Angiogenesis
2. Intussuseptive/splitting angiogenesis

#### *Sprouting Angiogenesis*

The vascular endothelial cells has the capability to divide in the presence of physiologic stimulus. A sequential events must occur in order for the vascular sprouting to take place. These sequential events includes: secretion of the growth factors (GF),

deterioration of the basement membrane, decision and activation of the tip cell, guiding the sprout generated from endothelial cell in the direction of gradient of growth factor, proliferation of stalk cell, formation of solid sprouts of endothelial cells and connecting of sprouts to vascular loops.

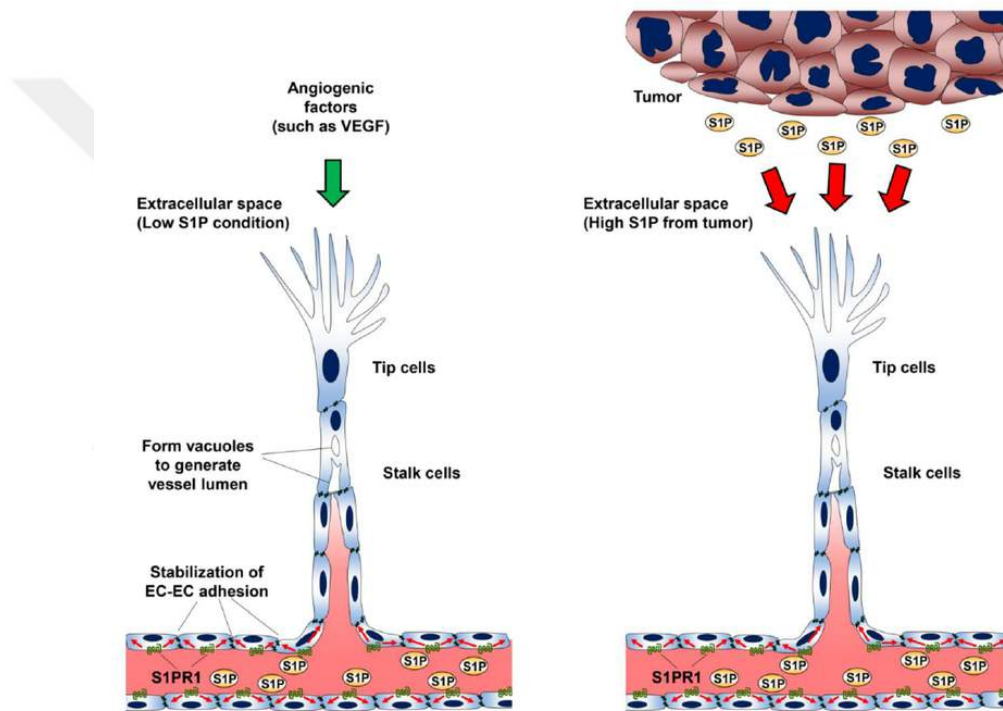


Figure 4.1: Sprouting angiogenesis triggered by biochemicals, (a) sprouting angiogenesis by providing biochemical directly, (b) biochemical secreted by tumor spheroids triggered sprouting angiogenesis.

Sprouting angiogenesis takes place in weakly per-fused tissues where mechanism for sensing oxygen detects a level of hypoxia that appeals for the formation of fresh blood vessels suitable for the metabolic requirements of parenchymal cells. The response of different types of parenchymal cells such as astrocytes, hepatocytes, myocytes, neurons, etc to hypoxic environment is through the secretion of key proangiogenic growth factor known as vascular endothelial growth factor of type A (VEGF-A). The endothelial cell receiving excess amount of VEGF-A becomes a tip cell. This endothelial tip cell leads the whole developing process from the capillary sprout through

the ECM towards an angiogenic centre. This angiogenic center secretes the angiogenic stimulus such as VEGF-A [Gerhardt, 2008, Ruhrberg, 2002, Carmeliet, 2009, Horowitz, 2008].

Thin elongations on tip cells called filopodia secrete huge quantity of proteolytic enzymes. These proteolytic enzymes digest a pathway through the ECM which supports the development of sprout [van Hinsbergh, 2008, Small, 2002]. The filopodia of endothelial tip cells is provided with vascular endothelial growth factors receptors of type 2 (VEGFR2), which allows tip cells to “sense” VEGF-A concentrations. This helps the tip cells to align in the direction with the VEGF-A gradient. The endothelial stalk cell proliferate by following the tip cell and causes the sprout of capillary to elongate along the tip cells. Lumen is formed with in the series of stalk cells by vacuoles and coalesce. These stalk cells grows and takes shape to become trunk of this newly formed capillary. When the tip cells of multiple sprouts converge at the angiogenesis center fuses together and creates a continuous lumen which supports the continuous flow of blood carrying oxygen. After receiving an adequate quantity of oxygen, the level of VEGF-A secretion return to its normal level.

#### *Intussusceptive angiogenesis*

Intussusceptive angiogenesis often known as splitting angiogenesis because of the vessel wall extends into the lumen which causes a single vessel to divide/split in two separate vessels. It is dynamic intravascular process having the capability to change the structure of the microcirculation. This occurs in normal as well as pathological conditions which involves repairing of tissues [A.Eming, 2007] regeneration of organs [Song, 2011] and tumorigenesis [Zhao, 2011]. Intussusceptive angiogenesis was described by caduff and colleagues in 1986 during visualizing blood vessel structure. They observed small holes in alveolar microvasculature during the phase of rapid polarization and capillary growth [Caduff, 1986]. Since then intussusceptive angiogenesis has given attention and is studied as an important mode for growth and remodeling of the developing vasculature [Styp-Rekowska, 2011, Burri, 2004, Makanya, 2009]. Compar-



ing to sprouting angiogenesis, intussusceptive angiogenesis is fast process and takes few hours or even minutes to complete. It is energetically more suitable and does not having any requirment of cell proliferation or basement membrane degradation. The occurance of sprouting angiogenesis or intussusceptive angiogenesis depends on metabolic and hemodynamic factors. Sprouting angiogenesis is biochemical triggered such as vascular endothelial growth factor (VEFG), FGF and PDGF. On the other hand intussusceptive angiogeneis is triggered due to high value of share stress (mechanical force exerted due to the blood flow) [Styp-Rekowska, 2011] and by a drop in angiogenic factor [Hlushchuk, 2008].

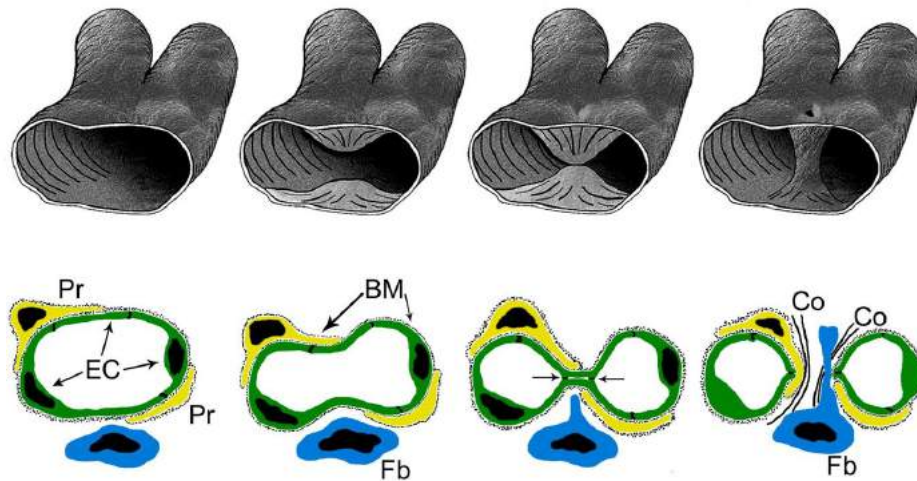


Figure 4.2: 3D schematic illustrating the generation of new vessele through intussusceptive angiogenesis, (BM)base membrane, (fb) fibroblast, (pr) pericytes.

### *Tumor Angiogenesis*

The formation of new blood vessels which is responsible for promoting tumor growth and metastasis is caused by tumor angiogenesis. Both malignant cells and the host cells in the tumor region produces pro-angiogenic factors, predominant in the tumor microenvironment drive this process. Judah Folkman in 1971 for the first time described the connection between pathologic angiogenesis and tumor gwoeth [folkman 1971]. The imbalance between anti-angiogenic factors and pro-angiogenic factors char-



acterize the tumor micro environment and is main reason for the defective vessels. The perfusion in these defective vessels is very poor and contribute to the tumor pathology. These defective vessels supports the tumor mass expansion, promote chronic inflammation, impeding drug delivery and disseminating of tumor cells [Ran, 2012]. In 1989, Ferrara and Henzel demonstrated that vascular endothelial growth factor (VEGF) is the main biochemical that triggers vascular endothelial cells [Ferrara, 1989]. One important factor hypoxia, is regulating factor and activates hypoxia-induced factor 1-alpha (HIF-1  $\alpha$ ) which activates genes like VEGFA, FGF, IGF, integrins and adhesion receptors (cell adhesion molecules), ECM protein and MMPs [Harris, 2002]. Tumor-associated macrophages (TAMs) contributes a significant proportion of the inflammatory tumor stroma which is still not clear whether they are cause of circulating or resident monocytes.

#### *4.0.2 Angiogenesis stimulators*

Angiogenesis is a complex set of various pathological conditions which is dependent on a variety of angiogenic factors. Intercellular signaling using growth factors have a significant contribution in controlling cell differentiation and movements. Chemical stimulation of angiogenesis is performed by various biochemicals such as integrins and postintegrins.

##### *Chemical stimulators*

Research for identifying the biochemical factors that stimulates the angiogenesis has determined both the anti and pro-angiogenic factors. Advancement in research in this area has helped to analyse precisely the behaviour of these biochemicals individually and collectively. Different combination of biochemicals are introduced to the biochemical responsive cells to understand angiogenesis. Vascular endothelial growth factor (VEGF) family is considered as the one having the most tendency to induce angiogenesis. Many other biochemicals such as fibroblast growth factor (FGF), platelet derived growth factor (PDGF), transforming growth factor (TGF), tumor necrosis

factor (TNF), angiopoietins (ANG) and interleukins are involved in angiogenesis [Giraud, 1998, Au, 2009, Cao, 2003, Klagsbrun, 1999, Kamihata, 2002]. VEGF also known as vascular permeability factor (VPF) is produced by cells that stimulates the formation of blood vessels. These important signaling proteins are involved in vasculogenesis and angiogenesis. VEGF is also responsible for restoring the oxygen supply to the tissues under inadequate blood circulation like hypoxia. FGF is another important growth factor that have shown the tendency to support the regeneration and repair of the tissues [L.Moya, 2010]. Due to its potential biological functions it have the capability to regenerate damage tissues like skin, blood vessels, muscles, ligaments, bones and nerves etc. PDGF is responsible for regulation of cell growth and cell division. It plays an important role in blood vessels formation from the existing vessels tissues, mitogenesis and directed cells migration. Transforming growth factor (TGF) also known as tumor growth factor is stimulates endothelial mitogenicity and extracellular matrix production. TNF induces the production of bFGF in endothelial cells and enhances its secretion which activates macrophages. ANG belong from the family of vascular growth factor which takes part in embryonic and postnatal angiogenesis. Angiopoietin signal smooth muscle cells which surrounds the Vessels to control vasodilation and microvascular permeability [Gilbert, 2010]. Among different angiogenic stimulators VEGF family members are known for triggering angiogenesis [Shin, 2011, Carmeliet, 2000]. In addition to VEGF, angiopoietins also plays a crucial role in attracting the supporting cells and in stabilizing of the new blood vessels.

#### 4.0.3 Results and Discussion

##### *Diffusion Experiment*

Diffusion experiment is important to have an understanding of the biomolecule diffusion inside the collagen. The collagen I (Rat-Tail type-1) is used to check the diffusion of Dextran 70kDa. Dextran 70kDa is chosen because its molecular size is identical to the VEGF-1 molecule size. By having the diffusion profiles at different times we

can predict the diffusion of VEGF-1 inside collagen-1. The collagen concentration used in this experiment is 2.7 mg/ml. The collagen is prepared according to the same recipe used in chapter3, in trapan blue experiment. Fig. 4.3 shows the microfluidic chip immediately after loading the dextran 70kDa in one of the side channel while the other channel is filled with Phosphate Buffer Solution (PBS). It can be seen clearly that there is no leakage inside the microfluidic chip and the only possible way for dextran to reach the other side channel is through the collagen. The central rectangle shows the area of the collagen gel inside the microfluidic chip.

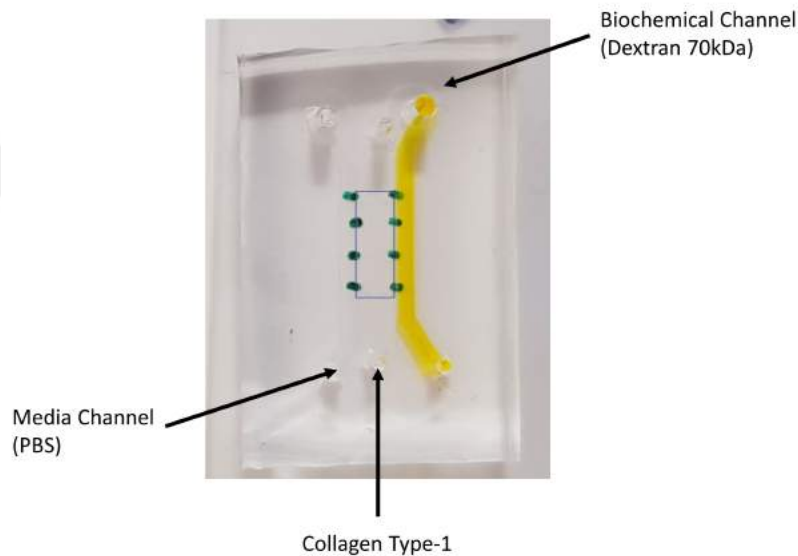


Figure 4.3: Dextran 70kDa loaded in one of the side channel for performing diffusion experiment.

The microfluidic chip shown in Fig. 4.3 was then sealed with a strong sticky tape to close all the inlets and outlets, to avoid evaporation. After sealing the microfluidic chip was placed inside a confocal microscope to record the diffusion images with a regular time interval. The images were recorded using the tiling option as the FOV was not enough to capture the whole collagen region *i.e.* 3 mm wide. Five tiles were used to capture the whole collagen region which were the combined to a single image by the the microscope software automatically. Initially, for 30 minutes the images

were recorded with the time interval of 1 min, after that for the next 24 hours the time interval was set to 10 minutes. Fig. 4.4 shows the diffusion profile of the Dextran 70kDa recorded at different time steps. The excitation and emission wavelengths of Dextran 70kDa are 488/525 nm.

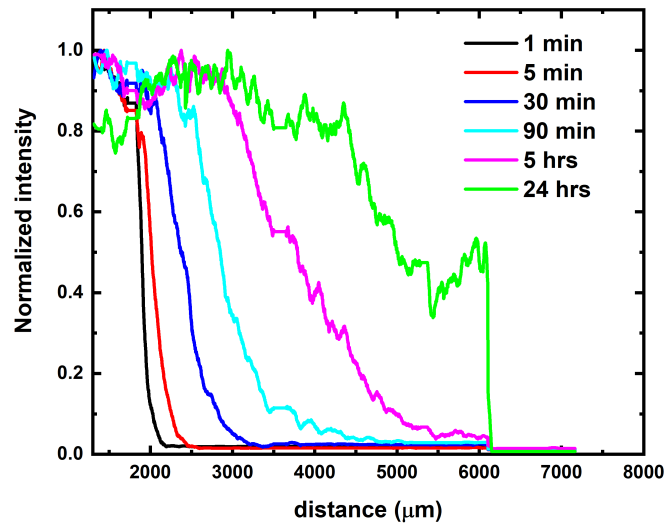


Figure 4.4: Diffusion profile of Dextran 70kDa in collagen type-1 (2.8 mg/ml) recorded at different time intervals.

It is evident from the diffusion profile that Dextran 70kDa having molecular size similar to VEGF molecule can diffuse inside collagen and reaches the opposite channel where endothelial cells will be seeded and due to the diffusion the biochemicals will reach them and stimulate them to produce sprouts. Fig. 4.5 shows the fluorescent images of the Dextran 70 kDa diffusing in the presence of collagen inside a microfluidic chip. Fig. 4.5 (a) shows the image recorded after 1 min of putting the Dextran 70kDa. We can see that Dextran 70 kDa started to diffuse inside the collagen. Fig. 4.5 (b) shows the image recorded after 5 min. As the time passes the distance covered by the Dextran increases. Images recorded after 30 min, 150 min and 5 hours are shown in Fig. 4.5 (c), Fig. 4.5 (d) and Fig. 4.5 (e), respectively. Up till this time we can see clearly that the Dextran has not reached to the other side channel and is still

diffusing inside the collagen.

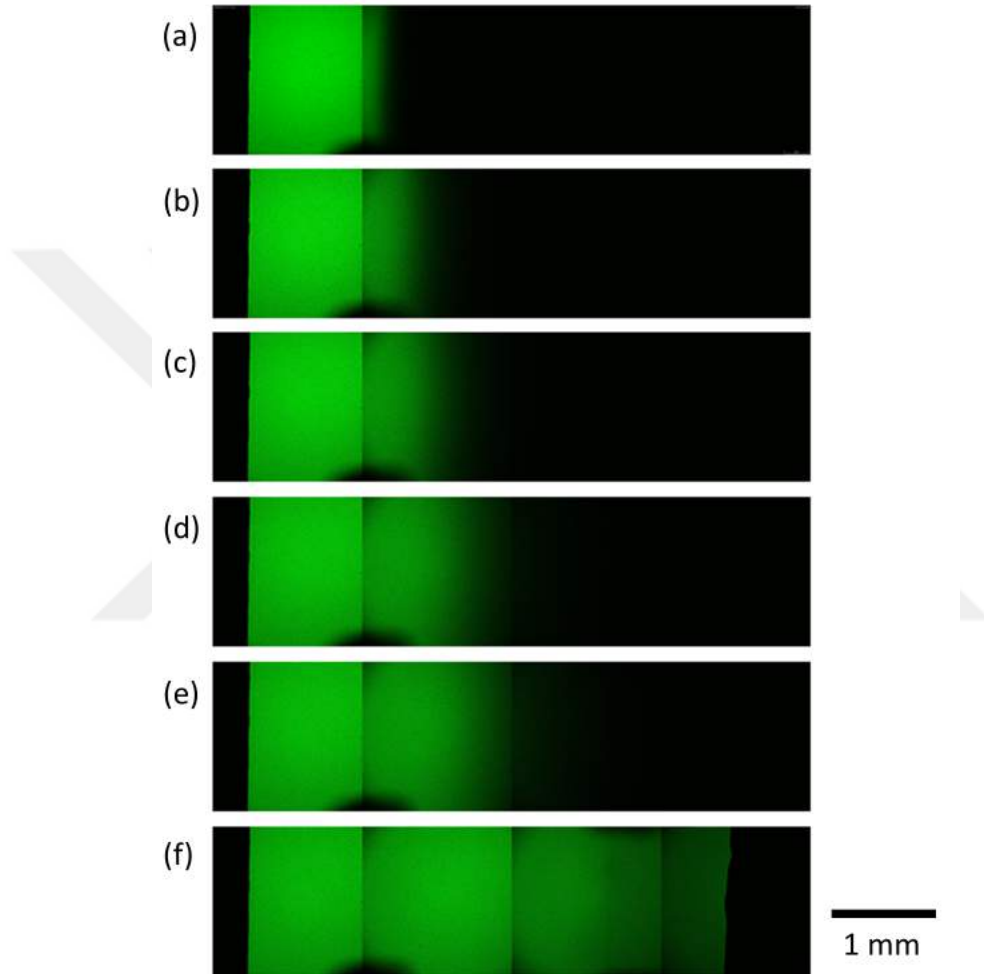


Figure 4.5: Fluorescent images for the diffusion of Dextran 70kDa in collagen type-1 (2.8 mg/ml) inside a microfluidic chip.

To understand the diffusion behavior of Dextran 70kDa in Hystem-HP hydrogel inside a microenvironment, dextran was injected in one of the media channel and putted inside a microscope to capture images of the hydrogel scaffold every 10 min. Fig. 4.6 shows the diffusion profile of Hystem-HP hydrogel at different times for 24 hours.

Fig. 4.7 (a) shows the image recorded after 1 min of putting the Dextran 70kDa. We can see that Dextran 70 kDa started to defuse inside the collagen. Fig. 4.7 (b)

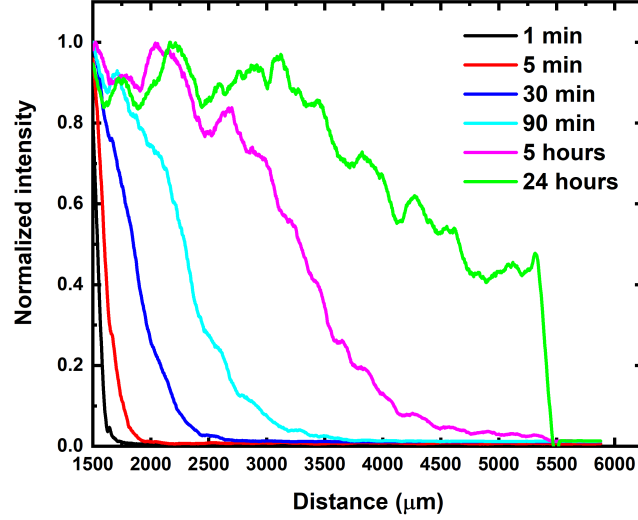


Figure 4.6: Diffusion profile of Dextran 70kDa in Hystem-HP hydrogel inside a microfluidic chip.

shows the image recorded after 5 min. As the time passes the distance covered by the Dextran increases. Images recorded after 30 min, 150 min and 5 hours are shown in Fig. 4.7 (c), Fig. 4.7 (d) and Fig. 4.7 (e), respectively. Up till this time we can see clearly that the Dextran has not reached to the other side channel and is still diffusing inside the collagen.

By comparing the diffusion profiles of collagen type-1 and Hystem-HP hydrogel it is observed that the diffusion rate of Dextran 70 kDa in collagen type-1 is faster than the Hystem-HP hydrogel. One possibility of this behavior can be the porosity. Pore size of collagen type-1 can be slightly bigger than the Hystem-HP. Based on the diffusion profiles of collagen and Hystem-HP hydrogel and the experiment performed with mesenchymal stem cells (MSCs), collagen type-1 was selected to be used for experiments with endothelial cells (ECs). From experiment with MSCs it was evident that cells were unable to enter Hystem-HP hydrogel but perfused nicely are were growing in collagen type-1.

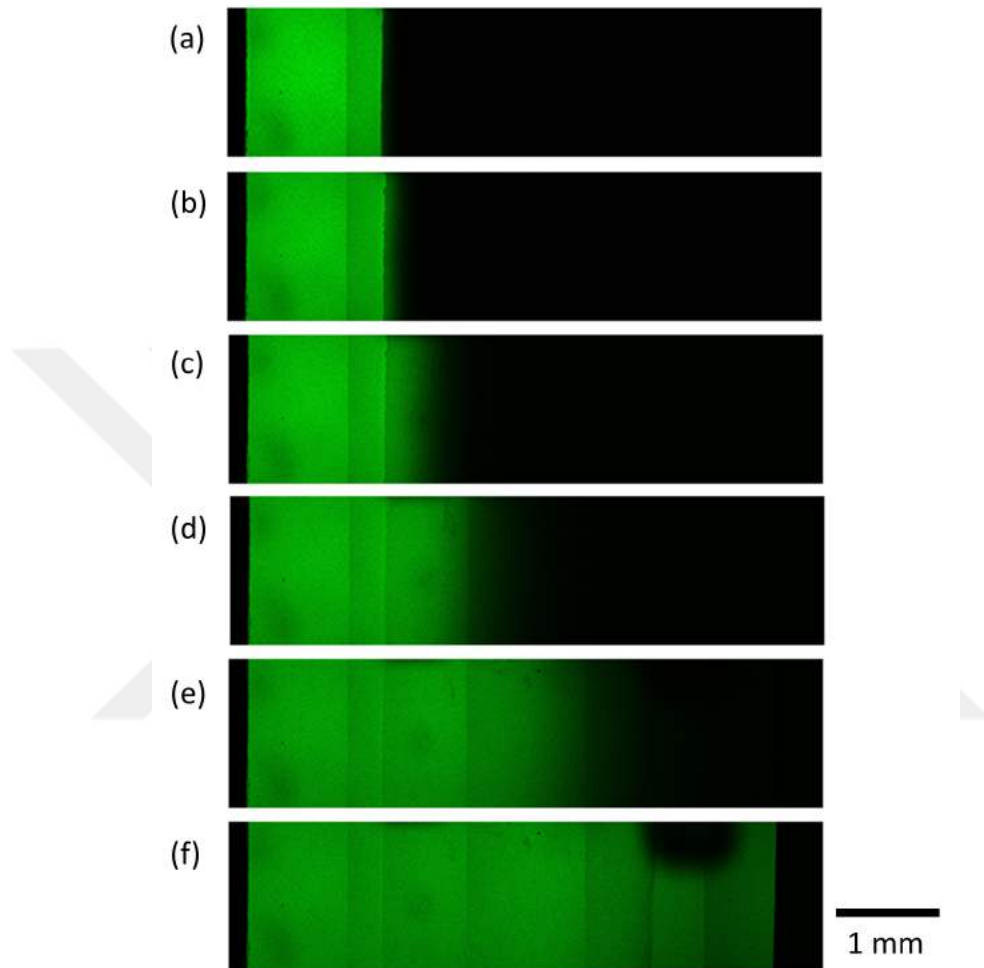


Figure 4.7: Fluorescent images for the diffusion of Dextran 70kDa in Hystem-HP hydrogel inside a microfluidic chip.

#### *Endothelial Cells (HUVECs) as an indicator for angiogenic stimulus*

Human umbilical vein endothelial cells were cultured in cell culture plate and were provided with endothelial cells growth media having all necessary supplements that supports its growth. Endothelial cells were grown in the 2D cell culture plate and waited till its confluency reached approximately 70 percent. This percentage is acceptable for passaging and experiment inside a microfluidic chip.

Figure. 4.9 shows the model of the experiment inside a microfluidic chip, with Human umbilical vein endothelial cells introduced in one of the side channel referred

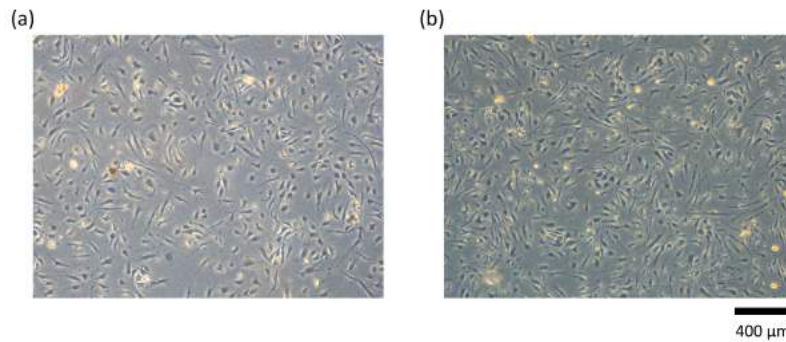


Figure 4.8: Human umbilical vein endothelial cells (HUVECs) cultured on a 2D cell culture plate showing confluency more than 70 percent.

as cell channel. The HUVECs were active and liked the collagen in its microenvironment. HUVECs responded by attaching to the collagen scaffold at the collagen and cell channel interface where they started to grow. For HUVECs to grow inside a collagen, external stimulus *i.e.* VEGF, ANG-1 etc are needed to stimulate these cells to produce sprouts. Normally, endothelial cells grow on the collagen interface wait for the stimulus. When HUVECs sense stimulus it starts to grow inside collagen and produce sprouts in the direction of stimulus gradient. Fig. 4.9 (a) shows that HUVECs grow on the interface of collagen and media in cell channel. When external stimulus is provided for the other side channel (biochemical channel), which diffuses through collagen and reaches the cells on the other side. Endothelial cells respond to these biochemical by producing protrusions or sprouts as shown in Fig. 4.9 (b).

We studied the endothelial cells sprouting in collagen type-1 inside the microfluidic chip over the span of time in the presence of stimulus. The pH value of the collagen was maintained in the range of 7.4 - 7.6 and with concentration 2.8 mg/ml. Approximately 20,000 endothelial cells were introduced in the cells channel. The other side channel known as biomolecules channel was filled with stimulus media. Figure. 4.10 shows the growth of endothelial cells inside a microfluidic chip in collagen. Fig. 4.10 (a) shows that endothelial cells are introduced immediately after the formation of gel inside the microfluidic chip. It can be observed that there exist a nice boundary



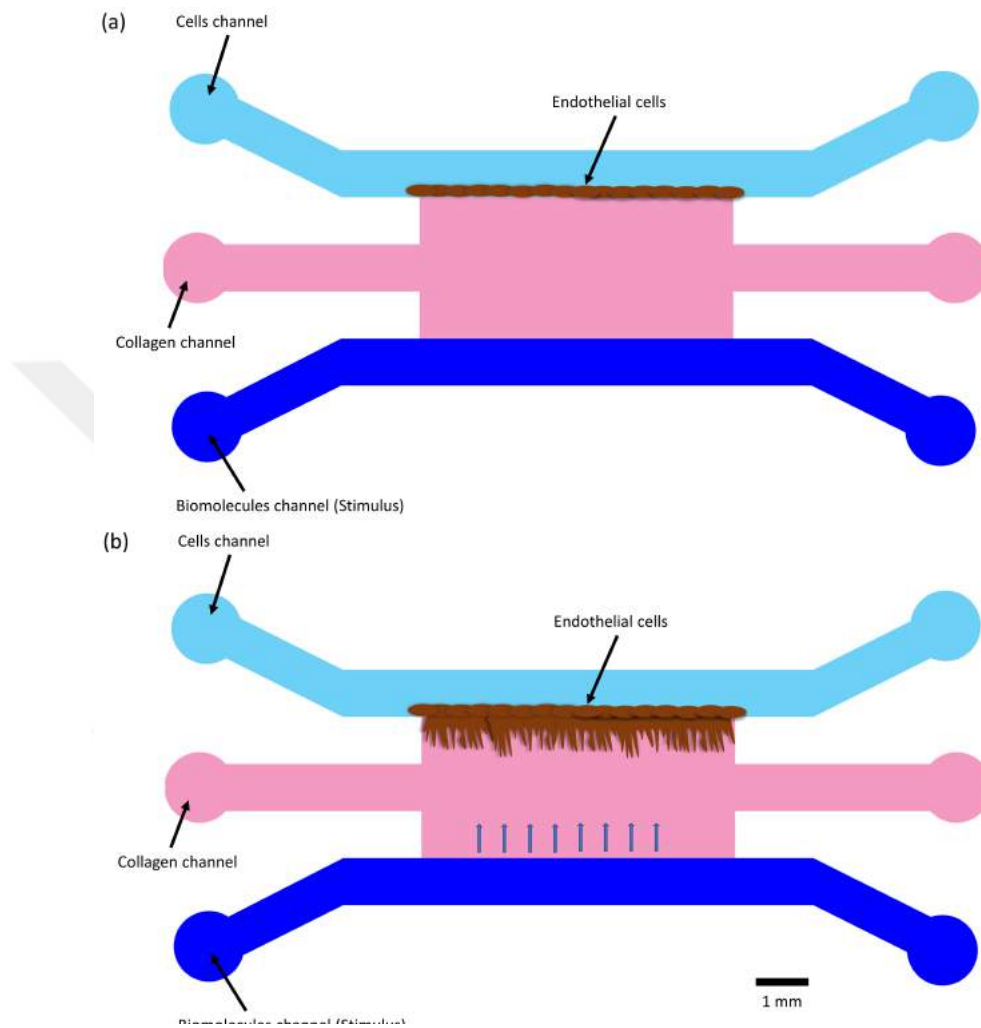


Figure 4.9: Model of microfluidic chip experiment having mesenchymal stem cells seeded in one channel.

of endothelial cells with the collagen and the endothelial cells does not enter the collagen neither from top nor from the bottom. This shows that the collagen solution was nicely loaded inside the microfluidic chip and is completely gelified. After cells were seeded inside the microfluidic chip the chips were tilted at 90 degrees so that cells settle down on the collagen boundary and attach to the collagen. Fig. 4.10 (b) shows the image recorded after 4 hours of tilting the microfluidic chip. Most cells settle down on the interface of the collagen. After 4 hours of tilting the chips a blob of endothelial cells growth medium was putted on all the channel inlets and outlets

to maintain the protein concentration in the cell channel inside the microfluidic chip and to reduce the evaporation of medium from the channels. Fig. 4.10 (c) shows the image recorded after 24 hours of incubation and stimulus is provided in the other side channel. This stimulus will diffuse through collagen and will reach the endothelial cell and trigger them to produce sprouts. After each 24 hours the cells growth media and the stimulus was changed and the chips were incubated. Fig.4.10(d) Shows the endothelial cells growth after 23 hours of providing stimulus. The cells started to grow inside the collagen and started to produce sprouts. Fig. 4.10 (e) shows the image of ECs after 48 hours of stimulus. Endothelial cells had responded to the stimulus by producing sprouts. Fig. 4.10 (f) show the Endothelial cell image recorded with 20X objective which shows that the cell has responded very nicely and produced multiple sprouts after 48 hours of stimulus. Fig. 4.10 (g) shows the right side and Fig. 4.10 (h) shows the left side of the ECs from the same region after 48 hours of stimulus, recorded with 10X objective.

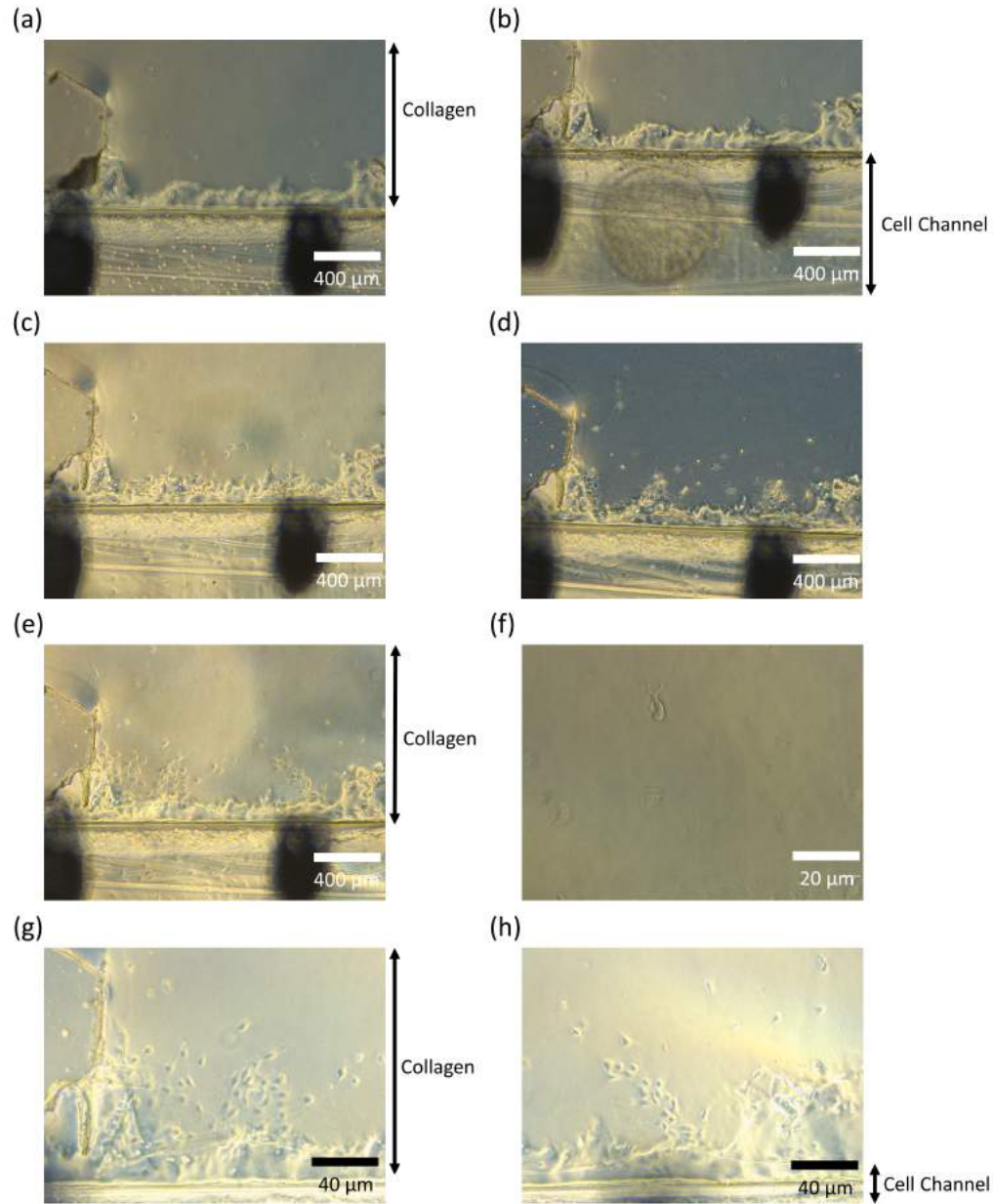


Figure 4.10: Endothelial cells growth inside a microfluidic chip, (a) ECs seeded immediately after hydrogel gelation, (b) microfluidic chip with ECs after 4 hours of incubation, (c) ECs after 24 hours of incubation after introducing ECs and stimulus at 0 hour, (d) ECs after 23 hours of stimulus, (e) ECs after 48 hours of stimulus, (f) EC with sprouts after 48 hours of stimulus (20X), (g) First half of the region of ECs after 48 hours of stimulus (10X), (h) Second half of the region of ECs after 48 hours of stimulus (10X).

## Chapter 5

### CONCLUSION

In chapter 2, we established a microfluidic platform for passive sorting of emulsion droplets. Our platform was capable of generating multi-phase droplets flowing in the common channel with a precise tuning and control over their size and speed. The flow direction of droplets was controlled by engraving inclined and narrow guiding tracks using laser ablation. In the first set of experiments, droplets of three different radii were produced while their flowing speed was kept constant and their deflection along the track was evaluated for two chips with different track widths. Small sized droplets were observed to be fully guided, medium sized droplet were partially guided and big droplets were fairly undeflected while crossing the guiding track. For the chip with slightly wider track, medium sized droplets were better guided relatively due to more pronounced surface energy and wetting effects. In the second set of experiments, partial guiding of droplets was evaluated as a function of droplet velocity while keeping the droplet sizes constant for chips with different track widths. It was observed that the droplets were less guided as their flowing speed was increased for all sizes. Moreover, bigger droplets were less partially guided as compared to the smaller ones at the same flowing speed and vice versa. In the final set of experiments, the droplets from the opposite inlets were forced to merge by collision in a common tapered region to get small and big droplets co-flowing in the channel. Due to the size dependency over guiding, small (unmerged) droplets from both inlets were absolutely guided, while bigger (merged) droplets were unguided resulting in separation of two species with a high success rate.

The experimental results were nicely correlated with the theoretical results obtained from dynamic modeling of droplet motion taking into account the fundamental

forces acting on the droplet. Detailed three-dimensional CFD simulations were also performed to determine the area of a droplet on top of a laser ablated track and away from it. The resulting droplet area changes were used for precise prediction of moving droplet trajectories in finite difference time domain approach. Good agreements were found between the experimental and theoretical trajectories. The reported technique for size-based sorting of droplet species can be employed in designing a microfluidic platform for fast diagnostics in medical applications and detection of reagents for homeland security and public safety. With the capability of sorting droplets based on size and velocity, a variety of sorting parameters can be defined suitable for a range of emulsion species whether carrying chemicals or cells. The reported size-based sorting technique can be employed to design a microfluidic system to be used in molecular detection such as droplets based fluorescence platform for analysis of biomarkers and single molecule counting for digital enzyme counting. This technique can be used in diagnostics, specifically in PCR to demonstrate its significance due to low reagent consumption, sorting the droplet containing the specimen to be tested and short assay time. In addition, the chemically treated samples can be parted and can be analyzed while others are finely deflected to the waste outlet. With the application of this technique, the present work has the potential to be applied effectively in the field of cell biology, chemistry and pharmacology.

In chapter 3, an extensive study of designing a 3D novel micro-environment platform for in-vitro studies and demonstrated its capability by growing mesenchymal stem cells inside a microfluidic chip.

The developed microfluidic chip is capable of mimicking in-vitro behavior. we incorporated a collagen scaffold without deploying micropillars array any where inside the chip for confining the collagen rather we used the combined effect of surface tension and capillary action to fill the collagen loading channel and confine it to its specified region. This integration of collagen scaffold inside a microfluidic chip allows fluid control with the advantage of studying microenvironment in 3D. This method of 3D cell culturing has open new paths for different biological applications. we provided

two different microfluidic designs to mimic microenvironment in 3D. The first design consists of two side channels *i.e.* cell channel and medium channel, for introducing cell inside a microfluidic chip and medium channel to provide media at the beginning stages of the experiment and later to provide stimulus for stimulating the cells. The design also have a region for incorporating collagen gel, which provides control delivery of stimulus and keeps the collagen hydrated from the other side. The second microfluidic design is an advanced version of the first design as it contains compartments for growing tumor spheroids in the biochemical channel. These compartments are like cell traps, once cells enters in to these compartments will not get away while changing cell medium and will grow there to take the shape of a tumor spheroid. Tumor spheroids secretes biochemicals that stimulates the endothelial cells. The microfluidic chip will characterize the angiogenic ability of different tumor spheroids. To demonstrate the ability of the chip designed, MSCs were introduced and successfully grown inside a microfluidic chip.

In Chapter 4, angiogenic behavior of endothelial cells was studied in the presence of biochemical injected in one of the side channel *i.e.* biochemical channel. Diffusion of two different scaffold materials was studied to select the suitable scaffold. Diffusion in collagen was slightly faster than the Hystem-HP hydeogel, aslo from the experiments performed with MSCs discussed in chapter 3, MSCs were unable to grow inside the collagen and were aligned along the interface. Based on the diffusion and MSCs experiment collagen type-1 was selected for conducting angiogenesis experiment. ECs were introduced in the microfluidic chip and were later provided by stimulus through other side channel. The ECs responded to the stimulus by producing sprouts, which were imaged and were stained using immunofluorescence protocol and were imaged under confocal microscope.

## BIBLIOGRAPHY

- [Abbyad, 2010] Abbyad, P. (2010). Rails and anchors: guiding and trapping droplet microreactors in two dimensions. *Lab Chip*, 11(5):813 – 821.
- [Abbyad et al., 2010] Abbyad, P., Tharaux, P. L., Martin, J. L., Baroud, C. N., and Alexandrou, A. (2010). Sickling of red blood cells through rapid oxygen exchange in microfluidic drops. *Lab Chip*, 10(19):2505 – 2512.
- [A.Eming, 2007] A.Eming, S. (2007). Regulation of angiogenesis: wound healing as a model. *Prog Histochem Cytochem.*, 42(3):115 – 170.
- [Agresti, 2010] Agresti, J. J. (2010). Ultrahigh-throughput screening in drop-based microfluidics for directed evolution. *PNAS*, 107(14):4004 – 4009.
- [Ahn, 2005] Ahn, K. (2005). Dielectrophoretic manipulation of drops for high-speed microfluidic sorting devices. *Appl. Phys. Lett.*, 88(2):24104.
- [Alitalo, 2011] Alitalo, K. (2011). The lymphatic vasculature in disease. *Nat Med.*, 17(11):1371 – 1380.
- [Andersson, 2004] Andersson, H. (2004). Microfabrication and microfluidics for tissue engineering: state of the art and future opportunities. *Lab Chip*, 4(2):98 – 103.
- [Anguiano, 2017] Anguiano, M. (2017). Characterization of three-dimensional cancer cell migration in mixed collagen-matrigel scaffolds using microfluidics and image analysis. *PLoS One*, 12(2).
- [Anna, 2002] Anna, S. L. (2002). Formation of dispersions using “flow focusing” in microchannels. *Appl. Phys. Lett.*, 82(3):364.

- [Aref, 2013] Aref, A. R. (2013). Screening therapeutic emt blocking agents in a three-dimensional microenvironment. *Integr Biol (Camb)*., 5(2):381 – 389.
- [Armulik, 2005] Armulik, A. (2005). Endothelial/pericyte interactions. *Circ Res.*, 97(6):512 – 523.
- [Au, 2009] Au, P. (2009). Paradoxical effects of pdgf-bb overexpression in endothelial cells on engineered blood vessels in vivo. *Am J Pathol.*, 175(1):294 – 302.
- [Barbulovic-Nad, 2010] Barbulovic-Nad, I. (2010). A microfluidic platform for complete mammalian cell culture. *Lab Chip*, 10(12):1536 – 1542.
- [Baret, 2010] Baret, J. C. (2010). Quantitative cell-based reporter gene assays using droplet-based microfluidics. *Chem. Biol.*, 7(15):528 – 536.
- [Baroud, 2007] Baroud, C. N. (2007). An optical toolbox for total control of droplet microfluidics. *Lab Chip*, 7(8):1029 – 1033.
- [Bonetta, 2005] Bonetta, L. (2005). Flow cytometry smaller and better. *Nature Methods*, 2(10):785 – 795.
- [Bonvin, 2010] Bonvin, C. (2010). A multichamber fluidic device for 3d cultures under interstitial flow with live imaging: Development, characterization, and applications. *Biotechnol Bioeng.*, 105(5):982 – 991.
- [Burri, 2004] Burri, P. H. (2004). Intussusceptive angiogenesis: its emergence, its characteristics, and its significance. *Dev Dyn.*, 231(3):474 – 488.
- [B.Vernon, 1999] B.Vernon, R. (1999). A novel, quantitative model for study of endothelial cell migration and sprout formation within three-dimensional collagen matrices. *Microvasc Res.*, 57(2):118 – 133.
- [B.Wheeler, 2006] B.Wheeler, M. (2006). Application of sexed semen technology to in vitro embryo production in cattle. *Theriogenology*, 65(1):219 – 227.



- [Caduff, 1986] Caduff, J. H. (1986). Scanning electron microscope study of the developing microvasculature in the postnatal rat lung. *Anat Rec.*, 16(2):154 – 164.
- [Cao, 2003] Cao, R. (2003). Angiogenic synergism, vascular stability and improvement of hind-limb ischemia by a combination of pdgf-bb and fgf-2. *Nat Med.*, 9(5):604 – 613.
- [Carmeliet, 2000] Carmeliet, P. (2000). Angiogenesis in cancer and other diseases. *Nat med.*, 407(6801):249 – 257.
- [Carmeliet, 2005] Carmeliet, P. (2005). Angiogenesis in life, disease and medicine. *Nature*, 438(7070):1932 – 1936.
- [Carmeliet, 2009] Carmeliet, P. (2009). Branching morphogenesis and antiangiogenesis candidates: tip cells lead the way. *Nat Rev Clin Oncol*, 6(6):315 – 326.
- [Chabert, 2008] Chabert, M. (2008). Microfluidic high-throughput encapsulation and hydrodynamic self-sorting of single cells. *PNAS*, 105(9):3191 – 3196.
- [Chabret, 2005] Chabret, M. (2005). Droplet fusion by alternating current (ac) field electrocoalescence in microchannels. *Electrophoresis*, 26(19):3706 – 3715.
- [Chen, 2010] Chen, A. A. (2010). Multiplexed, high-throughput analysis of 3d microtissue suspensions. *Integr Biol (Camb)*., 2(10):517 – 527.
- [Chen, 2008] Chen, J. (2008). Eph receptor tyrosine kinases: Modulators of angiogenesis. retinal and choroidal angiogenesis. *Springer*, pages 203 – 219.
- [Chetouani, 2006] Chetouani, H. (2006). Diamagnetic levitation with permanent magnets for contactless guiding and trapping of microdroplets and particles in air and liquids. *IEEE Trans. Magn.*, 42(10):3557 – 3559.
- [Chován, 2002] Chován, T. (2002). Microfluidic chips for clinical and forensic analysis. *Trends in Biotechnology*, 20(3):116 – 122.

- [Chung, 2009a] Chung, S. (2009a). Cell migration into scaffolds under co-culture conditions in a microfluidic platform. *Lab Chip*, 9(2):269 – 275.
- [Chung, 2009b] Chung, S. (2009b). Surface-treatment-induced three-dimensional capillary morphogenesis in a microfluidic platform. *Adv Mater.*, 21(47):4863 – 4867.
- [Dangla, 2011] Dangla, R. (2011). Trapping microfluidic drops in wells of surface energy. *Phys. Rev. Lett.*, 107(12):12450.
- [Domansky, 2010a] Domansky, K. (2010a). Perfused multiwell plate for 3d liver tissue engineering. *Lab Chip*, 10(1):51 – 58.
- [Domansky, 2010b] Domansky, K. (2010b). Perfused multiwell plate for 3d liver tissue engineering. *Lab Chip*, 10(1):51 – 58.
- [Douglas, 1998] Douglas, T. (1998). Host - guest encapsulation of materials by assembled virus protein cages. *Nature*, 393:152 – 155.
- [Eduati et al., 2018] Eduati, F., Utharala, R., Madhavan, D., Neumann, U. P., Longerich, T., Cramer, T., Saez-Rodriguez, J., and Merten, C. A. (2018). A microfluidics platform for combinatorial drug screening on cancer biopsies. *Nat. Commun.*, 9(2434):1 – 13.
- [Ellenberg, 2010] Ellenberg, D. (2010). Novel aspects of corneal angiogenic and lymphangiogenic privilege. *Prog Retin Eye Res.*, 29(3):1932 – 1936.
- [Even-Ram, 2005] Even-Ram, S. (2005). Cell migration in 3d matrix. *Current Opinion in Cell Biology*, 17(5):524 – 532.
- [Farahat, 2012] Farahat, W. A. (2012). Ensemble analysis of angiogenic growth in three- dimensional microfluidic cell cultures. *PLoS One*, 7(5).

- [Ferrara, 1989] Ferrara, N. (1989). Pituitary follicular cells secrete a novel heparin-binding growth factor specific for vascular endothelial cells. *Biochem Biophys Res Commun.*, 161(2):851 – 858.
- [Folkman, 1971] Folkman, J. (1971). Tumor angiogenesis: therapeutic implications. *N Engl J Med.*, 285(21):1182 – 1186.
- [Formaggia, 2009] Formaggia (2009). Cardiovascular mathematics: Modeling and simulation of the circulatory system. 1:1 – 522.
- [Fradet et al., 2011] Fradet, E., McDougall, C., Abbyad, P., Dangla, R., McGloin, D., and Baroud, C. N. (2011). Combining rails and anchors with laser forcing for selective manipulation within 2d droplet arrays. *Lab Chip*, 11(24):4228 – 4234.
- [Franke, 2006] Franke, T. (2006). Surface acoustic wave (saw) directed droplet flow in microfluidics for pdms devices. *Lab Chip*, 9(18):2625 – 2627.
- [Garstecki et al., 2006] Garstecki, P., Fuerstman, M. J., Stone, H. A., and Whitesides, G. M. (2006). Formation of droplets and bubbles in a microfluidic t-junction – scaling and mechanism of break-up. *Lab Chip*, 6(3):437 – 446.
- [Gerhardt, 2003] Gerhardt, H. (2003). Endothelial-pericyte interactions in angiogenesis. *Cell Tissue Res.*, 314(1):15 – 23.
- [Gerhardt, 2008] Gerhardt, H. (2008). Vegf and endothelial guidance in angiogenic sprouting. *Organogenesis*, 4(4):241 – 246.
- [Gilbert, 2010] Gilbert, S. F. (2010). Developmental biology (looseleaf). *Sinauer Associates Incorporated*, pages 1 – 750.
- [Giraud, 1998] Giraud, E. (1998). Tumor necrosis factor-alpha regulates expression of vascular endothelial growth factor receptor-2 and of its co-receptor neuropilin-1 in human vascular endothelial cells. *J Biol Chem.*, 273(34):22128 – 22135.

- [Griffith, 2006] Griffith, L. G. (2006). Capturing complex 3d tissue physiology in vitro. *Nat Rev Mol Cell Biol.*, 7(3):211 – 224.
- [Guo, 2012] Guo, M. T. (2012). Droplet microfluidics for high-throughput biological assays. *Lab Chip*, 12(12):2146 – 2155.
- [Hankemeier, 2010] Hankemeier, S. (2010). Modulation of proliferation and differentiation of human bone marrow stromal cells by fibroblast growth factor 2: potential implications for tissue engineering of tendons and ligaments. *Tissue Eng.*, 1(1-2):41 – 49.
- [Harada et al., 2012] Harada, Y., Yoon, D. H., Sekiguchi, T., and Shoji, S. (2012). Size-oriented passive droplet sorting by using surface free energy with micro guide groove. In *25th International Conference on Micro Electro Mechanical Systems (MEMS)*, Peris, France. IEEE.
- [Harris, 2002] Harris, A. L. (2002). Hypoxia—a key regulatory factor in tumour growth. *Nat Rev Cancer.*, 2(1):38 – 47.
- [Hlushchuk, 2008] Hlushchuk, R. (2008). Tumor recovery by angiogenic switch from sprouting to intussusceptive angiogenesis after treatment with ptk787/zk222584 or ionizing radiation. *Am J Pathol.*, 173(4):1173 – 1185.
- [Horowitz, 2008] Horowitz, A. (2008). Branching morphogenesis. *Nat Rev Clin Oncol*, 103(8):784 – 795.
- [Huebner, 2009] Huebner, A. (2009). Static microdroplet arrays: a microfluidic device for droplet trapping, incubation and release for enzymatic and cell-based assays. *Lab Chip*, 9(5):692 – 698.
- [Irimia, 2006] Irimia, D. (2006). Microfluidic system for measuring neutrophil migratory responses to fast switches of chemical gradients. *Lab Chip*, 6(2):191 – 198.

- [Jain, 2004] Jain, K. K. (2004). Applications of biochips:from diagnostics to personalized medicine. *Curr Opin Drug Discov Devel*, 7(3):285 – 289.
- [Jeon, 2014] Jeon, J. S. (2014). Generation of 3d functional microvascular networks with human mesenchymal stem cells in microfluidic systems. *Integr Biol (Camb)*, 6(5):555 – 563.
- [Kamihata, 2002] Kamihata, H. (2002). Improvement of collateral perfusion and regional function by implantation of peripheral blood mononuclear cells into ischemic hibernating myocardium. *Chemistry & Biology*, 22(11):217 – 224.
- [Klagsbrun, 1999] Klagsbrun, M. (1999). Molecular angiogenesis. *Chemistry & Biology*, 6(8):217 – 224.
- [Kothapalli, 2011] Kothapalli, C. R. (2011). A high-throughput microfluidic assay to study neurite response to growth factor gradients. *Lab Chip*, 11(3):497 – 507.
- [Kurup and Basu, 2013] Kurup, G. K. and Basu, A. S. (2013). Size based droplet sorting with wide tuning range using tensiophoresis. In *17th International Conference on Miniaturized Systems for Chemistry and Life Sciences ( $\mu$ TAS)*, Freiburg, Germany. CBMS.
- [Lecault, 2011] Lecault, V. (2011). High-throughput analysis of single hematopoietic stem cell proliferation in microfluidic cell culture arrays. *Nat Methods.*, 8(7):581–586.
- [Lee et al., 2018] Lee, Y., Choi, J. W., Yu, J., Park, D., Ha, J., Son, K., Lee, S., Chung, M., Kim, H.-Y., and Jeon, N. L. (2018). Microfluidics within a well: an injection-molded plastic array 3d culture platform. *Lab Chip*, 18:2433–2440.
- [Link, 2006] Link, D. R. (2006). Electric control of droplets in microfluidic devices. *Angew. Chem. Int. Ed. Engl.*, 45(16):2556 – 2560.

- [Link et al., 2006] Link, D. R., Grasland-Mongrain, E., Duri, A., Sarrazin, F., Cheng, Z., Cristobal, G., Marquez, M., and Weitz, D. A. (2006). Electric control of droplets in microfluidic devices. *Angew. Chem. Int. Ed. Engl.*, 45(16):2556 – 2560.
- [Liu, 2008] Liu, W. W. (2008). A microfluidic chamber for analysis of neuron-to-cell spread and axonal transport of an alpha-herpesvirus. *PLoS One*, 3(6):e2382.
- [L.Moya, 2010] L.Moya, M. (2010). The effect of fgf-1 loaded alginate microbeads on neovascularization and adipogenesis in a vascular pedicle model of adipose tissue engineering. *Biomaterials.*, 12(10):2816 – 2826.
- [Mahler et al., 2018] Mahler, L., Wink, K., Beulig, R. J., Scherlach, K., Tovar, M., Zang, E., Martin, K., Hertweck, C., Belder, D., and Roth, M. (2018). Detection of antibiotics synthesized in microfluidic picolitre-droplets by various actinobacteria. *Sci Rep.*, 8(13087):1 – 11.
- [Makanya, 2009] Makanya, A. N. (2009). Intussusceptive angiogenesis and its role in vascular morphogenesis, patterning, and remodeling. *Angiogenesis.*, 12(2):113 – 123.
- [Mierke, 2011] Mierke, C. T. (2011). Cancer cells regulate biomechanical properties of human microvascular endothelial cells. *Journal of Biological Chemistry*, 286(46):40025 – 40037.
- [M.Mercurio, 2001] M.Mercurio, A. (2001). Towards a mechanistic understanding of tumor invasion—lessons from the  $\alpha_6\beta_4$  integrin. *Seminar in Cancer Biology*, 11(2):129 – 141.
- [Papetti, 2002] Papetti, M. (2002). Mechanisms of normal and tumor-derived angiogenesis. *Am J Physiol Cell Physiol.*, 282(5):c947 – 970.
- [Park, 2003] Park, T. H. (2003). Integration of cell culture and microfabrication technology. *Biotechnol Prog*, 19(2):243 – 253.

- [Pekin, 2011] Pekin, D. (2011). Quantitative and sensitive detection of rare mutations using droplet-based microfluidics. *Lab Chip*, 11(13):2156 – 2166.
- [Piorek et al., 2012] Piorek, B. D., Lee, S. J., Moskovits, M., and Meinhart, C. D. (2012). Free-surface microfluidics/surface-enhanced raman spectroscopy for real-time trace vapor detection of explosives. *Anal. Chem.*, 84(22):9700–9705.
- [Pit, 2016] Pit, A. M. (2016). Electrode-assisted trapping and release of droplets on hydrophilic patches in a hydrophobic microchannel. *Microfluid Nanofluid*, 20(123):1 – 12.
- [Polverini, 2002] Polverini, P. (2002). Angiogenesis in health and disease: insights into basic mechanisms and therapeutic opportunities. *J Dent Educ.*, 66(8):962 – 975.
- [Ran, 2012] Ran, S. (2012). Tumor angiogenesis.
- [Rashid, 2018] Rashid, Z. (2018). Reconfigurable and permanent wetting patterns on polymer surfaces obtained using plasma oxidation and laser ablation. *Opt. Data Process. Storage*, 4:22 – 29.
- [Rashid, 2019] Rashid, Z. (2019). Passive sorting of emulsion droplets with different interfacial properties using laser-patterned surfaces. *Microfluidics and Nanofluidics*, 23(65).
- [Reyes, 2002] Reyes, D. R. (2002). Micro total analysis systems. 1. introduction, theory, and technology. *Analytical Chemistry*, 74(12):2623 – 2636.
- [Ridley, 2003] Ridley, A. J. (2003). Cell migration: integrating signals from front to back. *Science*, 302(5651):1704 – 1709.
- [Risau, 1995] Risau, W. (1995). Vasculogenesis. *Annu Rev Cell Dev Biol*, 11:73 – 91.

- [Rosenkilde, 2004] Rosenkilde, M. M. (2004). The chemokine system – a major regulator of angiogenesis in health and disease. *APMIS*, 112(7-8):481 – 495.
- [Ruhrberg, 2002] Ruhrberg, C. (2002). Spatially restricted patterning cues provided by heparin-binding vegf-a control blood vessel branching morphogenesis. *Genes Dev*, 16(20):22684 – 22688.
- [Sciambi, 2015] Sciambi, A. (2015). Accurate microfluidic sorting of droplets at 30 khz. *Lab Chip*, 15(1):47 – 51.
- [Shamloo, 2010] Shamloo, A. (2010). Matrix density mediates polarization and lumen formation of endothelial sprouts in vegf gradients. *Lab Chip*, 10(22):3061 – 3068.
- [Shi, 2008] Shi, W. (2008). Droplet-based microfluidic system for individual caenorhabditis elegans assay. *Lab Chip*, 8(9):1432 – 1435.
- [Shim, 2007] Shim, J. U. (2007). Control and measurement of the phase behavior of aqueous solutions using microfluidics. *J. Am. Chem. Soc.*, 129(28):8825 – 8829.
- [Shin, 2011] Shin, Y. (2011). In vitro 3d collective sprouting angiogenesis under orchestrated ang-1 and vegf gradients. *Lab Chip*, 11(13):2175 – 2181.
- [Small, 2002] Small, J. (2002). The lamellipodium: where motility begins. *Trends Cell Biol.*, 12(3):112 – 120.
- [Sollier et al., 2011] Sollier, E., Murray, C., Maoddi, P., and Carlo, D. D. (2011). Rapid prototyping polymers for microfluidic devices and high pressure injections. *Lab Chip*, 11(22):3752 – 3765.
- [Song, 2011] Song, J. J. (2011). Organ engineering based on decellularized matrix scaffolds. *Trends Mol Med.*, 17(8):424 – 432.
- [Song, 2009] Song, J. W. (2009). Microfluidic endothelium for studying the intravascular adhesion of metastatic breast cancer cells. *PLoS One*, 4(6):e5756.



- [Stroock, 2010] Stroock, A. D. (2010). Microfluidic culture models of tumor angiogenesis. *Tissue Eng Part A*, 16(7):2143 – 2146.
- [Styp-Rekowska, 2011] Styp-Rekowska, B. (2011). Intussusceptive angiogenesis: pillars against the blood flow. *Acta Physiol (Oxf)*., 202(3):213 – 223.
- [Su, 2011] Su, X. (2011). Microfluidic cell culture and its application in high-throughput drug screening: cardiotoxicity assay for hERG channels. *J Biomol Screen.*, 16(1):101 – 111.
- [Sudo, 2005] Sudo, R. (2005). Reconstruction of 3d stacked-up structures by rat small hepatocytes on microporous membranes. *FASEB J.*, 19(12):1695 – 1697.
- [Sudo, 2009] Sudo, R. (2009). Transport-mediated angiogenesis in 3d epithelial co-culture. *FASEB Journal*, 23(7):2155 – 2164.
- [Sugiura, 2001] Sugiura, S. (2001). Interfacial tension driven monodispersed droplet formation from microfabricated channel array. *Langmuir*, 17(18):5562 – 5566.
- [Tan et al., 2004] Tan, Y.-C., Fisher, J. S., Lee, A. I., Cristini, V., and Lee, A. P. (2004). Design of microfluidic channel geometries for the control of droplet volume, chemical concentration, and sorting. *Lab Chip*, 4(4):292 – 298.
- [Tan et al., 2007] Tan, Y.-C., Ho, Y. L., and Lee, A. P. (2007). Microfluidic sorting of droplets by size. *Microfluid Nanofluid*, 4:343 – 348.
- [Thorsen, 2001] Thorsen, T. (2001). Dynamic pattern formation in vesicle-generating microfluidic device. *Phys. Rev. Lett.*, 86(18):4163 – 6.
- [Tullis, 2014] Tullis, J. (2014). Selective fusion of anchored droplets via changes in surfactant concentration. *Lab Chip*, 14(17):3285 – 3289.

- [van Hinsbergh, 2008] van Hinsbergh, V. W. (2008). Endothelial sprouting and angiogenesis: matrix metalloproteinases in the lead. *Cardiovasc Res.*, 78(2):203 – 212.
- [Verbridge, 2010] Verbridge, S. S. (2010). Tissue-engineered three-dimensional tumor models to study tumor angiogenesis. *Tissue Eng Part A*, 16(7):2147 – 2152.
- [Verneuil, 2009] Verneuil, E. (2009). Laser-induced force on a microfluidic drop: origin and magnitude. *Langmuir*, 25(9):5127 – 5134.
- [Verpoorte, 2002] Verpoorte, E. (2002). Microfabricated devices in biotechnology and biochemical processing. *Electrophoresis*, 23(5):677 – 712.
- [Vickerman, 2008] Vickerman, V. (2008). Design, fabrication and implementation of a novel multi-parameter control microfluidic platform for three-dimensional cell culture and real-time imaging. *Lab Chip*, 8(9):1468 – 1477.
- [Wang, 1997] Wang, T. (1997). An encapsulation system for the immunoisolation of pancreatic islets. *Nat. Biotechnol.*, 15(4):358 – 362.
- [Whitesides, 2006] Whitesides, G. M. (2006). The origins and the future of microfluidics. *Nature*, 442(7101):368 – 373.
- [Xi et al., 2017] Xi, H. D., Zheng, H., Guo, W., Calvo, A. M. G., Ai, Y., Tsao, C. W., Zhou, J., Li, W., Huang, Y., Nguyen, N.-T., and Tan, S. H. (2017). Active droplet sorting in microfluidics: a review. *Lab Chip*, 17(5):751 – 771.
- [Xu et al., 2012] Xu, L., Lee, H., Panchapakesan, R., and Oh, K. W. (2012). Fusion and sorting of two parallel trains of droplets using a railroad-like channel network and guiding tracks. *Lab Chip*, 12(20):3936 – 3942.
- [Yoon, 2014] Yoon, D. H. (2014). Hydrodynamic on-rail droplet pass filter for fully passive sorting of droplet-phase samples. *RSC Adv.*, 4(71):37721 – 37725.

- [Young, 2010] Young, E. W. K. (2010). Fundamentals of microfluidic cell culture in controlled microenvironments. *Chem Soc Rev.*, 39(3):1036 – 1048.
- [Young, 2012] Young, E. W. K. (2012). Microscale functional cytomics for studying hematologic cancers. *Blood.*, 119(10):76 – 85.
- [Zervantonakis, 2012] Zervantonakis, I. K. (2012). Three-dimensional microfluidic model for tumor cell intravasation and endothelial barrier function. *PNAS*, 109(34):13515 – 13520.
- [Zhao, 2011] Zhao, Y. (2011). Cancer stem cells and angiogenesis. *Int J Dev Biol.*, 55(4-5):477 – 482.